INCORPORATING NOVEL FUNCTIONALITY ON *IN VITRO*

MICROELECTRODE ARRAYS

by

Audrey Sue Hammack

APPROVED BY SUPERVISORY COMMITTEE:

_____

Dr. Bruce E. Gnade, Chair

_____

Dr. Paul Pantano, Co-Chair

_____

Dr. A. Dean Sherry

_____

Dr. Jie Zheng

For my family

INCORPORATING NOVEL FUNCTIONALITY ON *IN VITRO* MICROELECTRODE ARRAYS

by

AUDREY SUE HAMMACK, BS

DISSERTATION

Presented to the Faculty of

The University of Texas at Dallas

in Partial Fulfillment

of the Requirements

for the Degree of

DOCTOR OF PHILOSOPHY IN

CHEMISTRY

THE UNIVERSITY OF TEXAS AT DALLAS

May 2018

ACKNOWLEDGMENTS

I would like to begin by thanking Dr. Bruce Gnade for the opportunity to work and study at UT Dallas. His mentorship and the experience I have gained working on this project have been invaluable. I would also like to thank Dr. Joseph Pancrazio. I am grateful to him for his expert advice, weekly meetings, and the work that his research group contributed to this dissertation. I would also like to acknowledge Dr. Paul Pantano, Dr. A. Dean Sherry, and Dr. Jie Zheng for their excellent feedback throughout the years. I would especially like to express my gratitude to Dr. Pantano for serving as the co-chair of my committee on short notice.

I would like to thank the UT Dallas cleanroom staff for doing an excellent job at maintaining the facility. Their processing expertise and patience with students is unparalleled, and I am grateful for the many, many helpful trainings and conversations that I have had with them. Likewise, I would like to thank Dr. Huiping "Max" Jia for training on the OLED deposition and measurement systems, and many helpful conversations regarding OLED fabrication and cleanroom processing. I would like to thank Dr. Hamid Charkhkar and Dr. Bryan Black for their collaborative work and many helpful conversations regarding MEA technology and cell culture. I would like to thank Rashed Rihani for his collaborative work and time spent making impedance measurements. I would like to thank Dr. Manuel Quevedo-Lopez for access to the lab probe station, which was integral to testing transistors. Similarly, I would like to acknowledge Dr. Walter Voit for lab access to the laser cutter. I would like to thank Andy Gnade at Plexon Inc., for support regarding the NanoZ.

I would like to thank senior students and post-docs for training, mentorship, and advice. This long list includes Dr. Adrian Avendaño, Dr. David Arreaga, Connie Manz, Dr. Israel Mejia, and

many, many others. I am also very grateful to have worked with a talented group of undergraduates. I would like to thank Shadan Alwan, Marcus Fagioli, Hywel Soney, Landon Mignardi, and Michael Martin for their efforts.

Lastly, I would like to thank friends and family for supporting me throughout the years: my parents Charles and Susanne Hammack, Matt Tharby, Mark and Lisa Tharby, Lindsey Smith, Justin Didier, Cathy Sachs, Luis Reyes, and the rest of my colleagues in the cleanroom, NSERL, and Berkner.

March 2018

INCORPORATING NOVEL FUNCTIONALITY ON *IN VITRO*

MICROELECTRODE ARRAYS

Audrey Sue Hammack, PhD
The University of Texas at Dallas, 2018

Supervising Professors: Dr. Bruce E. Gnade, Chair
Dr. Paul Pantano, Co-Chair

The microelectrode array (MEA) is an inexpensive, high throughput platform for measuring and recording extracellular electrical potentials from a culture of electrogenic tissues. However, this technology is not without drawbacks, which this work seeks to address. On conventional MEAs, stimulation of a culture is achieved via electrical stimulation through the electrodes, which may introduce recording artifacts. Optogenetics is a molecular biology technique that can be used to decouple the recording and stimulation functions of the MEA electrode, but hardware required to utilize optogenetics in combination with an MEA is a barrier that prevents utilization of this technique. One project presented here seeks to integrate an MEA with an array of organic light-emitting diodes (OLEDs) driven by thin film transistors (TFTs), to create a multifunctional MEA with optical stimulating capabilities, in order to streamline the hardware required for an *in vitro* optogenetics recording experiment. Discreet functional components are demonstrated and a proof of concept, integrated substrate is presented. Another project presented in this dissertation seeks to insulate the MEA electrodes with polystyrene. The vast set of organic and inorganic materials used to insulate MEA electrodes present challenges to users who must modify cell

culture protocols for cell adhesion to the surface of the MEAs. An MEA that features a patterned film of polystyrene, a material that is far more common to cell culture work, as electrode insulation is presented. Viable cell culture on this MEA and recordings that are comparable to other MEA substrates are demonstrated.

TABLE OF CONTENTS

LIST OF FIGURES

LIST OF TABLES

CHAPTER 1

INTRODUCTION

The brain, even in simple animals, is a complex organ, with various levels of sophisticated neuronal function and organization. New technologies and methods for neuroscience research are developed to facilitate experiments that attempt to probe and understand neuronal functionality and organization, both *in vivo* and *in vitro*. The microelectrode array (MEA) is one such *in vitro* technology. Prior to the MEA, patch clamp techniques were used to measure extracellular electrical activity from single neurons in an *in vitro* culture. The MEA, a planar substrate with an array of electrodes passivated with an insulating film, was introduced as a higher throughput alternative to patch clamp measurements (Gross et al. 1977). Each electrode on the substrate functions as a recording channel. Measurements may be made from many electrodes simultaneously and the platform can be used to measure electrical activity at the network level. However, the MEA suffers drawbacks in cost and precise stimulation of a culture, due to the nature of electrical stimulation through the recording electrodes. Optogenetics, a molecular biology technique that renders neurons susceptible to optical stimulation, potentially decouples the stimulating and recording function of the electrode (Maybeck et al. 2016). But, experiments that utilize optogenetically-engineered neurons rely on complicated stimulation and recording hardware that suffer from a lack of precision in terms of light delivery. A proof of concept multi-functional MEA is presented in this work as an attempt to streamline the hardware involved with *in vitro* optical stimulation and recordings. Motivation for the fabrication of this type of substrate is presented in Chapter 1. Fabrication of the three discreet components of the substrate, the MEA for neural recordings, and organic light-emitting diodes (OLEDs) for optical stimulation, and

thin film transistors (TFTs) to drive OLED operation, are presented in Chapters 2, 3, and 4, respectively, with lifetime stability tests of these devices. Process integration and demonstration of the completed multifunctional MEA substrate are presented in Chapter 5.

Another project in this work demonstrates the feasibility of encapsulating the MEA electrodes with polystyrene. Previous work in fabricating MEAs has utilized a vast set of organic and inorganic materials for dielectric electrode encapsulation. These materials require users to develop complicated protocols for preparing the MEA surface for culture attachment, and some materials suffer serious mechanical, structural, and chemical drawbacks. The work presented in Chapter 6 demonstrates the feasibility of using semiconductor processing technologies to pattern a spin-cast film of polystyrene as the electrode encapsulation.

1.1 The Microelectrode Array

The microelectrode array (MEA) is a device that interfaces neurons with electronic hardware. It consists of electrodes that record electrical activity from an electrogenic cell culture and deliver electrical stimulation. The device can either be a planar substrate on which tissues are plated for *in vitro* use or an implantable device for *in vivo* work. MEAs for *in vitro* use are presented in this work.

1.1.1 Device Development and Current State of the Art

Prior to the development of the MEA, the primary method of recording extracellular electrical activity was the patch clamp method (Neher and Sakmann 1992). In this technique, a micropipette, containing a silver chloride recording electrode in an ionic solution, on a micropositioner is brought to close proximity of a neuron, as viewed under a microscope; noise

in the recordings is minimized when the tip of the recording electrode forms a hermetic, gigaohm seal with the outer wall of a cell membrane, but does not rupture the cell, as shown in a cartoon depiction in Figure 1.1 (Neher et al. 1978).

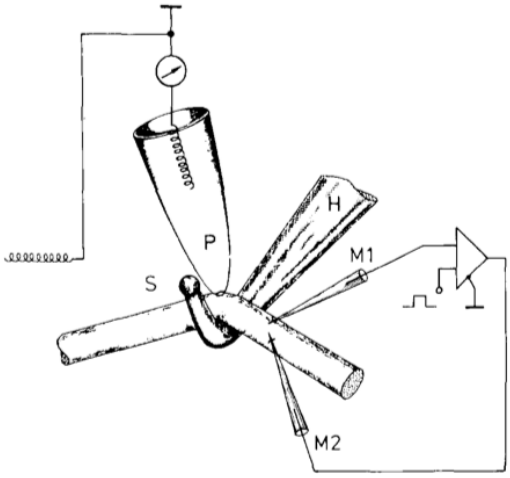

Figure 1.1. Schematic of patch clamp measurements of a muscle fiber (S). The fiber is lifted by support hook H. Microelectrodes (M1 and M2) and pipette (P), containing the ground electrode, are brought into contact with the fiber and are placed 50-100 μm away from the hook. Reprinted from work by Neher et al. (1978).

Electrical currents flow through the cell membrane into the pipette and are recorded by a differential amplifier. The information from recordings reveals a great deal of information about the nature of neuronal electrical activity, down to the level of cell membrane ion channels (Caterina et al. 1997). However, there are major drawbacks to this technique. Achieving the necessary gigaohm seal to the cell membrane, without puncturing the cell, requires a great deal of user training to hone precise manipulations of the pipettes, and is tedious. Additionally, the technique only allows the user to record from a limited number of cells at a time, making this a very low-throughput technique. An experiment that makes use of an automated patch clamp apparatus can only make measurements from 12 neurons simultaneously (Perin et al. 2011).

Finally, this technique is not applicable to chronic studies, as a cell cannot sustain patch clamp recordings for more than a few hours.

The MEA is an alternative technology to the patch clamp technique. First developed independently by C.A. Thomas and Gunter Gross in the 1970's, the *in vitro* MEA consists of conductive electrodes on a planar substrate (Gross et al. 1982; Thomas et al. 1972). A dielectric film insulates the electrode traces, and is patterned to define electrode contacts and bonding pads, as shown in Figures 1.2A and B.

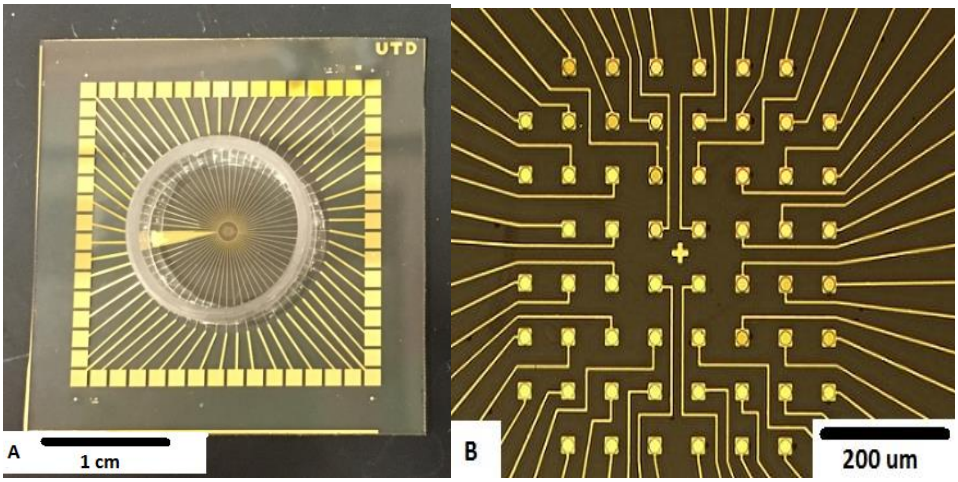

Figure 1.2. Images of an MEA fabricated at UTD. Macroscopic view of MEA substrate, including cell culture ring (A), and magnified image at 2.5X of recording electrodes, in which openings of dielectric on recording pads can be seen (B).

The electrodes record changes in the extracellular field due to current flows from the sum total of all the ionic processes of cells that are in close proximity to the electrode. The outer bonding pads of the substrate allow for the MEA to interface with recording hardware, such as amplifiers, filters and digitizers.

A ring to contain cell culture media is affixed to the surface of the MEA. The cell culture surface of the MEA is sterilized and laminated with organic molecules that promote cell

adhesion, such as collagen or laminin (Hales et al. 2010). A slice of tissue or a suspension of dissociated cells is plated in the ring, following tissue culture protocols, and chemicals and media are introduced to the ring by pipette or an externally mounted perfusion inlet. The substrate is stored in a cell culture incubator during the tissue culture period and when recordings are not being made.

Thanks to thin film deposition and CMOS processing technologies, MEA substrates are available from a number of commercial sources. Electrodes may be fabricated from gold, titanium nitride, platinum, or a transparent metal oxide, such as indium-tin oxide (ITO). The electrodes are encapsulated with inorganic dielectric materials, such as silicon nitride, or polymers. The dielectric is selectively opened to form electrode areas and bonding pads, as shown in Figure 1.2B. Electrode and encapsulation features are patterned using photolithography, which drives the manufacturability of the substrate fabrication. MEAs are available as a simple, single well substrate, or multi-well plates. Regardless of the vendor, the cost for a single well substrate is $350-$500 each (Loewy 2018; Parievsky 2018).

1.1.2 MEA applications

The MEA platform has been widely used to explore electrophysiology of different electrogenic tissues. One of the first arrays, developed by C.A. Thomas in 1972, was plated with dissociated chick cardiomyocytes. The dissociated cells formed a confluent, contractile sheet of tissue on the MEA surface after an incubation period. This work presents observations about the nature of the electrophysiology of the cardiac tissue. Spontaneous electrical activity was synchronized with mechanical contraction, and the period in between potentials was constant, varying 1% over 20-40 beats (Thomas et al. 1972). Guenter Gross developed an MEA platform

independently in 1977. Single unit activity was recorded from a single snail root ganglion cell that was cultured on the device (Gross et al. 1982).

Modern MEA utilization is varied in its scope. Some work has characterized electrophysiology in various tissue types. Recordings from whole slices of retinal tissue, investigations of the synchronization of cell firing and gene expression pathways, investigation of electrical activity synchronization as a function of tissue development, and characterization of electrophysiology of motor neuron cell lines are examples of fundamental work accomplished with MEAs (Aton et al. 2006; Gireesh and Plenz 2008; Meister et al. 1991; Sabitha et al. 2016). The MEA has also found pharmacological applications as a high-throughput platform for drug screening. The MEA offers a quantifiable electrophysiological approach to drug screening, compared to *in vivo* and *ex vivo* assays. MEAs have been used to establish quantitative methods of identifying drug effects, screening panels of new drugs for antiarrhythmic efficacy and pro-arrhythmic risk, and determining toxicity levels of new pharmaceutical compounds (Caspi et al. 2009; Cui et al. 2006; Keefer et al. 2001b).

1.1.3 MEA advantages and limitations

The MEA offers advantages over the patch clamp technique for *in vitro* recordings. Compared to patch clamp, the MEA is a significantly higher-throughput technology, since every electrode is a recording channel, and it is possible to record from several electrodes simultaneously. Using the technology does not require precise electrode manipulation, as electrode locations are fixed and defined by patterning conductor films using photolithography. Finally, the technology is more suitable for chronic studies, as recordings may be obtained from viable cultures, for periods ranging from weeks to months.

However, this technology is not without drawbacks. Compared to other cell-based assay technologies, the MEA is very expensive. Cell culture supplies and cell-based assays are based on inexpensive materials that are processed with cost-efficient manufacturing processes, such as injection-molded polystyrene, making them single-use and disposable supplies (Bennett et al. 2004; Martinez et al. 2007). At a cost of $350-$500 per substrate, commercially available MEAs are not treated as single-use items and are re-used in experiments. Any variability in the surface cleaning or preparation procedure, from one experiment to the next, introduces variability in the cell culture preparation, which may lead to variability in cell culture viability or recordings.

Secondly, tissue stimulation is an important feature of the MEA that is used to probe cellular networks. Most often, this electrical stimulation is delivered via the recording electrodes. This is problematic, since the electrical stimulus required to elicit a response may be 1-2000 times stronger than the signal acquired from the culture, thus introducing recording artifacts (Maybeck et al. 2016). The spatial specificity of electrical stimulation also suffers from a lack of precision, due to poor predictability of current spread through tissue plated on the MEA surface.

Finally, the planar MEA surface means that all the cells plated on the substrate form a single tissue preparation in the same plane. The cell media and any chemicals that are introduced form a homogenous chemical environment that is exposed to the culture. Assay-type experiments require many data points to be collected under different experimental conditions in order to achieve sufficient data for statistical analysis. The cost of a single MEA limits the number of MEAs, and hence experimental test conditions, that can be used for a single experiment. Multiwell MEA substrates from commercial suppliers increase the throughput of experiments. These substrates are available with a number of wells, ranging from 12 to 96 wells

per substrate, with each well holding a tissue preparation (McConnell et al. 2012). As each well is plated individually, there is some variation from well to well. A recent paper demonstrates the fabrication of a novel single well MEA. The MEA electrodes are insulated with a thick polymer film that is patterned into wells, such that each well is a physically isolated and contains a single recording electrode (Kang et al. 2009). This demonstrates the feasibility of achieving several different assay conditions on a single MEA with a single tissue preparation by integrating the MEA with microfluidic cell culture. However, fabrication of this particular microfluidic MEA was achieved with agarose, a polymer material. Soft polymeric materials that have been utilized in microfluidic fabrication, such as agarose and PDMS, suffer from some drawbacks that will be discussed in a later section.

1.2 Optogenetics

Optogenetics is a molecular biology and genetics technique that renders electrogenic tissues susceptible to optical stimulation (Deisseroth et al. 2006). This advancement allows investigators to deliver stimulation that is targeted to cell types with high specificity and on the same timescale as the action potential. When optogenetically-modified tissues are studied on an MEA substrate, the stimulation and recording modalities are decoupled.

1.2.1 Optogenetics development and applications

Optogenetics is an emerging field that combines optical and genetic technology for probing electrophysiology via temporally precise and noninvasive optical stimulation of cell membrane ion channels. The technique was first reported in 2005 by the Deisseroth lab at Stanford, as an alternative to non-cell-type-specific techniques, such as neurotransmitter caging

(Ellis-Davies 2012). In the caging technique, neurotransmitters, such as glutamate, are bound to cage-like molecules that change confirmation in response to light. Bound to the cage, the neurotransmitter is inactive, but it becomes uncaged upon optical stimulation. As the cage opens, the concentration of neurotransmitter in the extracellular space increases, and the neurotransmitter stimulate cell receptors (Shepherd et al. 2003). Because most cells have receptors for common neurotransmitters, it is impossible to target this type of stimulation to a single type of neuron. The next generation of temporally-precise stimulation involved modifying a potassium channel gene with a binding site for azobenzene, a molecule that changes conformation upon radiation of different wavelengths of light. With UV radiation, the azobenzene molecule changes conformation to open the potassium channel, and with visible light radiation, the molecule closes the channel. Light can be used to stimulate or silence the electrical activity of cells expressing the gene for the modified potassium channel, but activity control is limited to timescales ranging from seconds to minutes, due to the mechanism of cell depolarization (Lima and Miesenböck 2005). Deisseroth's contribution to the field simplified the genetic modification by identifying channelrhodopsin-2 (ChR2), a light-gated cell membrane ion channel protein in algae. The protein absorbs blue light, with a peak maximum of 480 nm (Bamann et al. 2008). Upon optical stimulation, the ChR2 channel opens, selectively allowing positive ions to flow through its central pore. Genetic modification of neurons to express ChR2 is ideal for optical control of electrophysiology with microsecond light pulses, with no additional chemical modification (Boyden et al. 2005). Cells that express the ChR2 protein are susceptible to optical stimulation in a way that is cell-type specific and on timescales that are relevant to electrophysiological events. In the time since Deisseroth's first report of optogenetics, a number

of different opsin cell membrane proteins have been either discovered or modified. Another commonly utilized opsin protein is bacteriorhodopsin. This transmembrane proton pump has a broad peak absorption spectrum in the range of 500-650 nm (Lozier et al. 1975). Upon optical stimulation with green light in this wavelength range, bacteriorhodopsin undergoes a conformational change that causes the protein to pump protons out of the intracellular space. This influx of positive charge hyperpolarizes the neuronal membrane, which silences the action potential (Boyden 2011). Hence, neuronal expression of bacteriorhodopsin allows for electrical activity to be controlled with green light. The expanding library of light-sensitive proteins allows researchers to investigate the effects of stimulating or silencing different ion channels at a variety of timescales (Rein and Deussing 2012).

In the decade since the development of this technique, it has found varied application in studying electrophysiology and networking information of different electrogenic tissues, both *in vivo* and *in vitro*. For example, the technique has been applied to study the functional integration of individual components of *in vitro* models of neurodegenerative diseases, such as Parkinson's (Tønnesen et al. 2011). Optogenetics has also been used to suppress seizures in *in vivo* murine models of epilepsy, and *in vitro* work elucidated the mechanism and ideal parameter values (light pulse train frequency and duration and length of time in between pulse trains) for seizure suppression (Chiang et al. 2014). In addition to neurons, the activity of cardiomyocytes has been observed with this technique *in vitro*, which reveals that both electrical activity and mechanical contractions can be optically stimulated in tissues that express ChR2 (Bruegmann et al. 2010).

1.2.2 Limitations to a current optogenetic experiments and the proposed multifunctional MEA device.

While optogenetics offers a novel technique for studying electrophysiology of tissues, the development of light delivery technologies, which is crucial for this technique, is still in rudimentary stages and suffers from a lack of spatial precision. From the earliest report of optogenetic stimulation *in vitro* from the Diesseroth lab, cells were illuminated with a blanket exposure of filtered light from a mercury arc lamp (Boyden et al. 2005); light is delivered with no spatial specificity, which eliminates the possibility of gathering spatiotemporal information from the cell culture. In later experiments, light delivery was slightly more sophisticated, such as laser light delivered by fiber optic cable or a panel of LEDs, both of which suffer from the lack of spatial control of light delivery (Adesnik and Scanziani 2010; Chiang et al. 2014).

Even work that attempts to address the weakness of current optogenetic technology, the proposed platforms do not completely solve the problem. A platform was developed that integrates active-matrix thin film transistor technology and an OLED array for matrix-addressable optical stimulation (Smith et al. 2014). While the paper demonstrates that the OLED and TFT fabrication processes are compatible and produce functional devices, and that the surface of the device supports cell culture, the substrate does not provide a means of recording electrical activity from the plated tissues. The goal of this work is a multifunctional substrate that integrates the recording technology of the MEA with the optical stimulation and spatial precision of an array of matrix-addressable organic light-emitting diodes (OLEDs).

The proposed multifunctional device is fabricated on a glass substrate. A simple schematic of this substrate is shown in Figure 1.3.

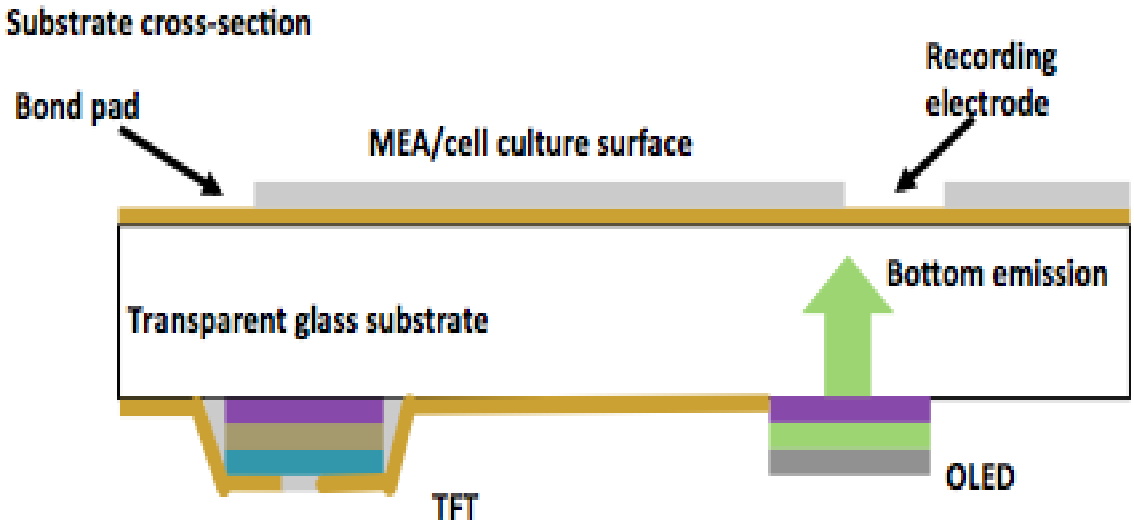

Figure 1.3. A schematic of the proposed integrated, multifunctional substrate.

An array of 64 gold electrodes, encapsulated with parylene-C, is fabricated on the front side of the substrate; this is the cell culture surface of the substrate. Thin film electronics are fabricated on the backside of the substrate. An array of bottom-emission OLEDs provide radiation through the transparent glass substrate for optical stimulation of tissues on the cell culture surface of the substrate. The precise location and the dimensions of the OLED pixel are fixed, as the bottom electrode is patterned by photolithography. As the OLED is fabricated directly on the substrate, the need for stand-alone light sources or waveguides is eliminated, and the position of the source of optical stimulation relative to MEA electrodes is reproducible from substrate to substrate. The rationale for fabricating the OLEDs on the backside of the substrate is two-fold. OLEDs are typically more efficient when fabricated in the bottom-emission configuration (Chu et al. 2006). Separation of the OLED from the recording electrodes by the glass substrate should also eliminate electrical noise in recordings induced by potential cross-talk

between an OLED and a recording electrode. The OLEDs are driven by an array of thin film transistors (TFTs). The TFT array adds the matrix-addressable quality to the substrate, allowing a user to turn on one OLED element at a time. The TFT array also reduces the number of contacts needed to drive the array, making the substrate amenable to connector hardware constructed by collaborators at Plexon, Inc. The substrate is novel, in that it is the first proposed combination of substrate-embedded MEA recording technology and thin film electronics for optogenetic applications. The MEA, OLED, and TFT components of the integrated substrate are patterned using photolithography, which presents challenges in terms of device integration and process compatibility.

1.3 Organic Light Emitting Diodes

The OLED is the component of the proposed multifunctional substrate that delivers optical stimulation to the cell culture. A general overview theory of the OLED operation is discussed in this section. A discussion of OLED fabrication and characterization for the multifunctional integrated MEA substrate is presented in Chapter 3.

1.3.1 Device operation and characterization

The light emitting diode is an electronic device that utilizes the material properties of a semiconductor (i.e. conductivity and the bandgap) to produce electromagnetic radiation in the visible light spectrum. A simple schematic of an OLED is shown in Figure 1.4.

An organic semiconductor is a material with electrical conduction between that of a metal, a highly conductive material, and an insulator, a poorly conductive material. The density of charge carriers and carrier mobility determine the conductivity of a semiconducting material.

Electrons and holes may be injected from a conductive electrode or generated by photoexcitation. For instance, changing the applied bias on the cathode modulates the conductivity of the organic material shown in Figure 1.4.

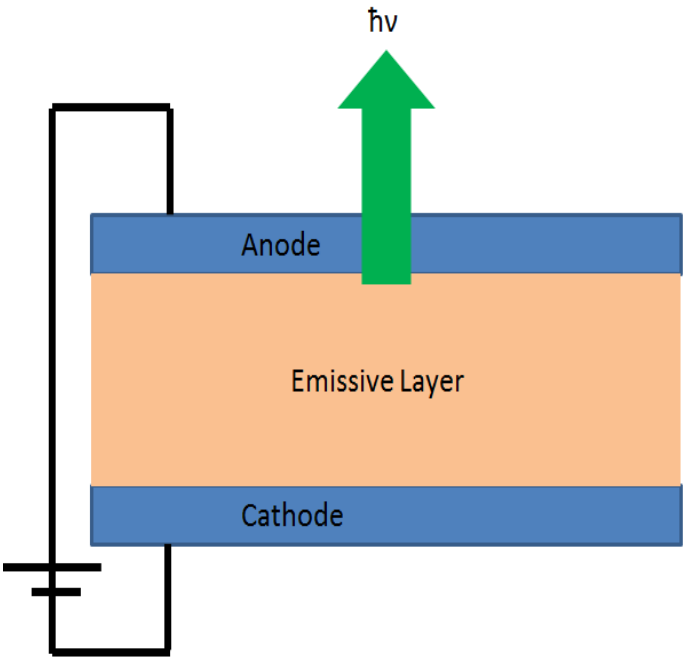

Figure 1.4. A schematic of an OLED. The device consists of a cathode and anode, which inject charge carriers into the emissive layer. Charge recombination in the emissive layer generates electromagnetic radiation in the visible spectrum.

In organic molecules, semiconductor properties arise in aromatic systems: planar, conjugated, cyclic arrangement of sp^2-hybridized atoms (Rawn 2014). An example of this phenomenon in benzene is shown in Figure 1.5. In the plane of the benzene ring, sp^2 hybridized orbitals form σ bonds. The sp^2 hybridized orbitals that are perpendicular to the ring form π bonds above and below the ring. Electrons are exchangeable and delocalized over the pi systems.

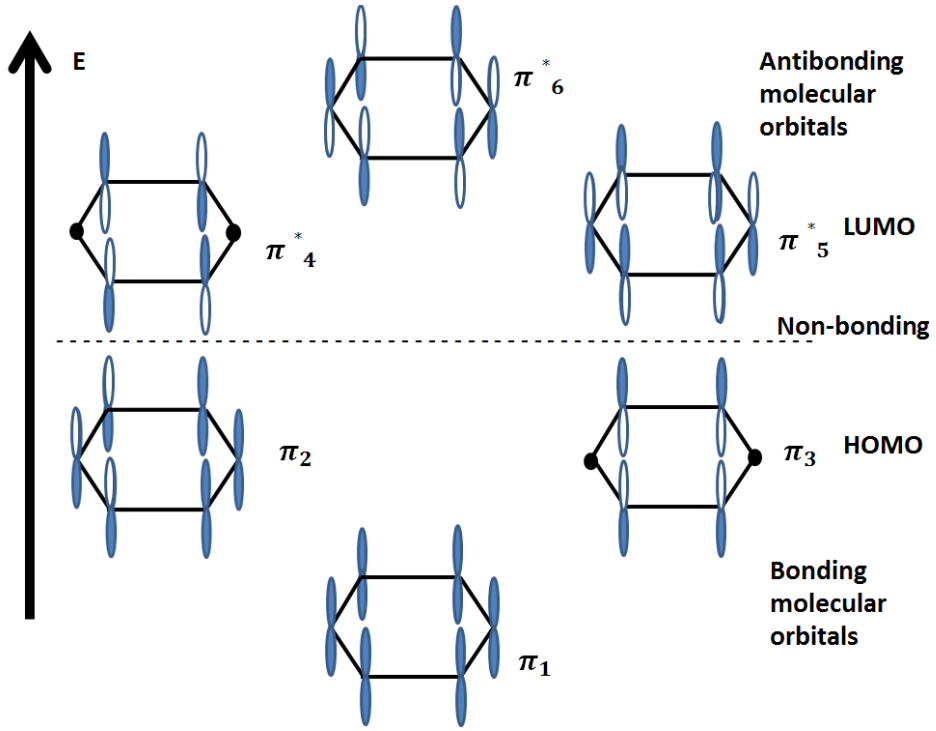

Figure 1.5. The six molecular orbitals of benzene. Orbitals are arranged in order of increasing energy. The three orbitals below the non-bonding line are bonding, and the three above are antibonding. The π_3 and π_2 orbitals are at equal energy, and are considered to be the HOMO. The π^*_4 and π^*_5 orbitals are also at equal same energy and considered to be the LUMO.

Linear combinations of parent atomic orbitals form molecular orbitals. For the example of benzene, the six carbon parent atoms combine in linear combinations to form six molecular orbitals for benzene. Solving the Schrödinger equation yields the electronic wavefunction, which contains information about the allowable molecular orbitals (energy levels) that an electron may occupy. The highest occupied molecular orbital (HOMO) and the lowest unoccupied molecular orbital (LUMO), as seen in Figure 1.5, are two important allowable energy levels that result from this analysis (Carey 2007). The HOMO is filled with electrons, and the LUMO is empty. The energy gap between the HOMO and the LUMO is the bandgap of the organic semiconductor. There are additional energy levels above the LUMO and energy levels below the HOMO.

Electrons may occupy the HOMO and LUMO and some of these additional orbitals in different combinations, called states. It is important to distinguish the difference between orbitals and states. An orbital is an energy level that an electron may occupy, whereas states are the possible combinations of occupied orbitals.

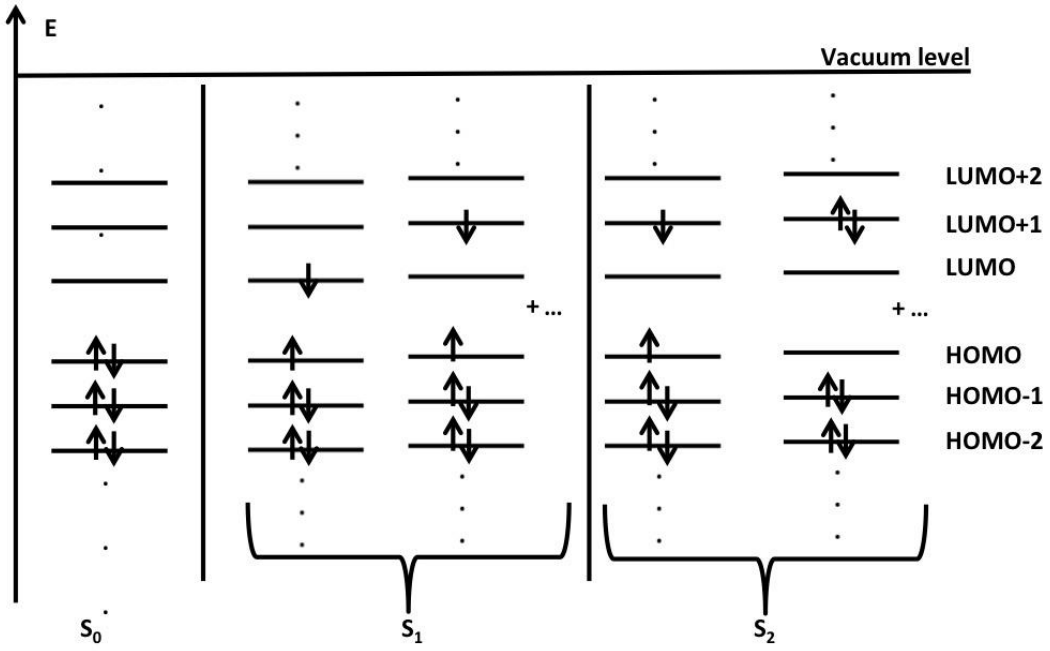

Figure 1.6. An illustration of configurations of electrons associated with different states. The configuration associated the ground state, S_0, is shown, as well as configurations that contribute to the first and second excited state, S_1 and S_2, respectively.

The ground state, S_0, is the lowest possible energy state, and consists of the lowest energy configuration of filled orbitals. Adding energy to the system results in electron configurations of higher energy than S_0. The first excited state, S_1, is higher in energy than the S_0. Promoting an electron from the HOMO to the LUMO can achieve S_1, as can promoting an electron from the HOMO to the LUMO+1 level. There are other possible configurations that can contribute to S_1

as well. The second excited state, S_2, is at a higher energy than the first excited state. As shown in Figure 1.5, S_2 may contain some of the configurations that contribute to S_1, as well as more energetic configurations, such that the energy sum total of S_2 is be greater than S_1.

The last piece of the analysis is the spin state of the energy states (McQuarrie 1997). The spin state is the sum of the individual electronic spins, which may be up or down and have an angular component that adds vectorially. Just as the analysis of electronic orbitals yielded the electronic wavefunction, the analysis of electronic spin yields the spin wavefunction, $\boldsymbol{\varphi}_{spin,}$ which is the sum total spin state of all the electronic spin states. An eigenvalue (i.e. a solution) of the analysis of $\boldsymbol{\varphi}_{spin}$ is $\boldsymbol{S}$, the spin angular momentum. $\boldsymbol{S_z}$ describes the z-component of the spin angular momentum. The electronic spins of paired electrons in orbitals cancel each other out, so only the spins of unpaired electrons in the HOMO and LUMO determine $\boldsymbol{S_z}$ of the spin state. A state in which only one spin configuration yields a value of $\boldsymbol{S_z}$ is considered a singlet state. A state in which three spin configurations yields the same value of $\boldsymbol{S_z}$ is considered a triplet state. An example of this analysis for a two-electron system, which yields 4 possible spin states, is shown in Figure 1.7.

An electron may be excited from a ground state configuration to either a singlet, S_1, or triplet, T_1, excited state configuration, as shown in Figure 1.8. Note that the energy of the LUMO of T_1 is less than the energy of the LUMO of S_1, in order to satisfy Hund's rule.

Electrons in excited state configurations will return to ground state configurations after some time, but only certain pathways are allowed and result in the emission of radiation, as shown in the Jablonski diagram in Figure 1.9.

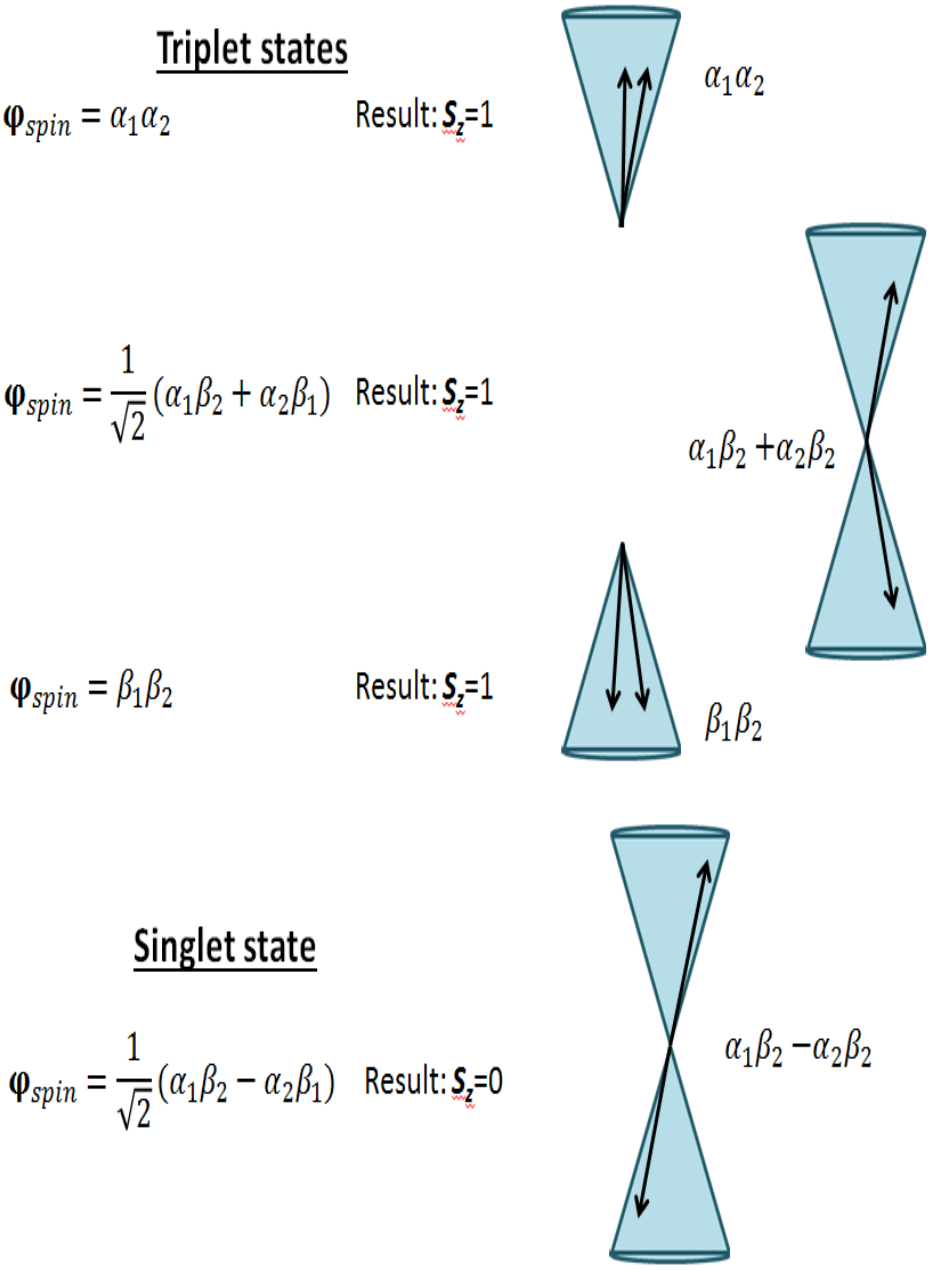

Figure 1.7. Spin states of a two electron system. In this example, α and β are the spin wavefunctions of the electrons, and the labels 1 and 2 refer to electron 1 and 2. The first three spin wavefunctions yield $\boldsymbol{S}_z$=1. These three states together are referred to as a triplet state. The last spin wavefunction yields only $\boldsymbol{S}_z$=0, and is referred to as singlet state. The cone diagrams also illustrate, as indicated by the arrows, how the singlet and triplet states arise as the sum of the z-component of the vectors. Adapted from McQuarrie (1997).

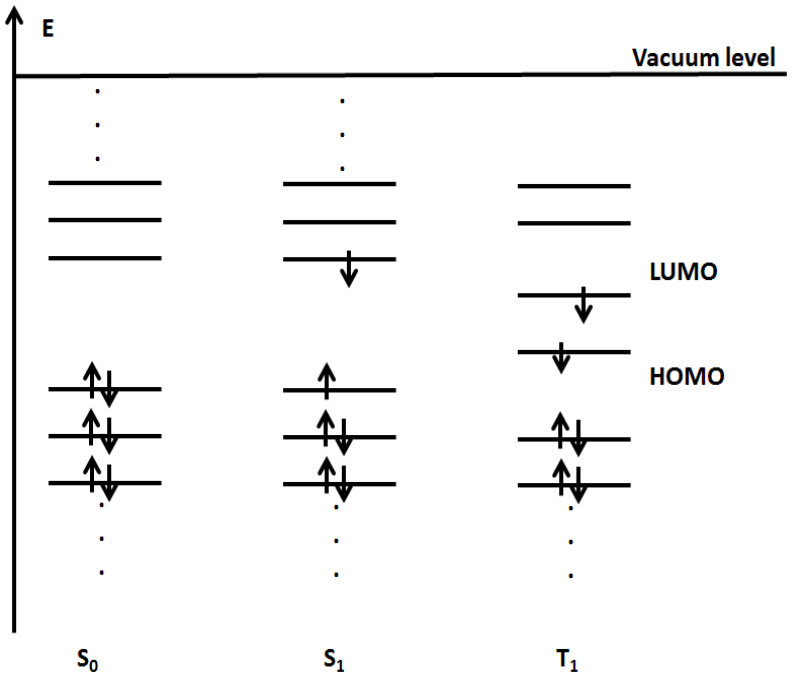

Figure 1.8. Orbital configurations of ground, singlet, and triplet states.

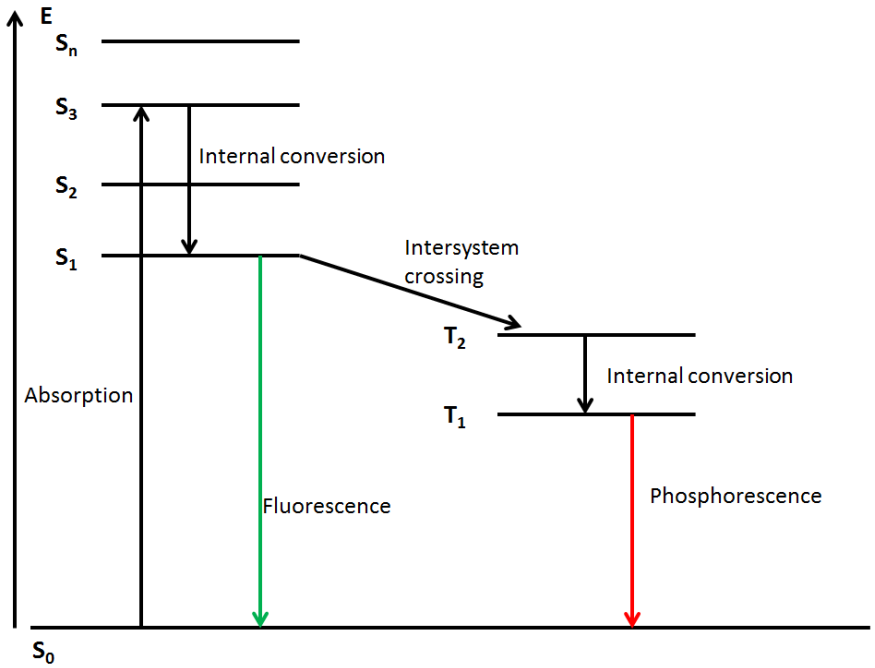

Figure 1.9. A Jablonski diagram illustrating the electronic state transitions that take place in the emission of electromagnetic radiation. Adapted from Skoog (1998).

Absorbed energy excites the electrons from a ground configuration to an excited configuration. The energy gap of the transition depends on the magnitude of absorbed energy. Relaxation from the S_1 state results in emission of electromagnetic radiation, called fluorescence, and relaxation from the T_1 state results in emission of electromagnetic radiation, called phosphorescence (Skoog 1998). Rates of relaxation from excited states to the ground state are determined by the spin wavefunction, $\boldsymbol{\varphi}_{spin}$, and in particular by the integral given by Equation 1.1, in which $\boldsymbol{\varphi}_{spin,\ initial}$ and $\boldsymbol{\varphi}_{spin,\ final}$ are the electron spin wavefunctions of the initial and final configurations, respectively (Skoog 1998).

$$\int_{-\infty}^{+\infty} \varphi_{spin,initial}\varphi_{spin,final} \quad (1.1)$$

The integral in Equation 1.1 only takes on 2 values: it is zero when the spin angular momenta of the initial and final states differ, and it is equal to one when the spin angular momenta are the same. Hence, transitions from S_n to S_0 or T_n to T_1 are spin-allowed, but transitions from T_1 to S_0 are spin-forbidden. However, transitions from T_1 to S_0 are observed due to intersystem crossing, a process in which the spin wavefunction of the triplet state gains some contribution from the spin wavefunction of the singlet state and vice versa (McQuarrie 1997). Intersystem crossing, a non-radiative process, is facilitated by spin-orbit coupling, in which the spin angular momentum, $\boldsymbol{S}$, and the orbital angular momentum, $\boldsymbol{L}$, interact. During transitions, the total angular momentum $\boldsymbol{J}$ must be conserved. If the spin angular momentum and orbital angular momentum couple, then $\boldsymbol{J}=\boldsymbol{S}+\boldsymbol{L}$. During a transition, a change in the spin angular momentum can be offset by an equal and opposite change in orbital angular momentum in order to conserve total angular momentum and facilitate spin-forbidden transitions. Spin-orbit

coupling, and hence intersystem crossing, is maximized when the energy gap between the singlet and triplet state is minimized; in general the S_1 state undergoes more triplet admixture than the S_0, due to a smaller energy gap from T_1 to S_1. Intersystem crossing also depends on the magnitude of the spin-orbit coupling interaction. For molecules, the degree of spin-orbit coupling is proportional to the fourth and fifth powers of atomic charge (McGlynn et al.1964). Hence, strong phosphorescence is observed when heavy metal atoms, such as platinum or iridium, are present in a semiconducting small molecule. The processes required for emission of radiation occur less frequently in phosphorescence than in fluorescence, so rates of phosphorescence are much slower than fluorescence. This results in triplet lifetimes being on the order of milliseconds to hours, compared to nanoseconds for singlet lifetimes.

The last process from Figure 1.9 to be discussed is internal conversion, a different kind of non-radiative process (Skoog 1998). Internal conversion represents transitions between states that have the same spin angular momentum, such as S_1 to S_0 or T_1 to T_0. In this type of process, energy from an excited state is dissipated to the surroundings in the form of vibrational energy.

An OLED is made of a layer or multiple layers of organic semiconductor material sandwiched in between a cathode and an anode. During device operation, a voltage is applied to the device, and electrons are injected into the LUMO of the semiconductor from the cathode and holes are injected into the HOMO from the anode. In the organic layer, electrons and holes combine to form an exciton. The exciton is a short-lived excited state of an electron and hole that are brought together by the electrostatic Columbic force. The exciton may be either a singlet or triplet state. If the exciton decays from the excited state to the ground state by the previously discussed radiative pathways, light is emitted from the device (McQuarrie 1997).

There are a number of ways to characterize the operation of an OLED. A spectrophotometer may be used to measure the emission spectrum of the device, in order to determine the peak wavelength output by the OLED. The current-voltage (C-V) and current-luminance (C-L) of the device may also be measured. C-V measurements require a voltage source, while C-L measurements require a voltage source and a spectrophotometer. The unit for luminance is cd/m^2 (Koshel 2013). C-L measurements are especially important to determine the current needed to turn on and drive the OLED to achieve a required luminance. C-L measurements are made as a function of time in order to determine device lifetime. Lastly, the performance of an OLED may be characterized by its external quantum efficiency (EQE). The EQE is the ratio of the flux of injected current to the flux of emitted photons (Kalyani 2017). The theoretical EQE of an OLED is determined by material properties of the luminescent and charge injecting layers, such as the molecular structure of the materials and composition and quality of the films. Initial OLED devices demonstrated very low EQE's less than 1%, however, due to developments in material deposition and device fabrication schemes, much higher EQE's have been realized (Kalyani 2017).

1.4 The Thin Film Transistor

The proposed multifunctional device features an array of thin film transistors (TFTs). These devices are switches that drive the OLEDs, and are necessary to make the substrate fit into hardware connectors provided by a collaborator. In this section, a general overview of device operation theory, fabrication, and characterization are discussed. A description of TFT fabrication and characterization specific to the multifunctional MEA substrate is presented in Chapter 4.

1.4.1 Description of the TFT

The TFT is a type of field effect transistor (FET) in which components of the device, such as the semiconductor active layer, the dielectric, and the gate, source, and drain contacts, are formed by depositing thin films of materials on an insulating substrate, as shown in Figure 1.10. This is different from ordinary FETs, such as MOSFETS, where the substrate, often a silicon wafer, is the semiconductor active layer of the device.

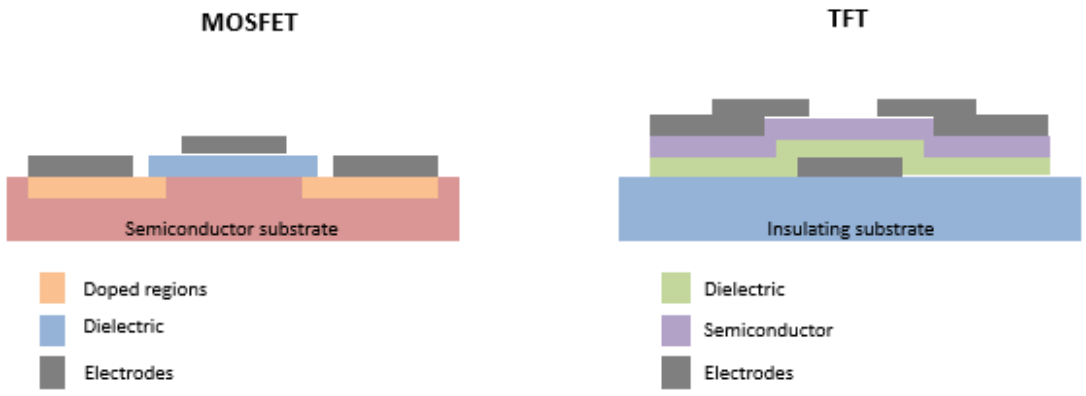

Figure 1.10. A comparison of typical MOSFET and TFT structures.

While there are many device configurations that are possible for a TFT, as seen in Figure 1.11, this work focuses on a bottom gate type device. In this device configuration, there are three electrodes: the gate, the bottom contact, and the source and drain, the two top contacts. A conductive channel is formed between the two top contacts during device operation. The channel length, L, is the distance between the source and drain contacts, while the channel width, W, is the extension of the source and drain, shown in Figure 1.11D.

The devices in this work are operated in accumulation mode, in which increasing the conductivity of the channel occurs by increasing the number of majority charge carriers in the channel (Sze 2007). In a TFT with an n-type active layer, the majority charge carrier is the

electron, while in a p-type device the majority carrier is the hole. The gate contact forms a capacitor structure, where the gate electrode is one plate of the capacitor and is separated from the other plate, the semiconductor layer, by the gate dielectric, an insulating material. When a positive voltage, V_G, is applied to the gate, the electrode is positively charged, which causes electrons to accumulate in the semiconductor layer, forming a conductive channel between the source and drain electrodes. The magnitude of carrier density is directly proportional to the magnitude of V_G. A source-drain voltage, V_{DS}, is applied to the source and drain contacts, where the source is the charge injecting contact and the drain removes charge from the channel.

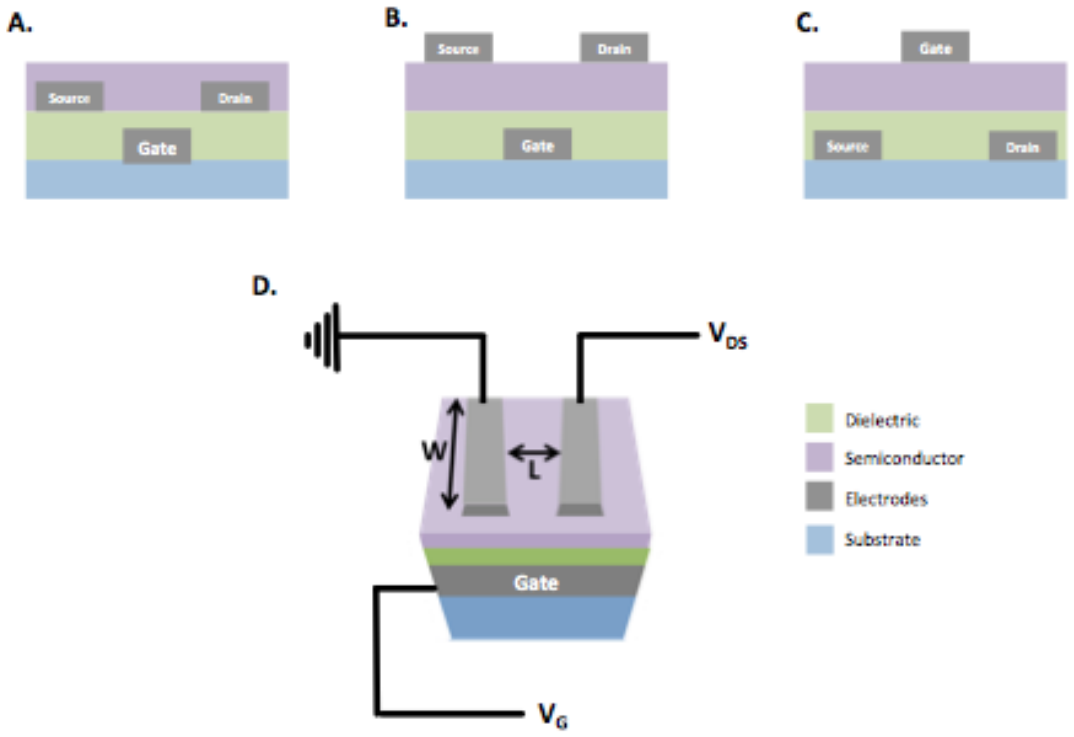

Figure 1.11. Cross-sectional illustrations of TFT structures, including (A) bottom gate-bottom contact, (B) bottom gate-top contact, and (C) top gate-bottom contact. A three-dimensional cross section of a bottom gate-top contact device (D), with applied biases and defined channel dimensions.

In the bottom gate configuration, the gate contact, made from a conductive material, is deposited and photolithographically patterned on the substrate. In subsequent layers and processing steps, the gate dielectric and semiconductor are deposited and patterned. The gate dielectric may be either an organic or inorganic insulator material. The semiconductor may be organic or inorganic as well. Finally, the source and drain ohmic contacts are deposited on the top of the device stack. The dimensions and locations of these contacts may be defined by shadow mask deposition, or by photolithography if the semiconductor is properly passivated.

For the MOSFET, device materials are chosen to optimize application-specific transistor performance. This usually comes at the cost of high processing temperatures and expensive methods for depositing the device materials. However, the TFT has found specialized applications in low cost, large area, and flexible applications, so materials are chosen for unique properties that allow the TFT to be utilized in novel applications (Correia 2016). Transparent metal oxides may be used for transparent contacts for an all-transparent device, common in display technologies (Wang et al. 2007). Or, if devices will be fabricated on a flexible polymer substrate, materials that can be processed at temperatures below the glass transition temperature of the substrate are ideal (Nomura et al. 2004).

1.4.2 TFT operation and characterization

TFTs operate in either enhancement or depletion mode, which is determined by the sign of the threshold voltage, V_T (Sze 2007). For enhancement mode TFTs, when V_G=0, the device is "off," and no current flows between the channel at the semiconductor-gate dielectric interface. As V_G becomes more positive, more charge accumulates in the channel. For depletion mode

TFTs, the device is "on" at V_G=0, and decreasing the value of V_G decreases the number of carriers in the channel, until the device is "off." This section will describe the operation of n-type TFTs operated in enhancement mode, since those devices are used in this work.

The operation of the TFT is described by three different regimes of channel conductivity, as illustrated in Figures 1.12 and 1.13 (Sze 2007). In the sub-threshold regime, the device is "off" as there is negligible current flow in the channel. In this regime, $V_G<V_T$. In the linear regime, the device is "on." There is charge flowing between the source and drain contacts at the interface of the active layer and the gate dielectric. In this regime, $V_G>V_T$, and $V_{DS}<(V_G-V_T)$. Lastly, in the saturation regime, the "pinch off" of the channel forms, limiting the amount of current at the drain. Current depends more on V_{DS} than V_G in this regime, where $V_G>V_T$ and $V_{DS}>(V_G-V_T)$.

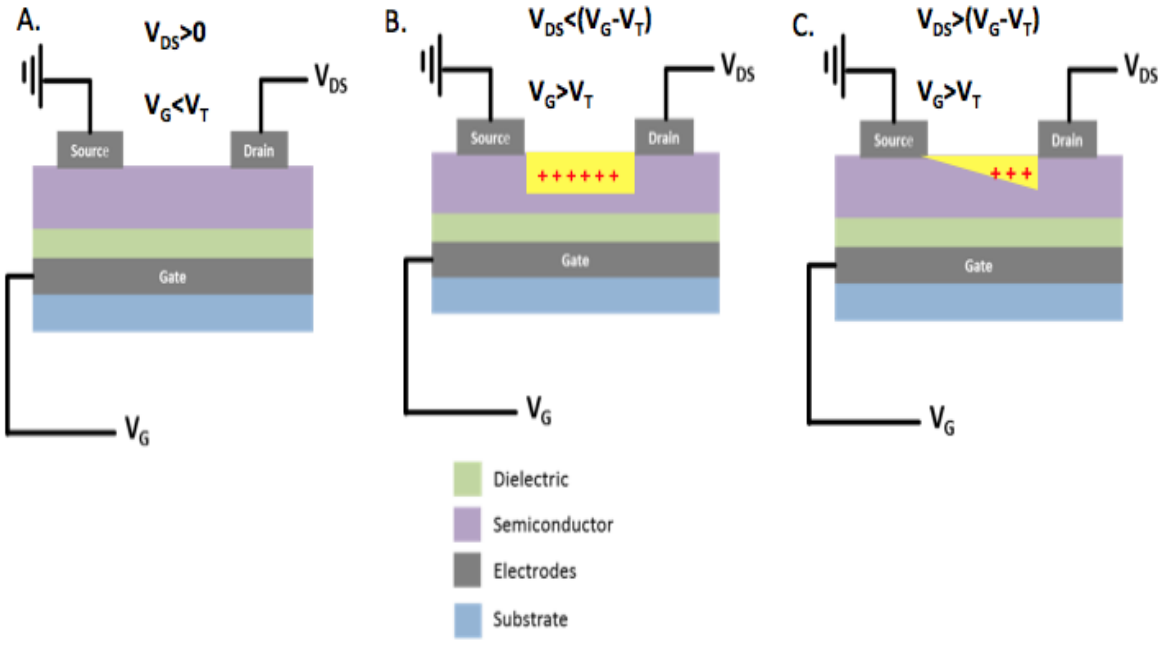

Figure 1.12. TFT operation regimes, including the (A) substhreshold, (B) linear, and (C) saturation regime.

Crucial TFT device performance characteristics are the on/off ratio, V_T, the threshold voltage at which the device is "on," and the field effect mobility of charge carriers, μ_{sat} (Sze 2007). These three values can be obtained from the transfer curve. This is a plot of current measured at the drain, I_D, while V_G sweeps through a range of values. The on/off ratio is straightforward to obtain from this plot, as it is the ratio of current in the "off" regime (V_G=0) and the current in the "on" saturation regime (V_G>V_T), as seen in Figure 1.13C. This value indicates the switching ability of the device, and a low "off" current is highly preferred for enhancement mode devices.

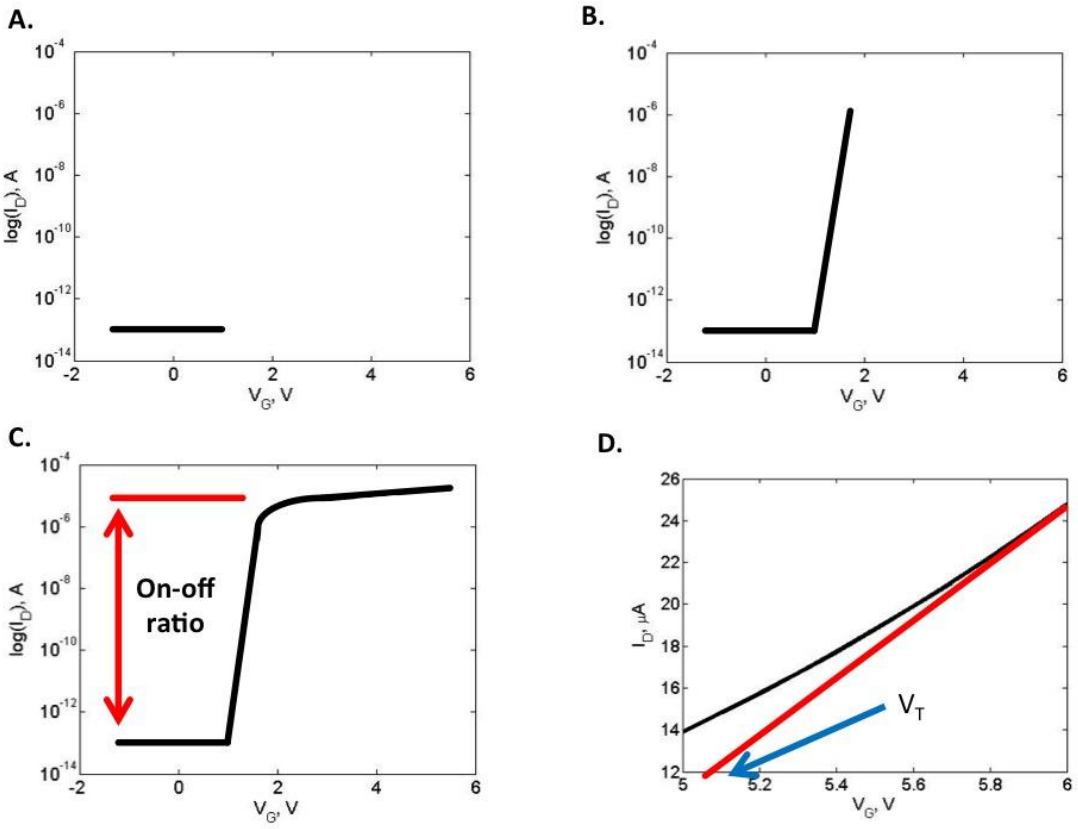

Figure 1.13. TFT transfer curves at different operation regimes, including the (A) subthreshold regime, (B) linear regime, and (C) the saturation regime. In (C) the determination of on-off ratio, and in (D) determination of V_T are demonstrated.

Obtaining V_T and μ_{sat} requires algebraic manipulation of the data from the output curve. In the saturation regime of device operation, $V_{DS}>(V_G-V_T)$ and device operation is linear. In this regime, the drain current I_D is given by the following equation:

$$I_D = \frac{W}{2L} C_i \mu_{sat} (V_G - V_T)^2 \qquad (1.2)$$

Where W is the channel width, L is the channel length, C_i is the capacitance per unit area of the gate dielectric, μ_{sat} is the field effect mobility in the saturation regime, V_G is the gate voltage and V_T is the threshold voltage. From Eq. 1.2, it can be seen that V_T may be obtained by plotting $\sqrt{I_D}$ versus V_G; V_T is the x-intercept of this plot at $\sqrt{I_D} = 0$. Taking the square root of both sides of the equation yields a linear equation of the form y=mx+b.

$$\sqrt{I_D} = \sqrt{\frac{C_i \mu_{sat} W}{2L}} V_G - \sqrt{\frac{C_i \mu_{sat} W}{2L}} V_T \qquad (1.3)$$

$$m = \sqrt{\frac{C_i \mu_{sat} W}{2L}} \qquad (1.4)$$

Hence, if the slope, m, is extracted from the plot, and C_i, W, and L are known values, then μ_{sat} can be calculated (Sze 2007).

1.5 Patterned Polystyrene-Based MEA

The final component of this dissertation is work that demonstrates the development of processes for depositing and patterning polystyrene electrode insulation film on the MEA. The ultimate goal for this project is to eventually pattern thick films of polystyrene, such that the film insulates the electrodes, and corrals or partitions a plated cell culture in three-dimensional

microfluidic structures. We demonstrate a proof of concept MEA that features a 500 nm thick polystyrene insulating film. The rationale for using polystyrene as the encapsulation material is two-fold. While the vast set of MEAs that are available in academic and commercial settings are encapsulated with a variety of organic or inorganic materials, none of these materials are as familiar as polystyrene to *in vitro* cell culture work. Working with a vast, unfamiliar material set requires users to develop complicated protocols for preparing the MEA surface for tissue plating. Also, while several works have demonstrated interfacing microfluidic structures with an MEA platform, these structures were achieved with soft materials, such as hydrogels or polydimethylsiloxane (PDMS). These materials are attractive to work with, as they are easily and rapidly patterned, however, they present challenges that are detrimental to the viability of a plated cell culture (Berthier et al. 2012).

1.5.1 Previous work with cell culture microfluidics

The possibility of *in vitro* biological experiments was first realized in the early 1900's, when embryonic frog nerve fibers were cultured in a glass dish (Harrison 1911). This work started a new avenue of biological research. Over the next few decades, methods for sterile *in vitro* cell culture were developed and standardized, and cell culture itself found new applications as it grew into a legitimate research field. A commonality to the work in the early years of cell culture work was the use of glass culture ware. The high cost of the glassware was a factor that potentially limits users from adopting *in vitro* cell culture techniques. Because of the cost, glassware is not treated as a single-use or disposable apparatus, which introduces laborious cleaning steps into cell culture protocol. However the development of the plastics industry introduced new materials in cell culture work during the 1950's. Many plastics had properties

such as optical clarity, mechanical strength, and durability that rivaled glass. Development of high-volume manufacturing processes made plastic beakers, culture flasks, and petri dishes much cheaper than their glass counterparts, to the extent that these containers and apparatuses became single-use and disposable. When Falcon Plastics developed oxygen plasma surface treatments to render polystyrene more hydrophilic, polystyrene replaced glass as the material of choice for *in vitro* cell culture work (Young et al. 2011).

A new interest in interfacing microfluidics with cell culture in the 1990's brought about a renewed interest in exploring different materials for cell culture. Cell culture microfluidics were driven by the idea of micro total analysis (μTAS) and lab-on-a-chip (LOC) substrates that could reduce traditional laboratory equipment to miniature platforms (Manz et al. 1990). Microfluidic substrates promised inexpensive alternatives to traditional cell culture experiments and analysis, such as electrophoresis and chromatography. Additionally, as these small substrates reduce the number of cells needed for an experiment, they act as platforms that are able to capture the perturbations of a few or even single cells, which is useful in elucidating mechanisms for cell processes such as locomotion. However, in order for these goals to be realized, processes for fabricating microfluidic channels must be developed. Early on, labs that were best equipped to do this work had access to costly microelectronic fabrication toolsets that were able to pattern the necessary micron-sized features in substrates such as glass or silicon. Just as the cost of glass was a limiting factor in the early days of *in vitro* biology, the cost of substrate fabrication limited the broad adoption of microfluidic cell culture. The emergence of soft lithography has since revolutionized microfluidics (Duffy et al. 1998). PDMS is a soft, silicone polymer that can be patterned by soft lithography techniques such as stamping or molding, followed with a thermal

cure. These fabrication techniques eliminate the need for costly microfabrication equipment, and allows for rapid prototyping of microfluidic devices. A limited number of similar soft polymeric materials, such as agarose, are also amenable to soft lithography techniques, and have found application in microfluidics (Moffitt et al. 2012)

The types of experiments performed with microfluidic cell culture and the results have been numerous, and images of different types of microfluidic cell culture structures are shown in Figure 1.14.

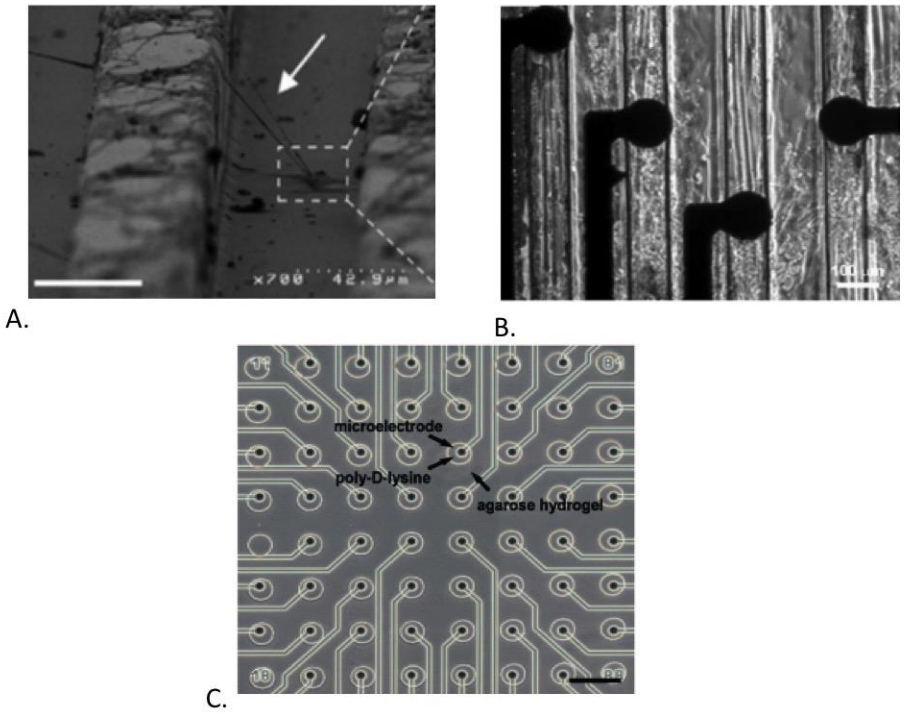

Figure 1.14. Images of microfluidic cell culture from literature, including (A) neurons cultured in the trough of PDMS microgrooves, reprinted from work by Lien et al. (2013), (B) PDMS microgrooves interfaced with MEA electrodes, reprinted from work by Langhammer et al. (2013), and (C) an array of agarose wells interfaced with MEA electrodes, reprinted from work by Kang et al. (2009).

For example, some work in this field focuses on determining mechanisms of neurite growth guidance. While investigators are aware of chemical cues that guide growth, it is not

clear how physical obstacles influence the growth of neurites and axons. In these types of papers, neuronal tissues are cultured on substrates that feature PDMS microgrooves of various dimensions (Goldner et al. 2006; Lien et al. 2013). The tissues are plated in the trough of grooves, and tissue growth, either in the presence or absence of growth-guiding chemicals, can be observed with optical microscopy or other analytical techniques, as shown in Figure 1.14A. More relevant to the focus of this project, investigators have also interfaced microfluidic cell culture with MEAs. Similar to the work with PDMS microgrooves, these works interface PDMS microfluidic features on the surface of the MEA, in order to establish and maintain tissue growth patterns with respect to the location of substrate electrodes, as seen in Figure 1.14B (Langhammer et al. 2013). Alternatively, microfluidics has also been interfaced with an MEA in an effort to construct a high throughput drug-screening platform (Kang et al. 2009). On a conventional MEA, only one experimental condition may be tested in an experiment, as all tissue in the plated culture is exposed to chemicals introduced into the cell culture ring. However, this work interfaces the MEA surface with an agarose film that is molded into an array of wells, shown in Figure 1.14C. Each well encircles a single MEA electrode and has a volume of several thousand cubic microns, to which experimental reagents may be added. Each well physically isolates an electrode from its neighbors and no neurons grow in the agarose space bridging the wells. Hence, the agarose well array creates a multiwell experiment platform on the surface of a conventional MEA.

1.5.2 The need for alternative materials for microfluidic cell culture

While the works with microfluidic cell culture are very novel and the results non-trivial, it is important to realize that the materials, such as PDMS and agarose, used to construct the

microstructures are not without significant drawbacks (Berthier et al. 2012). These material disadvantages impede successful and repeatable cell culture, and outweigh the ease of patterning and prototyping.

One disadvantage of these materials is low stiffness. For example, PDMS has an elastic modulus of 1-3 MPa, depending on cure conditions and crosslinking density (Wang et al. 2014) The elastic modulus of agarose can vary from 100-1000 kPa, depending on the viscosity of the monomer solution and curing conditions (Normand et al. 2000). For either material, the elastic modulus is significantly smaller than glass, which varies from 50 to 150 GPa, depending on composition, or thermoplastics, such as polystyrene which has a modulus that varies from 3 to 3.5 GPa, depending on the molecular weight of the monomer (Makishima and Mackenzie 1973; Wypych 2012). In the case of the previously discussed microgroove work, soft materials can experience deformation of grooves and high aspect ratio microfeatures. In work that involves pressure-driven flow conditions, soft PDMS microchannels may bulge. Some work has attempted to address the compliance of PDMS by optimizing the mixing ratio of monomers, crosslinking density, curing temperature and time, which improves deformation, but increases variability in PDMS preparation from substrate to substrate and across laboratories (Gervais et al. 2006; Park et al. 2010).

PDMS also has high permeability to gases. The permeability of oxygen in bulk PDMS is reported to be 2,000-4,000 $\mu m^2\ s^{-1}$ (Charati and Stern 1998; Saito et al. 2006). This value is three orders of magnitude larger than the diffusion rate of oxygen in polystyrene (2 $\mu m^2\ s^{-1}$), but very similar to the diffusion rate of oxygen in aqueous media (3,000 $\mu m^2\ s^{-1}$). Initially, this may seem like an advantage, as O_2 and CO_2 diffusion from cells is crucial in cell culture, especially in

chronic experiments. However, the diffusion rates in bulk PDMS and cell culture media are very similar, meaning that the oxygen content in a microfluidic device, with a total height of a few hundred microns, may actually be higher than in a conventional macroscale cell culture with a height of media of a few millimeters. This high oxygen concentration may stress the cell culture (Gewandter et al. 2009; Tang et al. 2010). In addition to oxygen permeability, PDMS has a high permeability for water vapor at about 1,000-6,000 $\mu m^2 s^{-1}$, which causes evaporation issues (Heo et al. 2007). As water diffuses from the culture media into the PDMS structures, this can significantly shift the volume of media and change concentrations and gradients of media chemicals that are crucial to the experiment. The loss of media volume can also cause air bubbles that can block fluid flow or lyse cells. A solution to these issues would be to coat the PDMS with a less permeable material, such as parylene (Young et al. 2003). However, this is an added fabrication step that requires a specialized toolset. Additionally, the investigator is now charged with plating tissue on a parylene surface, rather than a PDMS surface, which requires a different cell culture protocol.

In addition to being permeable to O_2, CO_2, and water vapor, PDMS is also permeable to hydrophobic compounds. Compound absorption is not unusual for materials used in microfluidic fabrication such as glass and thermoplastics, however these materials demonstrate only surface adsorption of small molecules. PDMS is prone to bulk absorption of these molecules, which can drastically decrease the concentration of experimental reagents in culture media (Toepke and Beebe 2006). It has been demonstrated that, compared to polystyrene microfluidics, PDMS bulk absorption of these small molecules produces artifacts in results, which can be detrimental to cell-based fundamental biology studies and new drug screens (Regehr et al. 2009; Su et al.

2013). Again, it is possible to mitigate absorption by coating PDMS in parylene (Sasaki et al. 2010). However, this is another step that complicates substrate fabrication and cell culture.

Similar to the issues of absorption and permeability is the leaching of unreacted material from the PDMS structures. Cured PDMS contains residual uncrosslinked polymer chains that leach out of the microfluidic structures and into culture media. It has been shown that this unreacted material can incorporate into cell membranes (Regehr et al. 2009). Several cycles of washing with organic solvents can reduce the amount of unreacted oligomer, but cannot eliminate this contamination entirely (Lee et al. 2003). Parylene coatings may also control leaching, but this comes with the same previously discussed disadvantages.

Lastly, PDMS exhibits hydrophobic recovery, which also impedes development of microfluidic cell culture. While PDMS is hydrophobic, the surface can be modified by exposure to oxygen plasma. In the presence of O_2 plasma, the PDMS surface is functionalized with hydroxyl groups, rendering the surface hydrophilic, which serves a variety of purposes in microfluidic cell culture, such as improving bonding between dissimilar materials, permitting further surface functionalization required by tissue culture protocols, and facilitating aqueous filling of microfluidic channels. However, as previously stated, there are unreacted polymer chains in the bulk PDMS that can diffuse freely. These chains may diffuse to the surface and replace hydroxyl groups, rendering the surface hydrophobic (Eddington et al. 2006). Minimizing the amount of time in between plasma surface treatment and substrate use is a strategy used to mitigate the rate of hydrophobic recovery, but it does not necessarily prevent recovery from occurring during cell culture. The rate of recovery is difficult to control or predict, and limits the ease-of-use and manufacturability of ready-to-use microfluidic substrates.

1.5.3 Polystyrene as an alternative material for microfluidic cell culture

As previously stated, polystyrene is ubiquitous in macroscale *in vitro* cell culture, and work has explored the possibility of employing this material in microfluidic cell culture. To date, photolithographic patterning and etch processes have not been utilized for polystyrene microfluidic fabrication. The current approach has been to adapt polystyrene to soft lithography processes, such as injection molding or hot embossing (Chin et al. 2011; Goral et al. 2011; Tung et al. 2011; Young et al. 2011). In these works, a master mold or stamp is fabricated. Negative-relief molds are fabricated by computer numerical control (CNC) milling or laser machining. Positive-relief molds may be made out of PDMS or epoxy patterned on a glass, fused silica, or silicon substrate. In hot embossing techniques, polystyrene is first dissolved in a solvent. Then the polystyrene solution is cast on a rigid carrier substrate, and the master is brought into conformal contact with the carrier. The master is clamped down onto the carrier and the master-sample substrate is thermally cured to evaporate solvent. After the thermal cure the polystyrene part is released from the mold. In injection molding techniques, a polystyrene film is brought into contact with a heated master, which deforms the film into the shape of the master. The molding technique may be gas-assisted in order to stretch the polystyrene film into voids in the master pattern. When the master cools, the polystyrene part is demolded.

In these referenced works, the fabricated polystyrene part is a stand-alone apparatus, so bonding the polystyrene microfeatures with features on another component is not critical. But bonding is an issue if the polystyrene part is to be coupled to another apparatus or substrate, such as an MEA. However, bonding a polystyrene part to another substrate is not a trivial task. Temperature-assisted bonding methods that have been used to bond thermoplastic parts, are not

applicable to polystyrene, as high-aspect ratio features may deform well below the polystyrene glass transition (T_g) temperature of 100 °C. Solvent-bonding methods, in which a small amount of organic solvent is used to solubilize the surface of the polystyrene part to be bonded, have been reported to create strong bonds, however, feature deformation is still a risk and residual solvent may contaminate cell culture media. Thermal diffusion bonding has been explored as an alternative strategy. In this method, low heat and high pressure are applied to the polystyrene part and the substrate, which promotes reorganization and entanglement of polystyrene chains at the substrate interface, which forms a bond. However, feature deformation may still be a risk, due to applied heat. In short, a method for reliably bonding a polystyrene part to an MEA substrate in a way that maintains the dimensions of the part has not been demonstrated.

An alternative strategy to interfacing polystyrene microfluidics with the MEA surface would be to deposit the polystyrene directly on the surface of the MEA and use photolithography and plasma etch processes to pattern the film. Provided that there is good adhesion between the substrate and the polystyrene film, microfeatures may be patterned directly on the MEA substrate. However, polystyrene has limitations that are not amenable to standard photolithographic processing. The T_g, for polystyrene is 100°C, which is not compatible with the standard photolithographic processes in use at UT Dallas, which have resist cure temperatures of 115°C. A fabrication scheme that utilizes processing temperatures at or below 100 °C is presented in this dissertation. Also, polystyrene is soluble in some organic solvents and incompatible with others. During the photoresist deposition step in a standard photolithography process, the polystyrene film will come into contact with solvents in the resist, which may crack

or wash away the film. A strategy to protect the polystyrene film with a solvent-impermeable SiO_2 hardmask is also demonstrated in this dissertation.

1.6 Structure of the Dissertation

The following chapters of the dissertation are structured as follows:

a) Chapter 2 presents a fabrication process for an MEA on a flexible substrate developed at UT Dallas, and compares the performance and stability of the flexible MEA to commercially available MEAs in an *in vitro* cell culture application.

b) Chapter 3 presents a fabrication process for a blue OLED and characterizes the device in terms of color, brightness, and lifetime.

c) Chapter 4 presents a fabrication process for a TFT that can potentially drive the blue OLED fabricated in Chapter 3. The performance of the TFT is characterized in terms of drive current and V_T stability

d) Chapter 5 discusses the integration methodology developed in this dissertation for the fabrication of MEA, OLED, and TFT components on a single multifunctional substrate for *in vitro* optogenetic experiments.

e) Chapter 6 demonstrates the development, characterization, and fabrication of an MEA with polystyrene electrode encapsulation. The polystyrene film is deposited, patterned, and etched using processes that are common to semiconductor processing. MEA devices are evaluated in a cell culture experiment where cell culture viability and neural recordings are demonstrated.

f) Chapter 7 concludes the dissertation with summaries of the work in previous chapters and discussions of future tasks for the projects presented in this work.

CHAPTER 2

NOVEL DISPOSABLE MICROELECTRODE ARRAY FOR CULTURED NEURONAL NETWORK RECORDING EXHIBITING EQUIVALENT PERFORMANCE TO COMMERCIALLY AVAILABLE ARRAYS

Microelectrode arrays (MEAs) enable non-invasive recording of supra-threshold signals, i.e. action potentials or spikes, from a variety of cultured electrically active cells. While this label-free technology has been shown to be useful for pharmacological and toxicological studies, a major limitation has been the reliance on expensive recording substrates that have been manufactured with the intent of re-use (Giovangrandi et al. 2006; Hämmerle et al. 1994; Novak and Wheeler 1986). Prior work by our group has demonstrated an approach for fabricating MEAs using conventional liquid crystal display manufacturing techniques. Here, we describe and characterize the UT Dallas planar MEA which is fabricated with low cost materials and processes. We compare the performance of the UT Dallas MEAs, which consist of exposed gold microelectrodes with patterned parylene insulation over traces, with well-established commercially available MEAs using cultured murine cortical networks. Detailed electrophysiological comparisons show virtually identical performance between MEA types with respect to network metrics including: recording yield across the array, network spike rate and burst rate, and virtually identical pharmacological responses to a diverse set of neuropharmacological agents.

This work was a collaborative effort between research groups at The University of Texas at Dallas and George Mason University that resulted in a publication. This chapter is reprinted from

the Journal of Sensors and Actuators B: Chemical, Volume 226, Hamid Charkhkar, David Arreaga-Salas, Thao Tran, Audrey Hammack, Walter Voit, Joseph Pancrazio, and Bruce E. Gnade, "Novel disposable microelectrode array for cultured neuronal network recording exhibiting equivalent performance to commercially available arrays", Pages No. 232-238, Copyright (2016), with permission from Elsevier. The lead author on the publication was Mr. Charkhkar, who also performed the cell culture work at George Mason University. Mr. Arreaga-Salas performed electrode electroplating at UT Dallas. Ms. Hammack fabricated the MEA substrates at UT Dallas. Ms. Tran carried out the electrical impedance stability measurements at George Mason University. Dr. Voit, Dr. Gnade, and Dr. Pancrazio were the principal investigators that oversaw this work. Dr. Voit and Dr. Gnade were at the UT Dallas, while Dr. Pancrazio was at George Mason University.

2.1 Introduction

Neuronal networks cultured on planar microelectrode arrays (MEAs) have utility in a wide range of *in vitro* applications including neuropharmacology (Johnstone et al. 2010; Keefer et al. 2001a; Morefield et al. 2000; Xiang et al. 2007), assessing biocompatibility of novel materials (Charkhkar et al. 2014), studying neural network plasticity (Bakkum et al. 2008; Chiappalone et al. 2008; Hamilton et al. 2013), connectivity (Poli et al. 2015), and response to electrical stimulation (Ide et al. 2010; Wagenaar et al. 2005), as well as the emergence of dynamic states (Massobrio et al. 2015; Tetzlaff et al. 2010). Murine primary cultures derived from embryonic neural tissue mature to form spontaneously active networks on the surface of MEAs. In fact, the use of cultured cortical tissue on MEAs for pharmacological assays has been cross-validated across multiple laboratories (Novellino et al. 2011). Compared to other

electrophysiological assays or imaging approaches, MEAs offer label-free, non-invasive, and long-term recording capabilities.

To create MEAs with features on the order of tens of microns, fabrication processes and materials common in the silicon microelectronics industry are used. Common conductive materials comprising MEAs include indium tin oxide (ITO), platinum, gold, or titanium nitride, whereas the insulating materials include SU-8, silicon nitride, polymimide, parylene, or PDMS. Advances in MEA technology have mainly focused on increasing spatial resolution and channel density through the incorporation of on-chip CMOS electronics (Heer et al. 2004; Heer et al. 2006; Tateno and Nishikawa 2014). Unfortunately, MEAs are typically expensive, fragile, and consist of materials that are distinctly different from conventional polystyrene culture dishes used and discarded in typical cell biology laboratories. Manufacturers expect re-use and specialized handling of these devices.

We previously reported on the application of liquid crystal display fabrication technologies to create a low-cost functional MEA (Charkhkar et al. 2012) that made use of gold microelectrode contacts and traces insulated with parylene-C, a biocompatible polymer often used in implantable device applications (Kim et al. 2009; Schmidt et al. 1988; Takeuchi et al. 2005).

In this chapter, we report on reproducible fabrication of low-cost MEAs leveraging our fabrication process that exhibits stable electrochemical impedance profiles of gold contacts and conducting polymer modified sites under culture conditions. We show that the performance of these MEAs with respect to cultured neuronal network recording is entirely consistent with that from well-established commercially available MEAs from Multi Channel Systems (Reutlingen,

Germany). Our data show that the UT Dallas MEAs offer a platform for low-cost, disposable high content assays from neuronal networks.

2.2 Methods

2.2.1 Fabrication and Characterization

An array of 60 gold square microelectrodes with a side length of 30 µm was patterned on the substrate with parylene-C insulation over the leads. The outer dimensions of the array substrate were 3.8 cm x 3.8 cm with 2 mm x 2 mm bond pads separated by 400 µm. As shown in Figure 2.1, the substrate was a 500 µm thick layer of polycarbonate, a stiffer material than polyethylene naphthalate used previously (Knaack et al. 2013), which improves ease of handling.

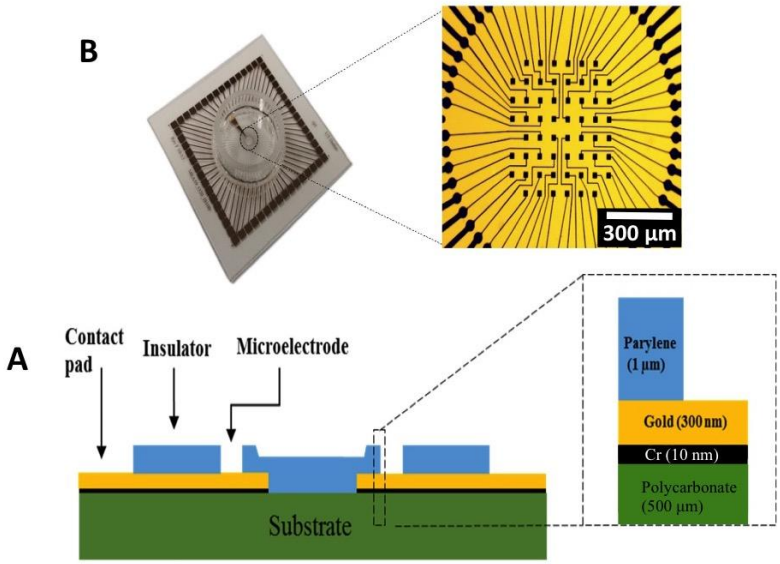

Figure 2.1. A cross-sectional drawing of the UT Dallas MEA showing the different layers, thicknesses, and the material used in each layer (A). An optical image of the MEA with magnification showing the microelectrodes (B).

The gold microelectrodes were deposited by e-beam evaporation and patterned using standard photolithography and wet etch. Parylene-C was deposited by chemical vapor deposition and then exposed to oxygen reactive ion etching for patterning. Refer to Appendix A for a complete fabrication process flow.

Electrochemical characterization of the MEA was performed using electrochemical impedance spectroscopy (EIS) on individual microelectrodes from a typical array. The measurements were performed using a two-electrode setup using a potentiostat/galvanostat (CH 600D, CH Instruments, Texas, US) equipped with an electrochemical analyzer module (CHI Version 9.03, CH Instruments). Measurements were made in the presence of phosphate-buffered saline (PBS) at pH of 7.4 at room temperature by applying a sinusoidal signal with 20 mV amplitude over a range of frequencies from 10 Hz to 100 kHz to characterize the complex impedance of the working electrode and the electrolyte solution.

2.2.2 MEA Preparation and Cell Culture

Commercially available MEAs from Multi Channel Systems (Reutlingen, Germany), model MCSMEA-S2-GR which consist of 60 ITO microelectrodes, were used for comparison with the novel MEAs. Microelectrodes had a diameter of 10 - 30 µm and inter-electrode spacing of 200 µm. As described in (Charkhkar et al. 2014), MCS MEAs were first disinfected using 70% ethanol for 20 minutes under laminar flow in a biohood and then rinsed with sterile de-ionized water. To obtain better cell adhesion, the center regions of the MCS MEAs were coated with 50 µg/ml of poly-D-lysine (PDL) (Sigma-Aldrich, St. Louis, MO) overnight. After the incubation with PDL, the arrays were then washed with sterile deionized water three times to remove any excess PDL. The arrays were then coated at the center with 20 µg/mL of laminin

(Sigma-Aldrich, St. Louis, MO) for at least an hour. Prior to the cell seeding the laminin was removed from the MCS MEAs.

Small, yet important modifications to the above preparation steps enabled immediate and reliable use of the UT Dallas MEAs for cell culture. First, UT Dallas MEAs were exposed to oxygen plasma treatment with the O_2 pressure of 15 psi for 1 min at 75 W (PE-50, Plasma Etch Inc., Carson City, NV). UT Dallas MEA wells were filled with PBS and allowed to soak for 24 hours at room temperature. Under a biological containment hood, UT Dallas MEA wells were treated with 70% ethanol for 20 min, washed with sterile water, filled with cell culture medium consisting of DMEM (Life Technologies), 2% B27 (Life Technologies), 5% horse serum (Atlanta Biologicals, Lawrenceville, GA), 5% fetal bovine serum (Life Technologies), and 0.2% 4mg/ml ascorbic acid (Sigma Aldrich) and incubated overnight at 37 °C in the cell culture incubator. After removal of the culture medium, ~50 µl of 50 µg/ml of PDL was applied to the center of each UT Dallas MEA recording well and allowed to incubate at 37^{o}C in a CO_2 incubator overnight, with care taken to avoid evaporation. Approximately 2-3 hours prior to cell plating, PDL was washed from the recording wells three times with sterile water and the surface was allowed to dry. Finally, ~50 µl of 20 µg/ml of laminin was applied for at least 1 hour with the excess removed immediately prior to plating. Pilot experiments revealed that strict adherence to the above preparatory steps enabled reliable adhesion of dissociated primary embryonic cortical tissue and subsequent maturation into active networks.

The primary neuronal culture method was similar to that described in (Knaack et al. 2013). The procedure was approved by the Institutional Animal Care and Use Committee of George Mason University (Fairfax, VA). Timed pregnant, embryonic day 17, CD-1 mice

(Charles River, Wilmington, MA) were euthanized with carbon dioxide followed by decapitation. Embryos were extracted in ice cold L15 (Life Technologies, Grand Island, NY). Upon isolation of the frontal cortex, the tissue was stored up to 24 hours in a hibernate media (BrainBits, Springfield, IL) supplemented with 2% B27 (Life Technologies) and 0.5 mM Glutamax (Life Technologies), Later, the hibernate media was removed, the tissue was minced by scalpels and then dissociated through incubation with DNAase and papain (Worthington Biochemical Corp., Lakewood, NJ) for 15 minutes followed by mechanical trituration using disposable graduated pipettes (Fisher Scientific, Pittsburg, PA). After centrifuging at 2500 rpm for 5 minutes, the supernatant was removed and cells were re-suspended in culture medium. The cells were counted using a hemocytometer (Life Technologies) and immediately seeded on MEAs at a density of 100,000 in a 50 μL droplet. All cultures were incubated at 37°C with 10% CO_2 and maintained in DMEM with GlutaMAX supplemented with 5% horse serum (Atlanta Biologicals), 5% FBS (Life Technologies), 2% B27, and 0.2 % of 4 mg/ml ascorbic acid (Sigma-Aldrich) for the first two days. To avoid overgrowth of glial cells, the fetal bovine serum was removed at day 3 and the cultures were thereafter maintained by a 50% media exchange twice a week for at least 21 days.

2.2.3 Extracellular Recordings and Analysis

All recordings were performed after at least 3 weeks *in vitro* to ensure that the neural networks had reached maturity and consistency in activity. The multichannel extracellular recordings were acquired with an OmniPlex data acquisition system (Plexon Inc., Dallas, TX),

where each of the 60 channels of either MEA was digitized at a sampling frequency of 40 kHz. During the recording session, the culture temperature was controlled at 37 °C.

During extracellular recordings from the neuronal networks, the mean noise level was calculated for each individual channel and a threshold was set at 5 standard deviations from this mean. A spike was then detected if the signal surpassed this threshold. Channels were considered to be active if the spike rate was at least 0.1 Hz. The recorded spikes from each channel were sorted off-line into well-resolved units using Offline Sorter V.3 (Plexon Inc.). The spike sorting method was based on the 2D principle component analysis of spike waveforms followed by scanning K-Means to find and separate between clusters. Each unit presumably corresponds to the signal from an individual neuron. Consistent with (Shafer et al. 2008), a burst was defined as the occurrence of a minimum of 4 spikes which were not more than 75 ms apart from each other. The minimum inter-burst interval was set to 100 ms.

2.2.4 Pharmacological Exposure

For a subset of experiments, the pharmacological sensitivity of the cultured neuronal networks on the MCS and novel MEAs was examined. In separate comparison experiments, we applied the following compounds to the cultures on both MEA platforms: 20 µM memantine (Sigma -Aldrich), a blocker of excitatory N-methyl-D-aspartic acid (NMDA) receptors, 1 mM pilocarpine (Sigma –Aldrich), a muscarinic cholinergic receptor agonist, 5 µM amyloid beta ($A\beta_{1\text{-}42}$) monomer (Anaspec, Fremont, CA), a biomolecule associated with Alzheimer's disease, and 5 µM bicuculline, a blocker of $GABA_A$ receptors. The comparative effects of all the compounds were examined under acute conditions.

2.3 Results and Discussion

2.3.1 Microelectrode Impedance Stability

As shown in Figure 2.2A, the measured impedance for representative electrodes paralleled previous observations for metal electrodes in saline solution (Robinson 1968).

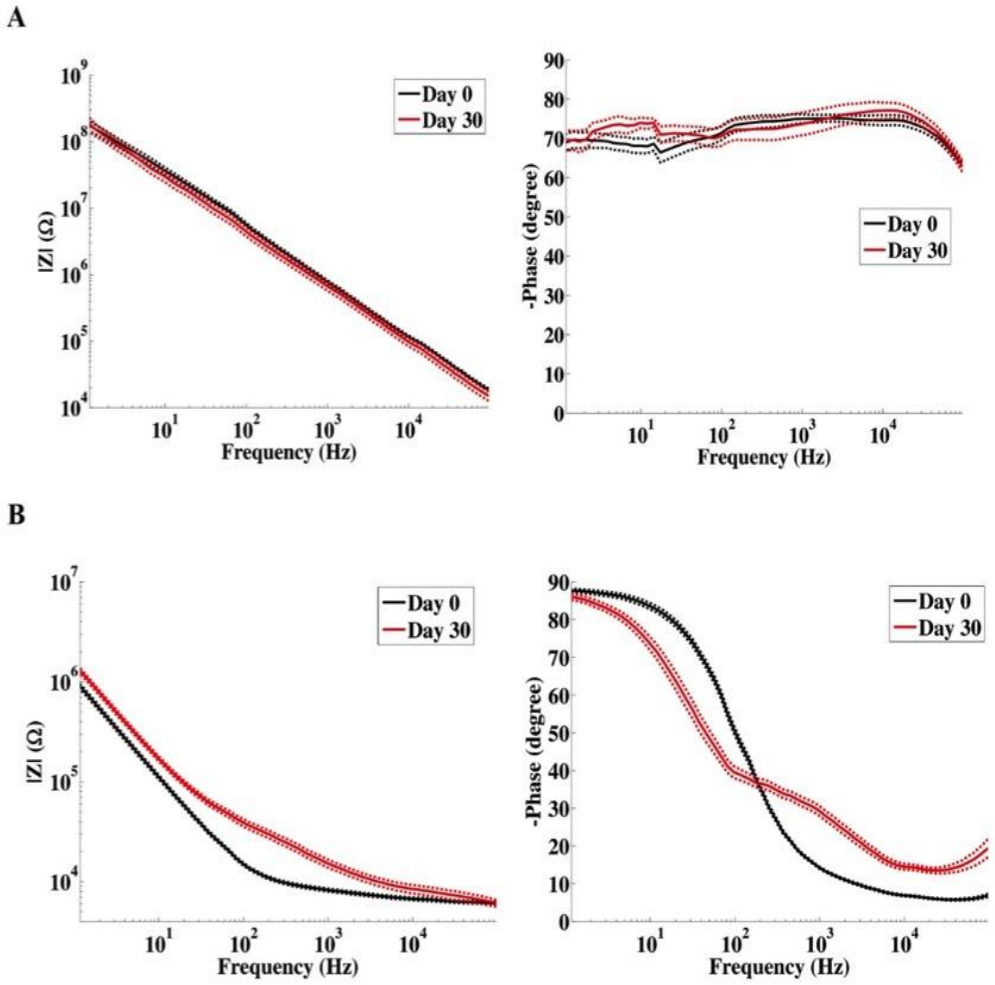

Figure 2.2. Electrochemical impedance stability of the novel MEA. The impedance profile from uncoated gold microelectrodes at day 0 and day 30 with storage at 37° C in PBS (A). The impedance profile from the gold microelectrodes individually coated with PEDOT at day 0 and day 30 with storage at 37° C in PBS (B).

To assess stability of the novel MEA microelectrodes and surrounding insulation, we compared the initial impedance and final impedance after 30 days within a cell incubator at 37 °C. The initial impedance magnitude at 1 kHz was 796.3 ± 49.6 kΩ (mean ± SEM, n=total of 16 microelectrodes from two MEAs, 8 microelectrodes per MEA) while the phase was -74.9 ± 1.1º. After 30 days, neither the impedance magnitude, 686.7 ± 98.9 kΩ, nor the phase, -73.6 ± 2.8º, were significantly altered, suggesting that the novel MEA maintains electrochemical stability for at least 30 days *in vitro*.

To further assess MEA robustness and tolerance for handling, we examined the stability of impedance characteristics after electropolymerization of microelectrode sites with the conducting polymer poly(3,4-ethylenedioxythiophene) (PEDOT) as described for *in vivo* microelectrodes (Mandal et al. 2014). PEDOT deposited with the counterion tetrafluoroborate has been shown to produce a robust, durable, and stable electrochemical interface for microelectrodes (Mandal et al. 2014; Mandal et al. 2015). As shown in Figure 2.2B, coating with PEDOT resulted in a significant alteration in the impedance profile where the initial impedance magnitude and phase at 1 KHz were 6.1 ± 0.4 kΩ and -13.6 ± 0.4º, respectively. The significant decrease in impedance is due to increased electrode surface area as a result of the rough polymer surface, which is consistent with other observations of PEDOT-coated metal electrodes (Green et al. 2012; Green et al. 2010). After 30 days, the impedance magnitude, 15.3 ± 1.4 kΩ, and the phase, -29.5 ± 1.3º remained significantly lower than uncoated gold electrodes. However, Figure 2.2B suggests that the PEDOT-coated electrodes are not as stable over time compared to uncoated electrodes. This may be due to poor adhesion of the PEDOT coating. Hydrolysis of

water at the electrode surface results in bubbles, which has been observed to diminish the adhesion of PEDOT during deposition (Green et al. 2010).

2.3.2 Neuronal Culture

Following surface preparation, the novel MEA supported cell body adhesion and neuronal growth, as shown in Figure 2.3A.

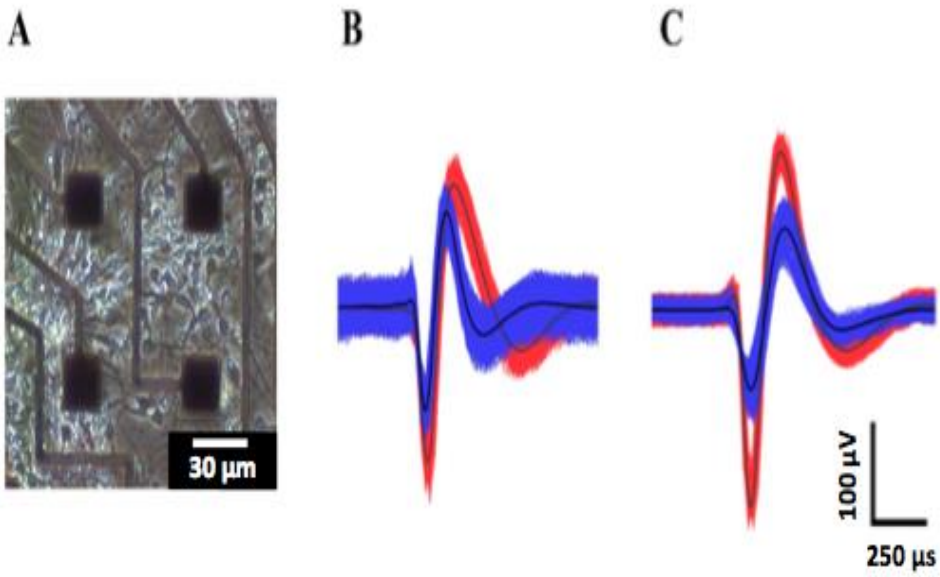

Figure 2.3. Cultured neuronal network on a UT Dallas MEA substrate (A). Representative activity from a single microelectrode recording site from a UT Dallas MEA showing two distinct units (B). Similar activity from a sister neuronal network culture on a MCS MEA (C).

With the maturation of the network, extracellular action potentials could be readily observed across multiple microelectrode recording sites (Figure 2.3B); these biphasic waveforms were entirely consistent with extracellular recordings reported previously using conventional MEA platforms (Chiappalone et al. 2003; Nam and Wheeler 2011). Parallel experiments using MCS MEAs showed virtually identical extracellular potentials (Figure 2.3C).

2.3.3 Comparative Native Neuronal Activity Across MEA Platforms

To examine the suitability of the UT Dallas MEA, we compared the resulting neuronal activity with that derived from the commercially available MCS MEA. As shown in Figure 2.4, cortical neuronal networks on each of the MEA platforms after approximately 3 weeks in culture displayed coordinated bursting activity.

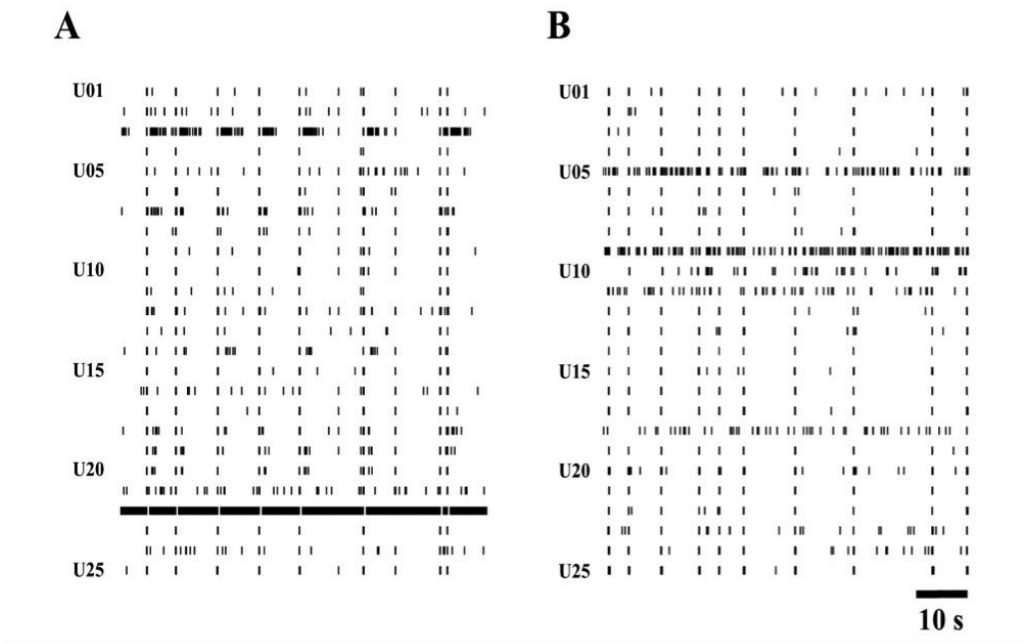

Figure 2.4. Raster plots of extracellular activity from cortical neuronal networks cultured for at least 21 days *in vitro* on a representative UT Dallas MEA (A), and a typical MCS MEA (B).

This observation for both MEA types is entirely consistent with prior work(Gross, Wen, Lin 1985; Jimbo et al. 2000; Novellino et al. 2011; Xiang et al. 2007). Multiple experiments were performed to quantitatively and systematically compare the MEA platforms. Electrophysiological parameters such as network mean spiking rate, mean bursting rate, and

mean inter-spike interval showed that the activity across the UT Dallas MEAs was statistically indistinguishable from that produced on the MCS MEAs (Table 2.1).

Table 2.1. Comparison of neuronal network parameters from sister cortical cultures seeded on novel MEAs and MCS MEAs. None of the parameters were statistically different between the MEA platforms.

	Network Number	Spike rate (Hz)	Burst rate (min^{-1})	Interspike interval (s)	Yield (%)
UT Dallas MEAs	11	2.8±0.3	4.8±1.0	1.8±0.1	67±6
MCS MEAs	9	2.5±0.5	4.3±0.8	1.7±0.2	74±11

In addition, the activity yield, i.e., the percentage of microelectrode sites that demonstrated resolvable single unit activity, was not different between the MEA types (~70%).

2.3.4 Comparative Neuronal Activity with Pharmacological Compounds Across MEA Platforms

To further probe the consistency of the MEA platforms, we also quantitatively characterized the effects of pharmacological agents on cultured cortical networks. Excitatory reagents, pilocarpine and bicuculline, an inhibitory reagent, memantine, and a neutral biomolecule, $A\beta_{1-42}$ monomer (Charkhkar et al. 2015), were applied to networks cultured on both substrate types. Exposure to pilocarpine and bicuculline resulted in an elevation in mean bursting and spiking rate, as shown in Figures 2.5 and 2.6, whereas memantine produced a reduction in mean spiking rate and the $A\beta_{1-42}$ monomer failed to markedly alter spike activity.

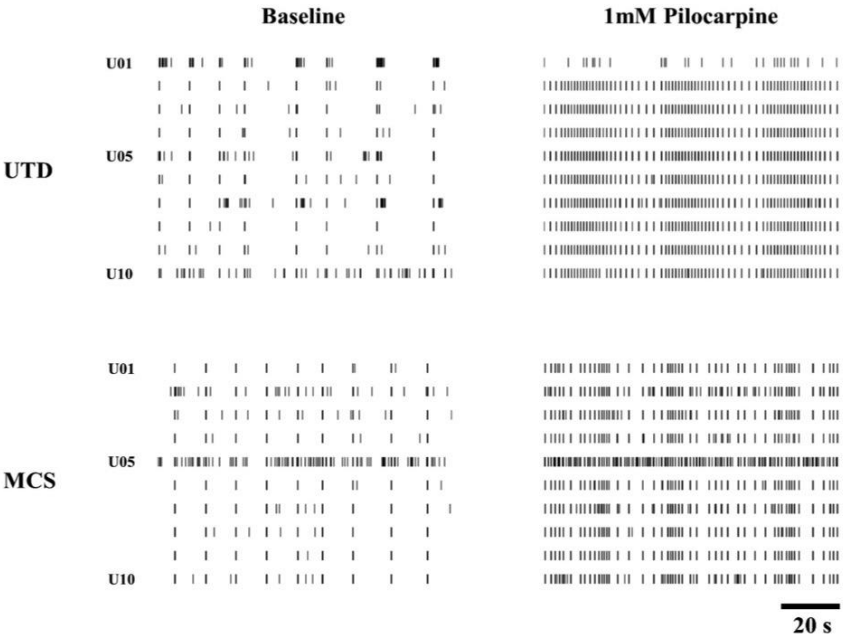

Figure 2.5. Raster plots of extracellular activity from cortical neuronal networks exposed to 1 mM pilocarpine on UT Dallas (A) and MCS (B) MEAs. Neuronal networks on both substrates responded similarly to the reagent.

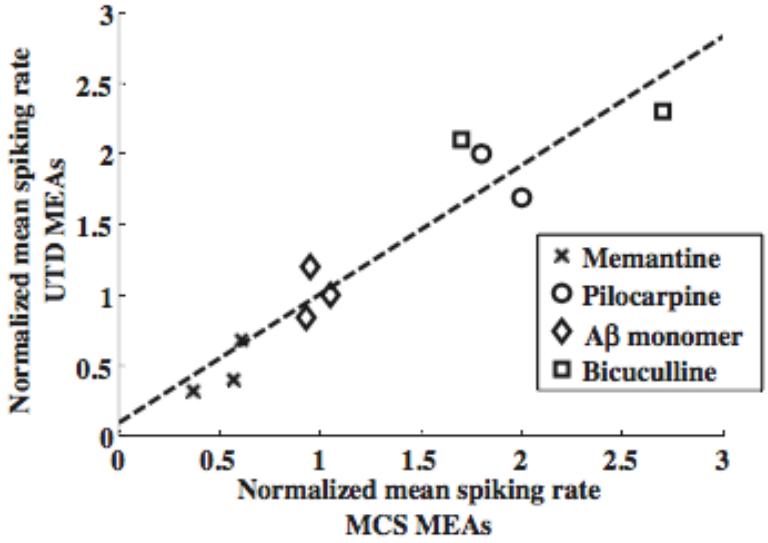

Figure 2.6. Normalized spiking rates for neuronal networks on UT Dallas vs. MCS MEAs in response to 1mM pilocarpine (o), 5 µM bicuculline (□), 5 µM $A\beta_{1-42}$ monomer (◊), and 20 µM memantine (x). The dashed line is the linear regression to the plotted data. The responses to the tested compounds were identical in both MEA types.

Figure 2.6 summarizes the normalized changes in mean spiking rate in response to these compounds for the networks cultured on both MEAs. Linear regression fitting yielded a slope ± standard error of 0.91 ± 0.11, which is statistically indistinguishable from unity. Therefore, the degrees of activity modulation produced by all the reagents were virtually identical for both of the MEA types.

2.3.5 Advantages of the UTD MEA

The use of MEAs for *in vitro* applications has been well-established since the initial demonstration over 30 years ago (Gross 1979; Gross et al. 1985; Gross et al. 1977). With more widespread use through commercial availability, a limitation has emerged with respect to the expense largely attributable to the materials, processes, and cleanroom facilities necessary for reproducible MEA fabrication. Unlike virtually all cell culture dishes and chambers, many of the available MEAs are expected to be re-used where specialized and experienced handling is required. In contrast, by leveraging flexible display fabrication approaches, the process for fabricating UT Dallas MEAs relies on materials common to biomedical applications, such as polycarbonate and parylene C, and can be readily scaled in a cost efficient manner. Based on flexible display fabrication costs, we estimate production costs at nominal volumes to be approximately \$3 per cm^2 such that the novel MEA could be fabricated for as little as \$25.

2.4 Conclusions

We have demonstrated a new design for an inexpensive plastic MEA, which is readily manufactured and disposable. Comparative analyses of electrophysiological parameters from cortical neuronal network activity from this novel MEA showed virtually identical results with a

corresponding commercially available MEA of similar dimensions. We also showed, for the first time, that the primary neuronal cultures on the new disposable MEAs, when compared to networks on these commercially available MEAs, respond similarly to representative excitatory, inhibitory and neutral compounds. Although there have been prior reports on developing novel microelectrode technology, demonstrating the pharmacological consistency is often absent (Heer et al. 2006; Hogan et al. 2012). Such a finding is not trivial considering that the substrate material could greatly impact the growth and development of primary neuronal cultures (Bayliss et al. 1999; Flanagan et al. 2002). The functional comparison shown in the present study demonstrates that these new disposable MEAs are entirely suitable for *in vitro* assay applications.

2.5 Acknowledgements

The authors acknowledge support from NSF PFI grant number IIP-1114211 (PI: BE Gnade) and from the DARPA Young Faculty Award Program (PI: WE Voit). The authors would also like to thank Wallace Martin, Jim Burris and Gordon Pollack of the University of Texas at Dallas clean room for many helpful processing suggestions.

CHAPTER 3

ORGANIC LIGHT-EMITTING DIODES FOR *IN VITRO* OPTICAL STIMULATION

Organic light-emitting diode (OLED) technology has revolutionized lighting and display technology since the first practical device was fabricated in the late 1980's (Geffroy et al. 2006). OLEDs have been used as solid-state light sources, providing an inexpensive and energy-efficient alternative to incandescent and fluorescent light bulbs (D'Andrade and Forrest 2004). OLED technology has also been explored for large-area, flexible display applications (Urabe et al. 2007). In this work, OLED devices are fabricated and characterized for potential application in *in vitro* optical stimulation of cells in optogenetic experiments on MEA substrates. In previous optogenetic work, optical stimulation was delivered via objective lenses, lasers, and fiber optic cables (Matsunaga et al. 2013; Renault et al. 2015; Welkenhuysen et al. 2016). With these light delivery methods, it is difficult to deliver optical stimulation in a precise location relative to an MEA electrode, in a manner that is consistent from substrate to substrate. In this work, we demonstrate the fabrication of OLEDs that emit wavelengths of light that are relevant to optogenetic experiments. We show that device encapsulation methods extend device lifetimes to timescales that are relevant to OLED operation in *in vitro* optogenetic experiments.

3.1 Introduction

Work prior to the development of the OLED had demonstrated electroluminescence in organic crystalline materials. In the earliest publication, metal contacts were deposited on a 20 μm thick anthracene crystalline slab, but the 400 V required for light emission from the device and the low efficiency made practical application impossible (Helfrich and Schneider 1965; Pope

et al. 1963). However, concepts established in the publication of the first practical OLED drive the fabrication of high-luminance devices today. These concepts include: choice of electron and hole injection material and workfunction of anode and cathode material, fabrication of low-voltage devices by evaporating device material films, recombination enhancement by use of layered structures of different materials, and high electric field by ultra-thin film formation (Hung and Chen 2002).

The next iteration of organic electroluminescent devices were fabricated by thermally evaporating thin, sub-micron films of anthracene on to the cathodes; top electrodes were also thermally deposited, without breaking vacuum. These devices were driven at 30 V with external quantum efficiencies of 0.03-0.06% (Vincett et al. 1982). A later device fabricated by Tang and VanSlyke, the first practical OLED, utilized thermal vacuum deposition of thin films, as well as a layered device structure to obtain 1% external quantum efficiency at driving voltages below 10 V (Tang and VanSlyke 1987). The layered structure consists of a 750 Å film of diammine, a hole transporting material, and a 600 Å film of tris(8-hydroxy-quinolinato)aluminum (Alq3), a metal chelate emissive layer. A green OLED based on a similar heterostructure device architecture with an Alq3 emissive layer is presented in this chapter.

The increase of efficiency due to hole transport layers (HTL) and electron transport layers (ETL) should be discussed here, as it is relevant to the next generation of OLEDs that utilize complex, multilayered device architecture in order to achieve efficiencies beyond 1%. A band diagram of a single layer device is presented in Figure 3.1A.

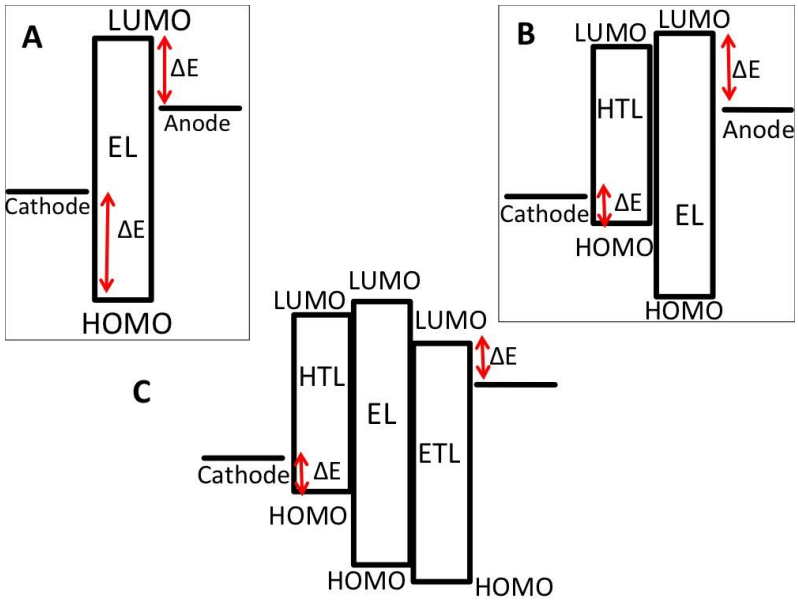

Figure 3.1. Band diagrams of OLED devices, including (A) a simple device, (B) a heterostructure device utilizing an HTL, and (C) a double heterostructure device utilizing an HTL and an ETL.

Single layer devices are inefficient at exciton generation due to two crucial reasons. One reason is that there may be poor charge injection at the interface of the emissive layer (EL) and the anode and/or the interface of the EL and the cathode. This is due to the fact that it is practically impossible to simultaneously match the work function of the anode to the HOMO of the EL and match the work function of the cathode to the LUMO of the EL. This creates an energy barrier at one or both electrodes that impedes charge injection into the EL (Kulkarni et al. 2004). Another reason is the fact that electron and hole mobilities in organic semiconductor materials differ greatly. For example at an electric field of 6.3×10^{5} Vcm^{-1}, electron mobility in Alq3 was determined to be 1×10^{-5} $cm^{2}V^{-1}s^{-1}$, while the hole mobility was found to be 3 orders of magnitude smaller (Naka et al. 2000). An HTL may be added, as shown in Figure 3.1B. The HTL material should be carefully chosen. The material should have a low reduction potential that facilitates a relatively high hole mobility and the HOMO of the HTL should reduce the

energy barrier for hole injection from the anode (Tang and VanSlyke 1987). The overall result of an effective HTL is exciton generation in the EL, which results in radiative emission, rather than hole-electron recombination at the anode-EL interface, which does not result in radiative emission. Similarly, an ETL may also be employed, as shown in Figure 3.1C. An appropriate ETL has a high reduction potential, resulting in high electron mobility, and a LUMO that reduces the energy barrier for charge injection from the cathode (Kulkarni et al. 2004). The use of both the ETL and HTL reduces non-radiiative recombination at the interface of either the cathode or the anode, and increases the efficiency of generation in the EL.

Beyond these early single and double layer device architectures, contemporary work has focused on increasing the efficiency of the devices, through a variety of strategies. The next generation of devices utilized a double heterostructure architecture that consisted of an HTL, an emissive layer, and an ETL (Chihaya et al. 1988). This device also uses a doped emissive layer strategy. The EL is doped with a small concentration of a fluorescent molecule. The host and dopant materials are chosen such that the singlet S_1 energy level of the host is higher than the S_1 singlet energy level of the dopant, so that energy is transferred from the host to the dopant, as shown in Figure 3.2A. In this manner, the dopant acts as an exciton trap. The concentration of the dopant in the host layer is optimized to prevent self-quenching, a process in which a high concentration of dopant absorbs energy of the exciton and emits the energy in a non-radiative manner. Trapping excitons in the emissive layer and reduction of self-quenching results in an increase of the luminescent efficiency of the emissive layer. The result of the combination of the double heterostructure and fluorescent dopant strategies is a device with approximately 5% external quantum efficiency (Tang and VanSlyke 1989).

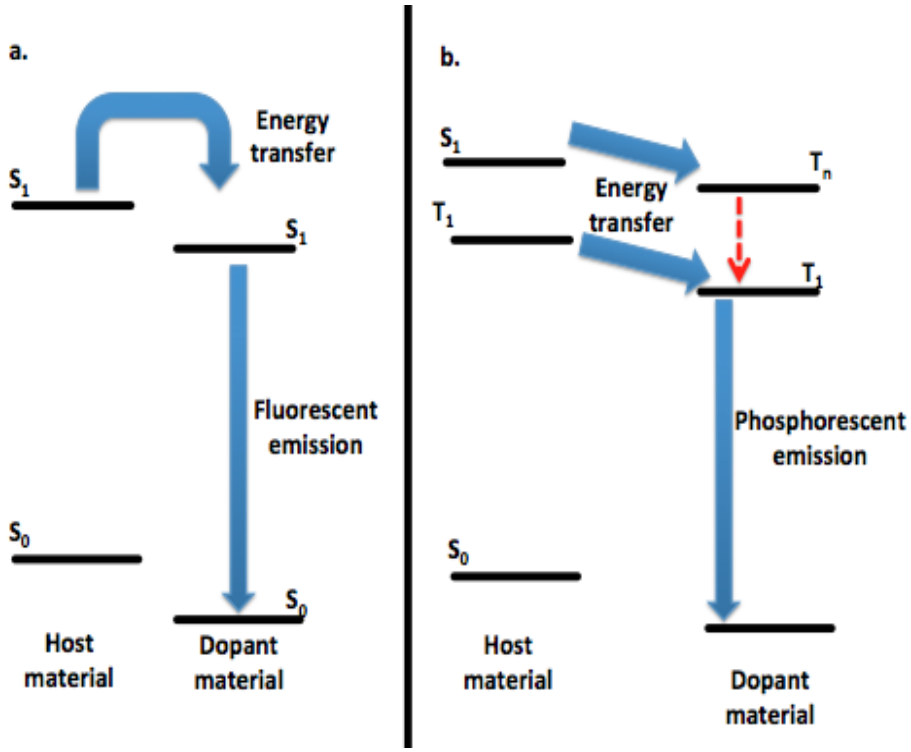

Figure 3.2. Mechanisms of doped host energy transfer mechanisms, in (A) fluorescent, and (B) phosphorescent mechanisms. Adapted from work by Tang and VanSlyke (1989).

Another strategy for increasing efficiency is to dope an emissive host layer with a phosphorescent dopant (Baldo et al. 1998). Again, the host and dopant materials are chosen based upon band gaps, such that energy is transferred from the host to the dopant. However, in the case of phosphorescence, the route of energy transfer is from the S_1 singlet and T_1 triplet states of the host to a triplet excited state T_n of the dopant; after intersystem conversion from the dopant T_n triplet state to the dopant T_1 state, light is emitted via phosphorescence, as shown in Figure 3.1B. These types of dopants are small molecule metal chelates with a heavy central metal atom, such as iridium or platinum, that increases the rate of intersystem crossing from a singlet host state to a dopant triplet state, as previously discussed in Chapter 1, Section 1.3.1. The singlet excited states that induce fluorescent emission only represent 25% of the total excited

state population. Phosphorescent dopants allow access to triplet excited states, and hence, a greater fraction of the total excited state population, which increases the theoretical efficiency of such devices (Forrest et al. 1998). However, the lifetimes and diffusion lengths of singlet and triplet excitons differ greatly. Fluorescent emission is spin-allowed and occurs rapidly, so singlet excitons may diffuse short distances of ten to a few hundred angstroms. As previously discussed, phosphorescence occurs by mediating mechanisms, which result in longer exciton lifetimes. A triplet exciton may diffuse for much longer distances, up to a few thousand angstroms (O'Brien et al. 1999). Phosphorescent heterostructure devices must be carefully designed with the band gaps of the hole transport layer, electron transport layer, phosphorescent dopant, and emissive host layer in mind in order to trap both singlet and triplet excitons in emissive layers. High external quantum efficiencies from 23% up to 30% have been reported from phosphorescent OLEDS utilizing a heterostructure architecture (Adamovich et al. 2003; Forrest et al. 1998; Udagawa et al. 2016).

The fabrication of two OLED devices is reported in this chapter. One device is a green OLED that features a heterostructure device architecture and Alq3 as an emissive material, similar to work by Tang and VanSlyke (Tang and VanSlyke 1987). However, in this particular device, the triarylamine HTL that was utilized by Tang and VanSlyke has been replaced with N,N’-Bis(naphthalene-1-yl)-N,N’-bis(phenyl)-benzidine (NPB). This material is more favorable as an HTL than the previously used triarylamine material since NPB film has been found to increase lifetime and stability of Alq3 devices (Aziz et al. 1998; Gautier et al. 1996; McElvain et al. 1996). A cross-sectional schematic of the device, and material structures is presented in Figure 3.3, and an energy level diagram for the device materials is show in Figure 3.4.

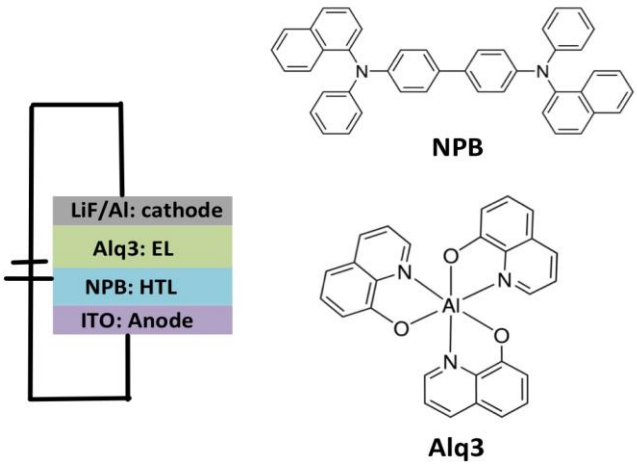

Figure 3.3. An illustration of the green OLED device, including chemical structures for the hole transport layer (HTL) and electroluminescent layer (EL). Device structure is adapted from work by Tang and VanSlyke (1987), and chemical structures are reprinted from work by Halls et al. (2001) and Tang and VanSlyke (1987).

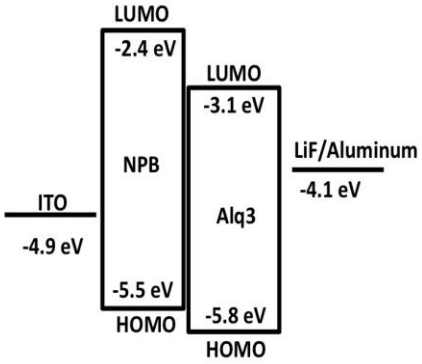

Figure 3.4. Energy level diagram of the green OLED device materials. Adapted from work by Aziz et al. (1998) and Tang and VanSlyke (1987).

The phosphorescent blue OLED fabricated in this work is based on an electroluminescent layer reported by Kawamura et al. in 2005. The electroluminescent layer consists of an organic semiconductor host material, *m*-bis(N-carbazolyl)benzene (referred to as MCP), and a

phosphorescent iridium complex, bis[(4,6-difluorophenyl)pyridinato-N,C^2](picolinato)iridium(III) (referred to as FIrpic). FIrpic is a known blue phosphorescent emitter. MCP was utilized as the host material because the energy of the T_1 triplet state of this host material is slightly higher than the T_1 triplet state of the dopant, resulting in 100% transfer of energy from host to dopant. Other host materials have been explored, such as 4,4'-bis(N-carbazolyl)-2,2'-biphenyl (CBP), however, the T_1 energy level of this host material is slightly below the T_1 energy level of the dopant, which results in back-transfer of energy from the dopant to host and decreased device efficiency, which is illustrated in Figure 3.5.

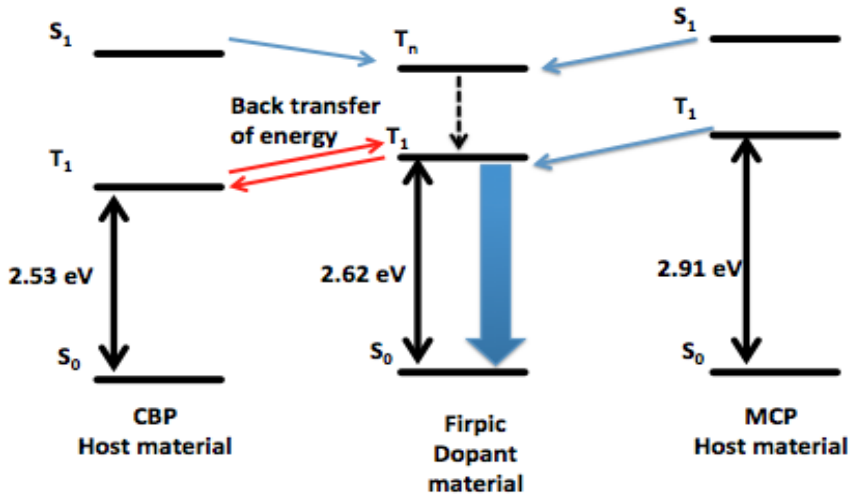

Figure 3.5. Preferred mechanism of energy transfer from MCP host to FIrpic dopant, and mechanism of energy back transfer from FIrpic to CBP host material. Adapted from work by Kawamura et al. (2005).

High internal efficiency with this emissive layer (>99%) is achieved with dopant concentrations ranging from 1% to 10%. The device fabricated for this work also utilizes hole and electron transport layers. A schematic of this device is shown in Figure 3.6 and the energy level diagram of the semiconductor materials is shown in Figure 3.7.

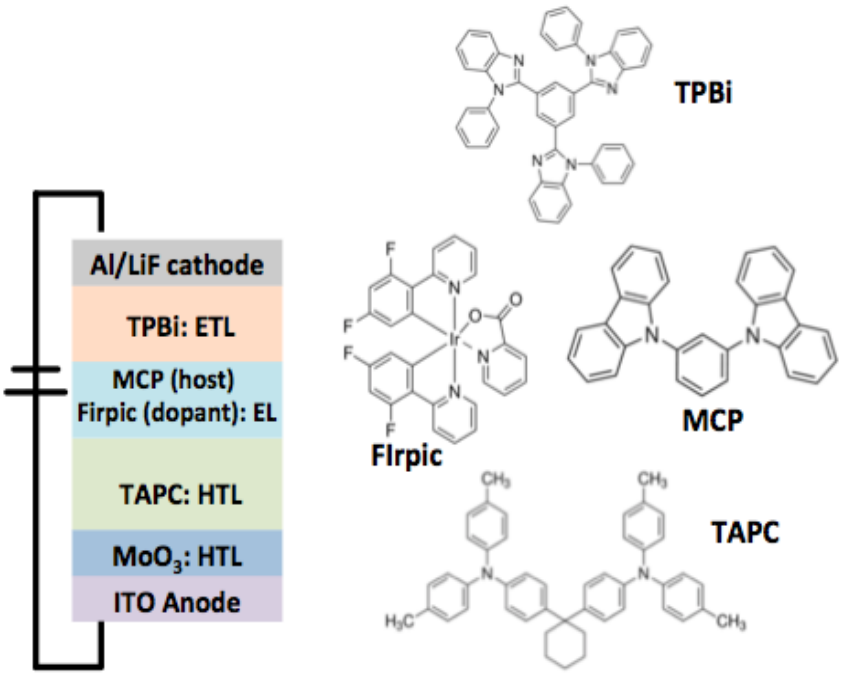

Figure 3.6. An illustration of the blue OLED device, including chemical structures for the electron transport layer (ETL), electroluminescent layer (EL), and hole transport layer (HTL) organic materials. Device and chemical structures adapted from work by Kawamura et al. (2005).

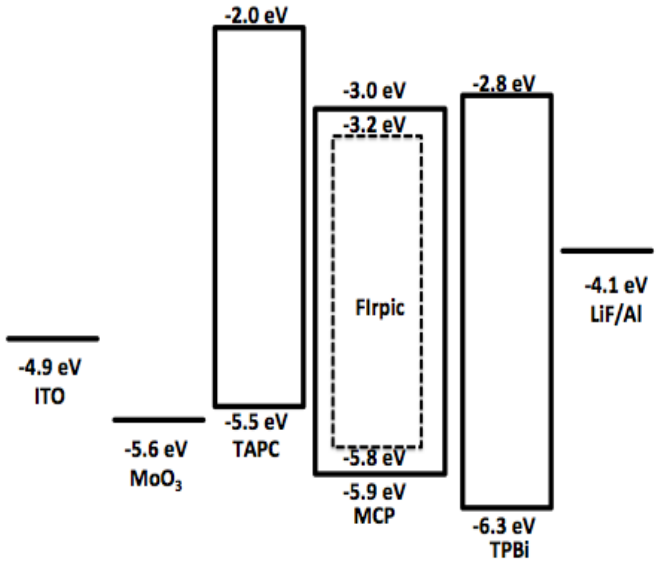

Figure 3.7. Energy level diagram of blue OLED device materials. Adapted from Kawamura et al. (2005).

3.2 Materials and Methods

Fabrication of 10 mm^2 OLED test pixels began with commercially available ITO-coated glass slides (Luminescence Technology Corp., Taiwan). The ITO film has a sheet resistance of 15 Ω/□, and is pre-patterned into 4 10 mm^2 electrodes. The slides were cleaned with sonication in acetone, isopropyl alcohol, and deionized water, for 5 minutes each, dried with N_2, and baked at 100° C for 5 minutes to dehydrate the slide. Just prior to deposition of the OLED stack, the ITO surface was treated with O_2 plasma for 5 minutes.

The glass slides were loaded into the UT Dallas deposition chamber (Cooke Vacuum Products) for thermal deposition of the OLED stack. The custom-designed system features a deposition chamber that is housed in an N_2-purged glove box. The chamber is equipped with 8 radially arranged Knudsen cells. Each cell holds powdered deposition material in a ceramic crucible, and has an individual power controller, temperature monitor, and source shutter to prevent cross-contamination. Additionally, the chamber also has an external power source (Varian), for sublimation of aluminum from a tungsten filament. The slides were loaded onto a rotating substrate holder that is also shuttered. The chamber was pumped down to a base vacuum pressure of $2x10^{-6}$ Torr.

Upon reaching base vacuum, the stack materials for the green OLED were deposited. The following organic materials were used as received from Luminescence Technology Corporation (Taiwan): N-N'-di(1-naphthyl)-N,N'-diphenyl-(1,1'-biphenyl)-4,4'-diamine (>99.5%, NPB), and tris(8-hydroxy-quinolinato)aluminum (>99.5%, Alq3)

Alternatively, a different stack of materials for the phosphorescent blue OLED were deposited. The following organic materials were also used as received from Luminescence

Technology Corporation: 4,4′-Cyclohexylidenebis[*N*,*N*-bis(4-methylphenyl)benzenamine] (>99.5%, TAPC), 1,3-Di(9*H*-carbazol-9-yl)benzene (>99.5%, mCP), Bis[2-(4,6-difluorophenyl)pyridinato-C^2,*N*](picolinato)iridium(III) (> 99%, FIrpic), and 2,2′,2"-(1,3,5-Benzinetriyl)-tris(1-phenyl-1-*H*-benzimidazole) (>99%, TPBi). Molybdenum (VI) oxide (99.99%, anhydrous) was used as received from Sigma Aldrich.

For both types of OLEDs, a LiF/aluminum cathode was deposited by sublimation. Lithium fluoride (99.99%, anhydrous) was used as received from Sigma Aldrich, and was thermally evaporated. Aluminum wire with 1 mm diameter was obtained from Kurt J. Lesker Company (Clairton, Pennsylvania). Six-coil tungsten filaments for sublimation of aluminum from the external power source were obtained from R.D. Mathis Company (Signal Hill, California). The aluminum wire was cut into small pieces, folded into a V-shape, and hung on the coils of the filament for aluminum sublimation. Refer to Appendices B and C for complete details on deposition of stack materials for green and blue OLEDs, respectively.

Once device fabrication was completed, the glass slide was removed from the deposition chamber and transferred to an N_2-purged glove box. In this inert environment, the active area of the device was encapsulated with a glass microscope coverslip and UV-curable epoxy (Addison Clear Wave, St. Charles, Illinois). The coverslip leaves the device contacts exposed. The epoxy was cured in the glove box with a UV lamp for 20 minutes.

The completed encapsulated devices were tested using a Keithly 236 source meter and a PR-650 SpectraScan spectrophotometer. Data acquisition from both instruments was achieved using a custom LabView program.

3.3 Results and Discussion

An image of a completed green OLED pixel, operated at 6 V, is shown in Figure 3.8A. The device turns on at a voltage of 3.5 V. The electroluminescent spectrum of the device operated at 6 V was measured, as shown in Figure 3.8B in order to determine the applicability of this device in optically stimulating the bacteriorhodopsin protein in an *in vitro* optogenetic experiment.

While the device in the image appears blue, due to lighting conditions when the image was taken, the peak output wavelength of this device is at 530 nm, as shown in Figure 3.8B. This wavelength is green light that is appropriate for stimulating the bacteriorhodopsin protein, which has an absorbance spectrum of 500- 650 nm (Lozier et al. 1975).

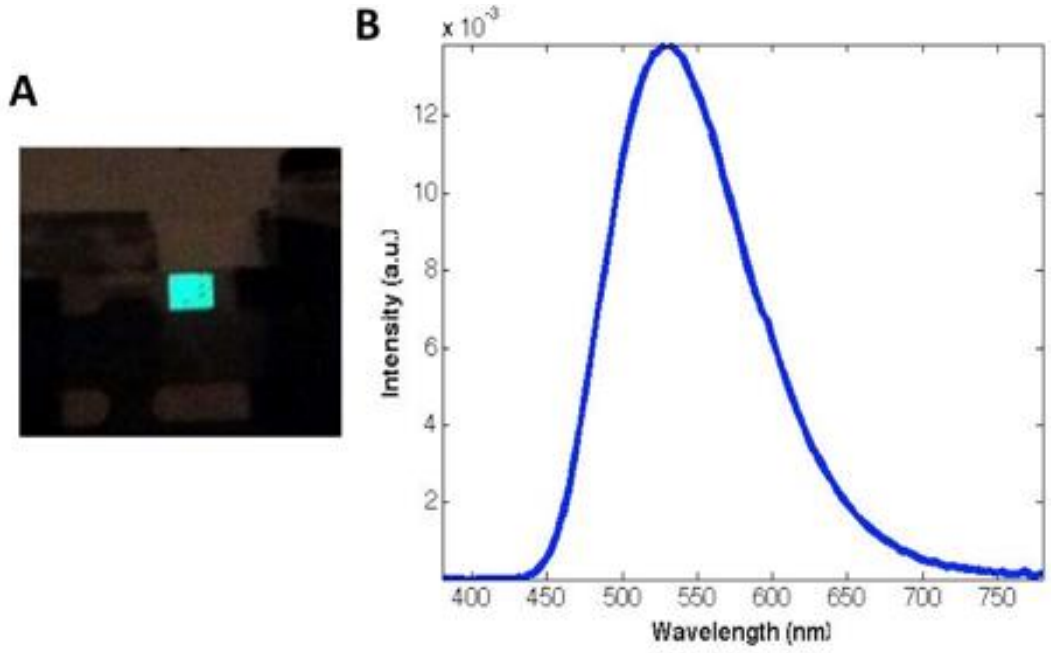

Figure 3.8. Green OLED device operated at 6 V, including an (A) image of the completed operational device and (B) the spectral output of the device.

The plotted current-luminescent characteristics of the OLED are presented in Figure 3.9. To collect this information, the device was driven from 0 to 10 V, while the driving current and optical emission were measured. A current of 1.1 mA is required to drive the 10 mm^2 device to a threshold luminance of 100 cd/m^2.

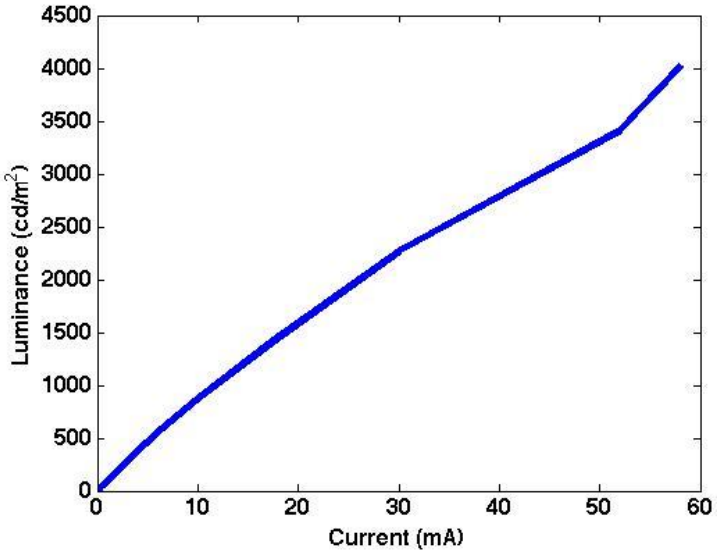

Figure 3.9. Current-luminance characteristics collected from the green OLED at driving voltages from 0 to 10 V.

This indicates that for the pixels on the proposed integrated substrate, which have an area of $10x10^3$ μm^2, 1.1 μA of current is required, assuming that current requirements scale linearly with device dimensions. A TFT integrated with this device on the integrated substrate must be able to supply 1.1 μA of drain current in order to turn on the OLED.

An image of a completed blue OLED pixel, operated at 6 V is shown in Figure 3.10A. The device turns on at a voltage of 4 V. The electroluminescent spectrum of the device was measured at 6 V in order to determine the applicability of this particular device in optically

stimulating the ChR2 protein. The electroluminescent spectrum of the device operated at 6 V is shown in Figure 3.10B.

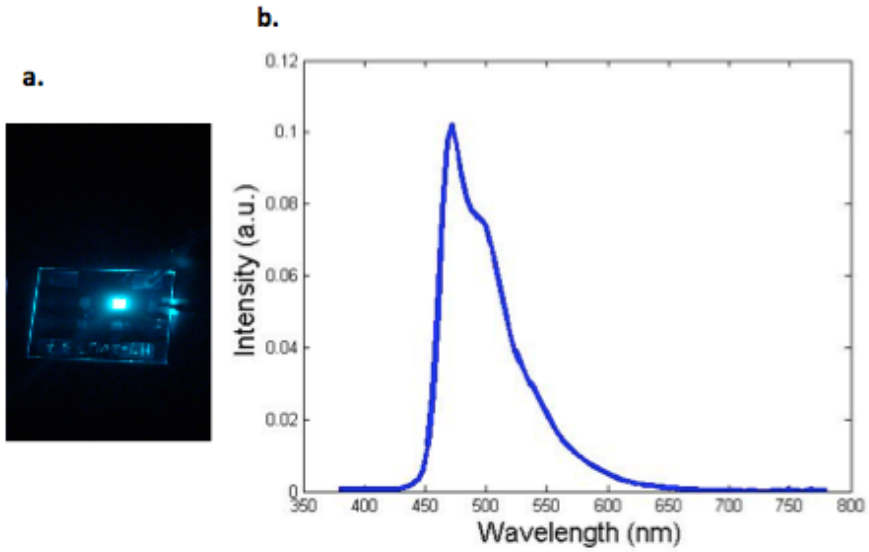

Figure 3.10. Blue OLED devices operated at 6 V, including an (A) image of the completed operational device, and (B) the spectral output of the device.

From this plot, the peak output wavelength is at 480 nm, which indicates that this blue light-emitting device can be used to optically stimulate the ChR2 protein. Current-luminance characteristics were also collected from the device, and are presented in Figure 3.11. To collect this information, the device was driven from 0 to 12V, while the driving current and optical emission were measured.

From this plot, the required drive current for the device is determined. For the 10 mm^2 test pixel, the device is assumed to be "on" at a luminance of 100 cd/m^2. This threshold luminance occurs at a driving current of 0.4 mA. The proposed integrated multifunctional substrate consists of OLED pixels that are $10x10^3$ μm^2.

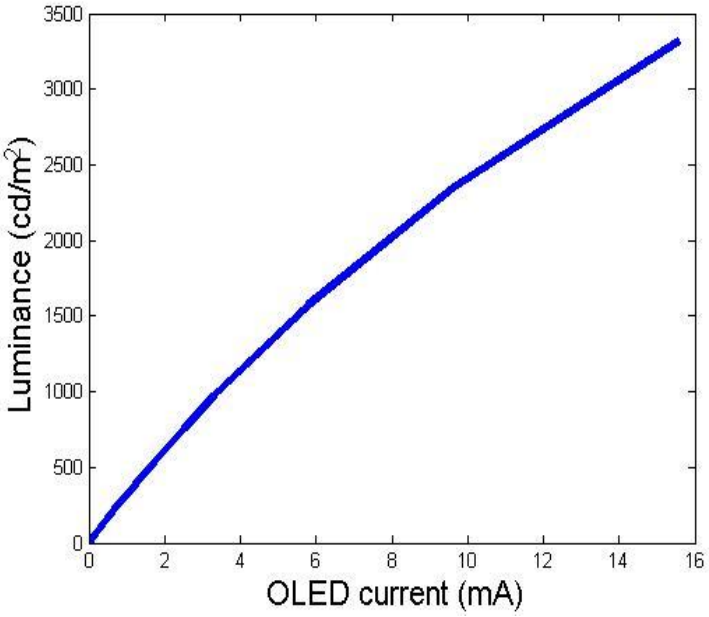

Figure 3.11. Current-luminance characteristics collected from the blue OLED at driving voltages from 0 to 12 V.

Assuming linear scaling between the current-luminance characteristics and device area, the OLED pixels on the integrated substrate, which are three orders of magnitude smaller than the test pixels, will be turned on with a driving current of 0.4 μA. A TFT interfaced with the OLED on the integrated substrate must be able to supply a minimum of 0.4 μA drain current in order to drive the blue device.

A lifetime test was conducted to determine the lifetime of the blue OLED pixel under constant operation. The device was operated at 6 V, and spectral and electrical data were collected periodically by driving the device from 4-16 V, which is shown in Figure 3.12. From Figure 3.12B, it can be seen that while the intensity of the output radiation does decrease over the course of continuous operation, the peak wavelength remains 470 nm. During continuous use, the OLED continues to emit a wavelength of light that would stimulate the ChR2 protein.

However, as seen in Figure 3.12A, the luminance of the device does decrease over time with constant use. In fact, the initial luminance of the device decreases by approximately half over the course of the first hour of the experiment.

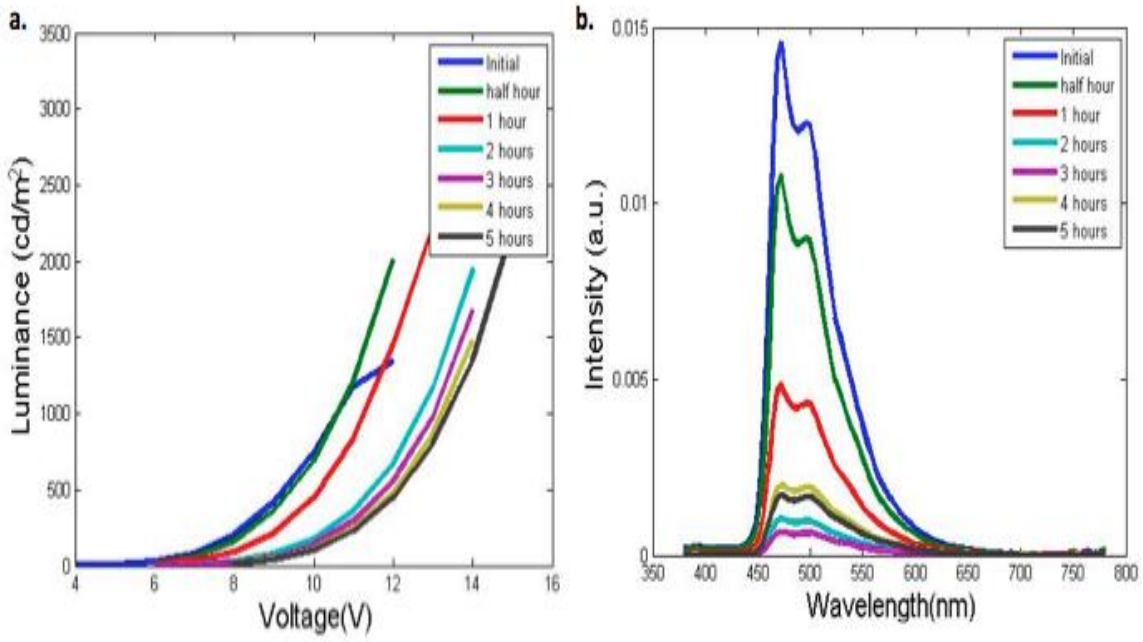

Figure 3.12. Results of OLED lifetime test under continuous operation, including (A) the voltage-luminance characteristics, and (B) the spectral output of the device.

This short time operating time may present a concern to a potential user of this technology for *in vitro* optogenetic experiments, since a constant luminance intensity would be required over the duration of an experiment in order to consistently illicit a stimulated response from electrogenic tissues. However, OLED degradation and loss of luminance occur mainly when the device is (Aziz and Popovic 2004). Optical stimulation in optogenetic experiments is delivered in short pulses, ranging from 1 millisecond to few 100's of milliseconds at frequencies of 1-100 Hz (Mohanty and Lakshminarayananan 2015). Therefore, the total time of operation for the OLED during a typical experiment would be on the order of a fraction of a second to a few

minutes. Therefore, it is still possible that this particular OLED device would be suitable for application in *in vitro* optogenetic experiments.

3.4 Conclusions

Fabrication of green- and blue-light emitting OLEDs for application in optogenetic experiments has been demonstrated. The spectral output of the green OLED indicates that the peak output wavelength is 530 nm, which is appropriate for stimulation of the bacteriorhodopsin protein. The 10 mm^2 test pixel is driven to a threshold brightness of 100 cd/m^2 with a driving current of 1.1 mA. For the proposed integrated substrate, which features OLEDs with an area three orders of magnitude smaller than the test pixels, 1.1 μA of current is required.

The spectral output of the blue device indicates that the peak wavelength of light emitted from the device is 470 nm, which is appropriate for stimulating the ChR2 protein. From the current-luminance characteristics of the blue test pixel, 0.4 mA of current is needed to drive the device at a threshold luminance of 100 cd/m^2. This means that 0.4 μA of current would be necessary to drive the OLED pixels on the proposed integrated substrate.

A preliminary lifetime test of an encapsulated blue OLED pixel demonstrates proof of concept that the stability of the encapsulated blue device is sufficient for an *in vitro* optogenetics experiment. The peak wavelength of the device does not shift during continuous operation of the device, but the luminance does decrease by half in the first hour of continuous operation. However, total on-time during a typical optogenetics experiment is on the order of minutes, a relatively short time frame for OLED degradation. We believe that this lifetime test demonstrates proof of concept that this particular blue OLED would be suitable in this application

CHAPTER 4

THIN FILM TRANSISTORS FOR DRIVING OLED OPERATION

In Chapter 3, the fabrication of two different types of OLEDs was presented and the driving current requirements for each device were determined. In this chapter, the fabrication of a thin film transistor, based on an indium-gallium- doped zinc oxide active layer is presented. The current output performance of this device indicates that it is capable of turning on and driving both types of OLEDs presented in chapter 3. While this is sufficient for proof of concept, a lifetime test of the unencapsulated transistor stored on the shelf indicates that there is some instability in device performance, and future work should address this.

4.1 Introduction

The development of transistor technology, including the field effect transistor (FET) spurred the growth of the semiconductor industry, as it is the fundamental component integrated circuit technology (Kasap 2018). The FET, and the related thin film transistor (TFT), acts as a switch, where the magnitude of the output current is modulated by the magnitude of the input gate voltage. This modulation occurs because charge is produced when a transverse electric field is applied normal to the surface of a semiconductor. This induced charge changes the surface conductivity of the semiconductor. In metals, this effect is negligible, due to the high density of conduction electrons that are present even in the absence of an applied field. However, in a semiconductor, this effect is not trivial and the applied voltage may change the conductivity in the surface region by several orders of magnitude. As such, the applied voltage is used to modulate current in the semiconductor.

The first reports of the utilization of a transverse voltage to modulate conductivity were recorded in 1926 (Lilienfield 1926). In 1935, this phenomenon was also observed in thin films by Heil. Shockley and Pearson observed this effect in germanium, and using principles of solid state physics, they were able to demonstrate that surface states of the semiconductor were responsible for modulation of conductivity (Shockley and Pearson 1948). In 1947, the first insulated gate, field-effect device, a precursor to the metal oxide semiconductor field effect transistor (MOSFET) was reported. Electrodes and gate dielectric were evaporated onto a single crystal of cadmium sulfide (Bardeen 1947). Later in 1960, the first true TFT was demonstrated (Bockemuehl 1960). The device was based on a cadmium sulfide semiconductor film, and all materials were deposited as thin films. This work demonstrated that the surface states, and hence the magnitude of output current modulation, were dependent on the nature of the gate dielectric material. The results of this work have inspired studies of surface states in thin film structures. Work on fabricating TFTs has mainly focused on determining suitable combinations of semiconductors and gate dielectric materials for TFTs in novel applications, such as flexible electronics.

In selecting an appropriate semiconductor for transistor fabrication, in general, carrier mobility, a measure of how quickly charge carriers move through the material, is an important characteristic. High carrier mobility means that electrons or holes will be swept from source to drain quickly, and the device will have a rapid response to high frequency applied voltage. However, high carrier mobility materials, such as single crystal silicon, are deposited using costly methods or in high temperature conditions that minimize the adoption of TFTs in particular projects where low-cost, large area fabrication is a goal. Specific to this project, carrier

mobility is less of a priority for the semiconductor material than the methods used to deposit all of the device materials, including the semiconductor and the gate dielectric. Since this TFT will be an integrated device, deposition temperatures should be taken into consideration, relative to the melting points and processing temperatures of other materials utilized in fabricating the MEA and the OLED devices that will also be integrated on the proposed substrate. Since the MEA is encapsulated with parylene-C, a polymer material with a melting point of 290 °C, methods used to deposit the TFT materials must have processing temperatures well below this melting point. For this project, HfO_2, deposited at 100 °C by atomic layer deposition was selected for the gate dielectric. Based on previous work in our group, this is a suitable TFT gate dielectric material (Perez et al. 2012). Indium, gallium-doped zinc oxide (IGZO) was selected as the active layer semiconductor material. This material has been used to fabricate TFTs at low processing temperatures with relatively high field effect mobility (Kang et al. 2011). There are two low temperature methods used at UT Dallas to deposit this material. One method is pulsed laser deposition (PLD), in which a high-powered laser ablates an IGZO target to deposit a film of IGZO on a substrate, under vacuum at room temperature (Suresh et al. 2007). The volume of a typical PLD deposition chamber accommodates substrates smaller than a four inch silicon wafer. The chamber size for this method is not large enough to accommodate our fully integrated substrate. For this reason, RF magnetron sputtering was selected as the deposition method. In the sputtering method, an inductively-coupled plasma is ignited by a radio frequency magnetron source, causing high energy gas ions to bombard an IGZO target (Kumomi et al. 2008). IGZO fragments are ejected from the target and deposited as a film on the substrate. Sputtering was performed at room temperature. The volume of the deposition chamber is large enough to

accommodate the proposed integrated substrate, which enables large area fabrication. Utilization of sputtering over PLD is also advantageous to scaling the manufacture of the integrated substrate in the future, as sputtering is a well-established process in the semiconductor device fabrication industry.

4.2 Materials and Methods

Transistor fabrication began with a glass substrate coated with a blanket film of ITO from Luminescence Technology Corporation (Taiwan). The ITO film has a sheet resistance of 15 Ω/□. The glass substrate was cleaned using sonication in acetone, isopropyl alcohol, and deionized water for 5 minutes each. The substrate was dried with N_2 and baked on a hotplate at 100° C for 5 minutes.

The gate electrode was patterned using the standard S1813 photolithography procedure. The ITO film was etched using undiluted HCl for 1.5 minutes. Next the following blanket films were deposited on the substrate: 30 nm HfO_2, the gate dielectric, via atomic layer deposition; 30 nm IGZO, the active layer, via RF magnetron sputtering (ATC Orion sputter deposition system by AJA International); and, 500 nm parylene-C, the inner layer dielectric, via chemical vapor deposition (deposition system by Specialty Coating Systems). These films were patterned using standard S1813 photolithographic processes. The parylene film was etched with an O_2 plasma etch, IGZO was etched in hydrochloric acid, diluted 1:1000, and HfO_2 was etched in 7:1 buffered oxide etch (BOE). After these films were patterned, a blanket film of 200 nm thick aluminum was deposited by sputter deposition. The aluminum was patterned using standard S1813 photolithography, and etched using undiluted phosphoric acid heated to 80° C. An illustration of this process flow is shown in Figure 4.1. Refer to Appendix C for complete details on the

fabrication process flow. The completed devices were tested on a Cascade Microtech probe station equipped with a Keithly 4200 semiconductor characterization system.

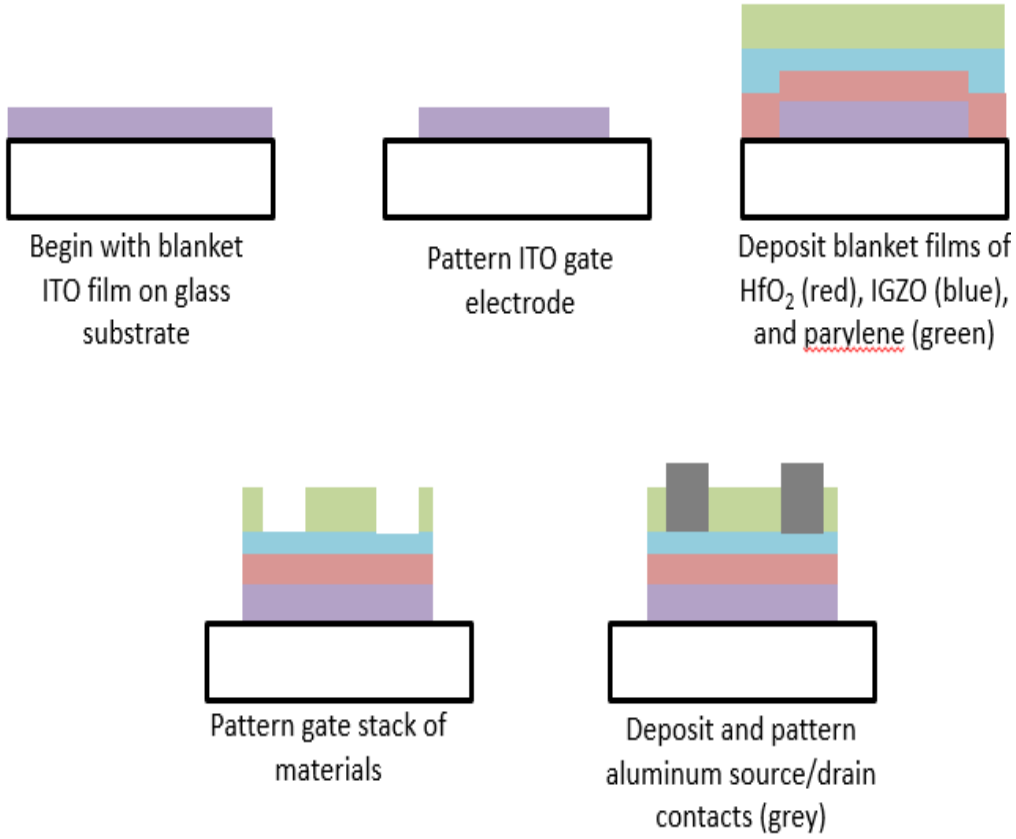

Figure 4.1. Illustration of IGZO TFT fabrication process flow.

4.3 Results and Discussion

An image of a completed TFT is shown in Figure 4.2A. As previously determined in Chapter 3, the green OLED requires a driving current of 1.1 μA, and the blue OLED requires a driving current of 0.4 μA in order to turn on the OLED pixel to a minimum brightness of 100 cd/m^2.

The V_G- I_D characteristics of this device are plotted in Figure 4.2B. This plot demonstrates that the TFT is capable of turning on the both types of OLED to a brightness of 100

cd/m^2. At a drain voltage of 6.0 V, a driving current of 1.1 μA is delivered at an applied gate voltage of 2.0 V , and 0.4 μA of current is delivered at 1.2 V applied gate voltage.

In order to determine the threshold voltage, V_T, and carrier mobility, μ_{sat}, as determined using Equations 1.3 and 1.4, the square root of the drain current is plotted versus the gate voltage, as shown in Figure 4.2D. A linear fit is applied to the linear region of the plot. The slope of the line is equal to μ_{sat} and the x-intercept is equal to V_T. For this particular device, the V_T was calculated to be 2.0 V, and μ_{sat} was calculated to be 2.9 cm^{2}V^{-1}s^{-1}.

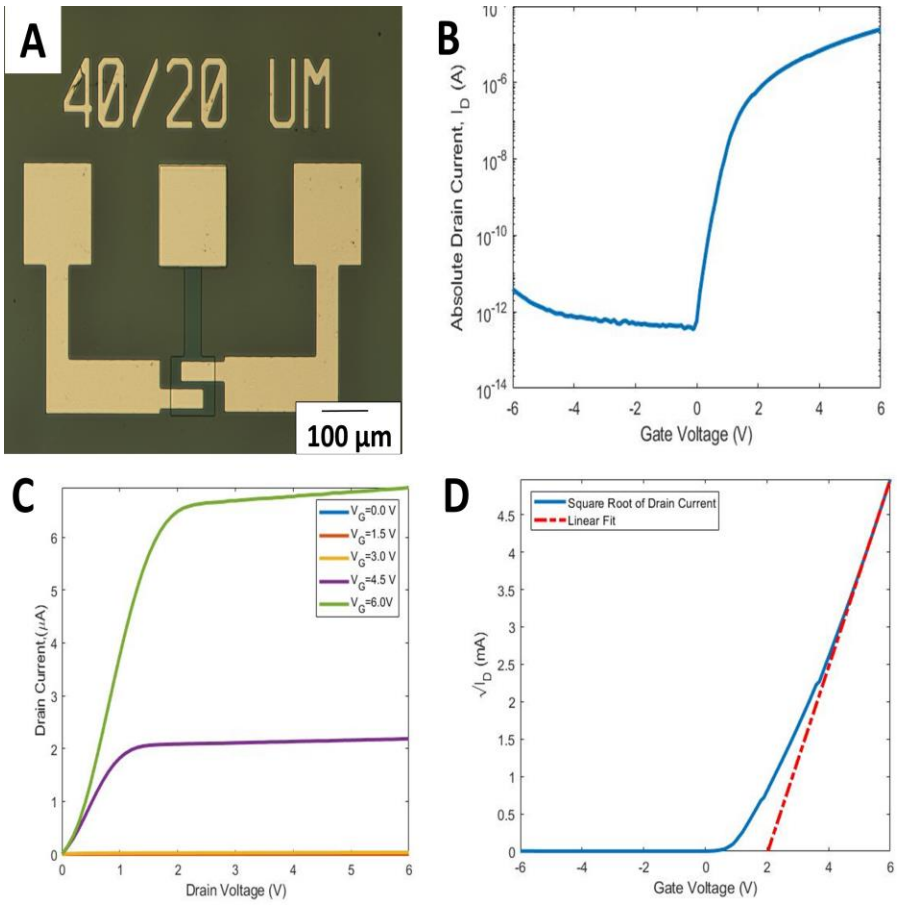

Figure 4.2. Completed TFT, including (A) an image of the device, (B) the V_G-I_D transfer curve operated with a V_{ID} of 6 V, (C) the V_D-I_D output curve, and (D) a plot of $\sqrt{I_D}$ vs V_G.

The mask set used in the fabrication produces an array of transistors of various channel dimensions. Consistency in V_T and μ_{sat} among the devices demonstrates that these two values are determined by the insulating properties of the gate dielectric and semiconducting properties of the IGZO semiconductor film, and that they are independent of the dimensions of the device.

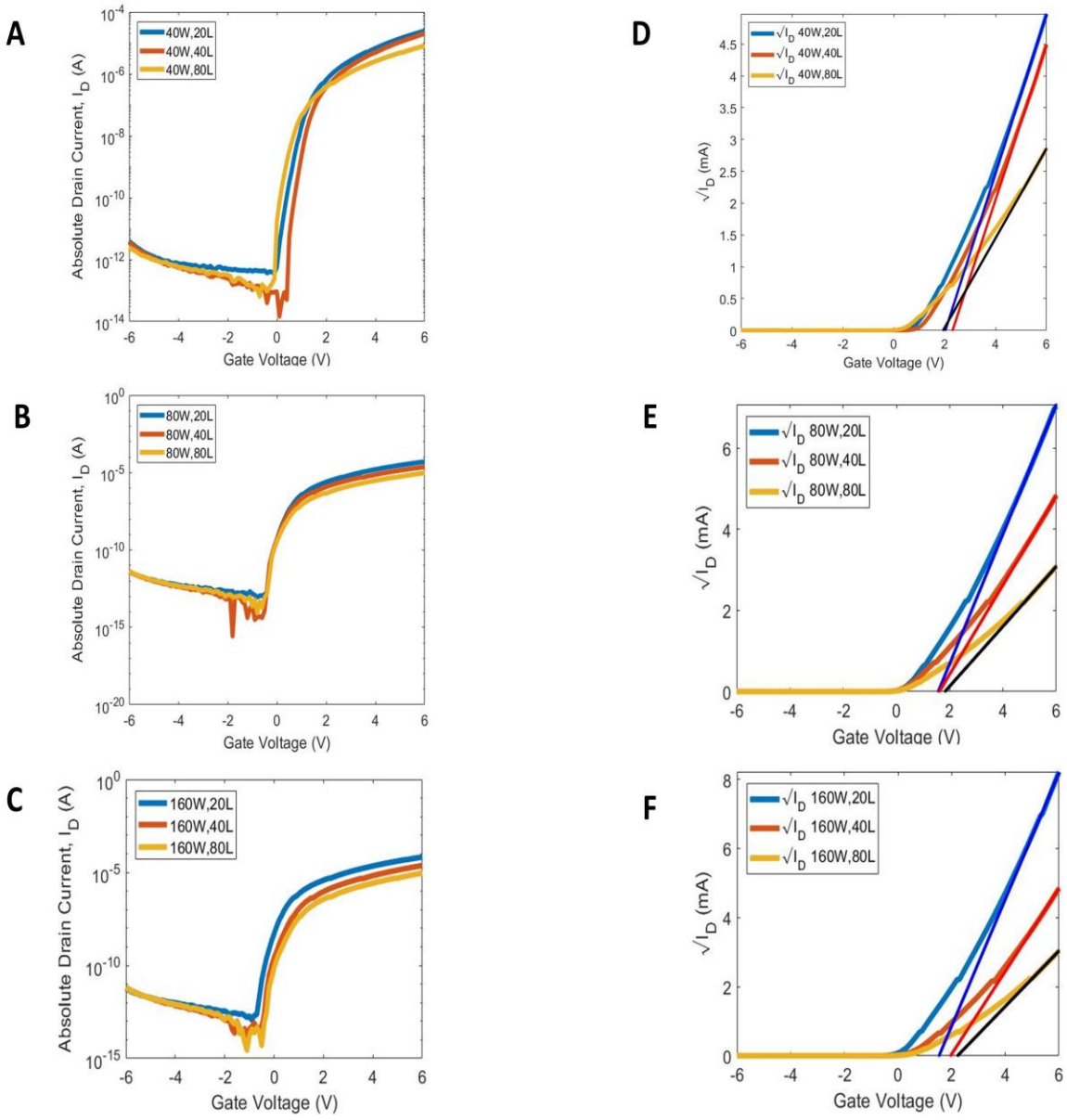

Figure 4.3. Measurements for different device dimensions, including (A-C) transfer curves (I_D-V_G) and (D-F) plots of $\sqrt{I_D}$ versus V_G, and the linear fits from which V_T and μ_{sat} are extracted.

Device channel widths were 40, 80 and 160 µm, and channel lengths were 20, 40, and 80 µm. Figure 4.3 A-C show the transfer curves (I_D-V_G) for these nine devices. Figure 4.3 D-F show the plots of $\sqrt{I_D}$ vs V_G. For each plot in Figure 4.4 D-F, a linear fit to the data allows for the calculation of V_T and μ_{sat} for each of the transistors. The average V_T was found to be 1.9 ± 0.1 V and the average μ_{sat} was found to be 2.6 ±0.5 $cm^2V^{-1}s^{-1}$ (mean ± SEM for N=9 transistors).

The device substrate was stored on a shelf for nine days and the devices were re-measured periodically, as a preliminary test of lifetime and stability. It is important to note that, unlike the OLED, the active area of the TFT was not encapsulated. After the first 48 hours of the lifetime test, the average V_T was found to have increased to 2.3 ±0.1 V, representing a 20% increase in V_T. The average μ_{sat} increased to 5.3 ± 0.6 $cm^2V^{-1}s^{-1}$, representing a 100% increase in mobility. Figure 4.4 shows how average V_T and average μ_{sat} change over the course of the test.

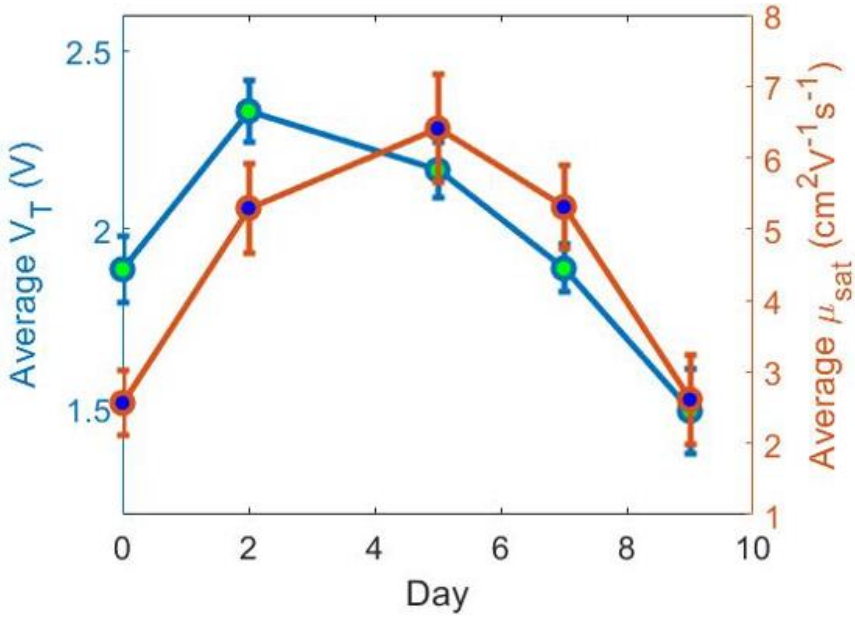

Figure 4.4. A plot of average V_T and average μ_{sat} for 9 TFTs over a nine day lifetime test, in which devices were tested on days 0, 2, 5, 7, and 9.

At the end of the lifetime test, the average V_T was found to have decreased to 1.5 ±0.1 V, representing a 20% decrease in V_T relative to day one. The average μ_{sat} was calculated to be 2.6 ± 0.6 $cm^2V^{-1}s^{-1}$, which is similar to the value calculated on day one. The instability seen in V_T and μ_{sat} is not unexpected for IGZO TFTs, as both of these values can be modulated by oxygen content in the IGZO film and in the environment (Jeong et al. 2008). Conduction in metal oxide films, such as IGZO, is due to oxygen vacancies that contribute free electrons in the conduction band of the material (Vanheusden et al. 1996). Hence, the conductivity of the IGZO film changes as the oxygen content of the film changes (Yao et al. 2011). As deposited, a sputtered IGZO film has defects, which introduce traps that change conductivity of the film and effect device performance. A post-deposition wet or dry thermal anneal, has been shown to eliminate defects and reduce shifts in V_T (Nomura et al. 2009). However, over time, the device may adsorb additional oxygen from the environment, which also results in changes in device performance. Strategies to eliminate instability in device performance due to this effect have included passivating the channel region and the active area of the completed device (Chen et al. 2011; Görrn et al. 2009; Hayashi et al. 2008). Implementing an annealing and device passivation step in this device fabrication is expected to improve device stability.

4.4 Conclusions

Fabrication of a TFT with a sputtered IGZO active layer has been demonstrated. The transistor supplies 0.4 μA and 1.1 μA of driving current, indicating that the TFT is capable of driving both green and blue OLEDs described in Chapter 3 to a minimum threshold brightness of 100 cd/m^2.

However, the unencapsulated TFT is not particularly stable on the shelf, as a 20% decrease in V_T was observed over the course of a nine-day lifetime test. A change in V_T reflects overall changes in the output performance of the device. Over time, the gate voltage required to supply driving current to the OLED will also change. This instability would present difficulties for a potential user of the integrated substrate, as the gate voltage needed to optically stimulate plated tissues at a constant brightness over the course of an experiment may change. While this preliminary work establishes proof of concept for the integrated substrate, advancing this work will involve exploring methods to increase the stability of the TFT performance over time.

CHAPTER 5

INTEGRATION OF THIN FILM ELECTRONICS AND MEA TECHNOLOGIES FOR A MULTIFUNCTIONAL SUBSTRATE

Chapters 2, 3, and 4 present the fabrication and characterization of functional discrete MEA, OLED and TFT components. In Chapter 2, fabrication of an MEA with gold electrodes and parylene encapsulation was demonstrated. In Chapter 3, fabrication of green and blue OLEDs was demonstrated, and driving current requirements were established. Lastly, Chapter 4 reported the fabrication of a TFT, and the output performance of the device indicates that the TFT is capable of driving both colors of OLEDs. Having demonstrated functional discrete components, in this chapter we demonstrate the proposed integrated substrate for application in *in vitro* optogenetic neuroscience experiments. This chapter describes the integration of the three components on a single glass substrate, presents the component layout and substrate design, and discusses the rationale for the development of the fabrication traveller and the order of fabrication steps. A short discussion of the limitations of this work concludes this chapter

5.1 Introduction

5.1.1 Literature review

As discussed in Chapter 1, proposed substrates for *in vitro* optogenetics work have been fabricated, but none of them feature substrate-integrated MEA and optical stimulation technologies. Platforms that feature substrate-integrated LEDs or OLEDs have been fabricated (Smith et al. 2014; Tokuda et al. 2013). In work by Smith et al. (2014), the authors report on the fabrication of a substrate-integrated array of OLEDs driven by TFTs, for matrix-addressable

stimulation. This work does not feature any substrate-embedded recording technology for recording electrical activity from cultured tissues, unlike the substrate that is proposed in this dissertation. In work by (Tokuda et al. 2013), the authors report a substrate that is fabricated with an embedded LED array and a CMOS-based imaging technology that allows the user to visualize plated tissues, but this device also lacks any substrate-embedded recording technology. A potential user of either of these substrates would also have to invest in a patch-clamp recording apparatus in order to measure tissue responses to optical stimulation. In addition to being costly and having a steep learning curve, a patch clamp system can record from one to a few cells, at best, which may be a disadvantage to a user that is interested in observing network level activity from the cultured tissue.

Other approaches to the integration of recording and stimulation have focused on the fabrication of an MEA substrate and utilizing a light source directed at the substrate or is attached to the substrate. Variations on this type of approach include delivering radiation via an objective lens (Sakar et al. 2012), affixing fiber optic cables to the substrate (Renault et al. 2015), or fabricating substrate-integrated waveguides to deliver light from sources such as LEDs (Welkenhuysen et al. 2016). A disadvantage for this approach is that it requires a stand-alone piece of equipment to deliver light, which is a potential barrier that prevents the adoption of optogenetics technologies. For strategies that requires attaching waveguides or cables to the substrate, it may be difficult to position waveguides or cables on the MEA electrode in a manner that is precise and reproducible, which may present issues to users that wish to explore spatial relationships between active units in a culture (Del Bene and Wyart 2012)

To date, our proposed substrate is the only platform that integrates MEA recording technology with OLEDs as a source of optical stimulation. Integrating these three technologies on a substrate will have three key advantages. One, because dimensions of the OLED and the location of the OLED relative to the MEA electrode are defined by photolithography, the location and the dimensions are produced in a manner that is more reliable and reproducible than current technologies that utilize attached fiber optic cables. Additionally, modification of locations or scaling of the dimensions of the OLED and/or the MEA electrode is easily achieved by modifying photolithography masks, which lends itself to rapidly-prototyped and cost-efficient variations of stimulation and recording experiments. Lastly, fully integrating the optical stimulation component of the optogenetics experiment on the substrate eliminates the need for costly stand-alone light sources and/or waveguides. With a substrate adapter that can access both the MEA electrodes and the backside electronics, both recording and stimulating technologies can be operated simultaneously by using a single piece of hardware, which is shown in Figure 5.1. This substrate streamlines the necessary hardware and introduces a "plug and play" aspect to *in vitro* optogenetics experiments that previously did not exist. We anticipate that these advantages will increase the number of users that adopt optogenetics technology.

5.1.2 Proposed device layout and fabrication process flow

The proposed device features an array of square MEA electrodes. The electrodes have a side length of 50 μm. The parylene encapsulation is patterned over the electrode to form a circular opening with a diameter of 30 μm. The electrodes are attached to bond pads with dimensions of 0.075 cm x 0.1 cm. The MEA electrodes are in groups of 4, arranged such that there is an electrode at the corner of a square OLED pixel. The pixel has a side length of 100 μm.

The distance from edge to edge of an MEA electrode is 250 μm. The distance from the edge of the OLED pixel to the edge of an MEA electrode is 75 μm. An OLED is connected to the drain electrode of the TFT. The TFT has 40 μm x 20 μm channel width and length dimensions.

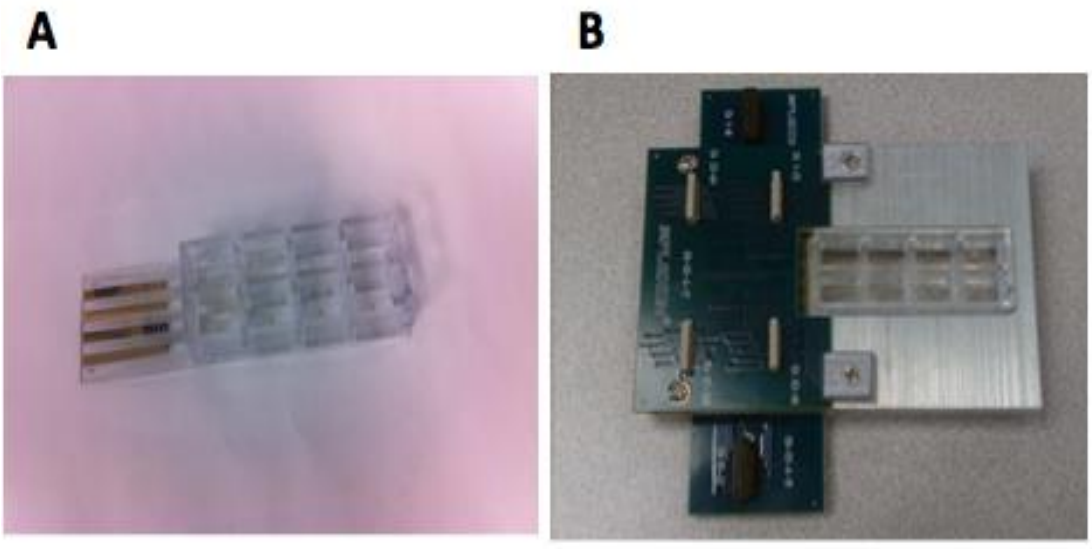

Figure 5.1. Images of the utilization of a the completed multifunctional substrate, including (A) an image of a substrate with an attached array of polycarbonate cell culture wells, and (B), an image of a custom clamshell adapter for operating both MEA and OLED components.

An array of 4 TFTs share a common gate electrode, with dimensions 0.35 cm x 0.1 cm, and have individual source electrodes, with similar dimensions, that allow for matrix-addressable operation of the OLEDs. An image of this layout is shown in Figure 5.2, which shows 16 MEA electrodes, 4 OLEDs, and 4 TFTs.

An image of the entire substrate layout is shown in Figure 5.3. The full proposed substrate contains two integrated MEA substrates per piece of ITO glass. Each MEA substrate has 64 MEA electrodes, 32 OLED pixels, and 32 TFTs. The finished MEA is 8 cm long and 2.5 cm wide. The substrate also includes 6 test TFT structures with 40 μm x 20 μm channel width and length dimensions. The gate, source, and drain contacts for these devices are easier to access

with probe station tips than the integrated TFTs for easier device testing. The active area of an integrated micropixel is too small to be detected by the spectrophotometer, so the integrated substrate also contains four OLED test pixels, with an area of 10 mm^2 each.

The order of device fabrication steps and the processing conditions are taken into careful consideration in this project, since front- and backside functionality are part of the novelty of this project. If the process flow is poorly designed, then fabrication on the backside of the device may degrade fabricated devices on the frontside. A schematic of the proposed process flow is shown in Figure 5.4.

Material tolerance during handling is the key characteristic that determines the order of fabricating the three components. Since the MEA is fabricated in a few steps from relatively inert, robust materials, it is fabricated first. The gold electrodes and traces are patterned and encapsulated with a blanket film of parylene, but the parylene film is not patterned. Since parylene is chemically inert and has a high melting point (290 °C), this film should be robust enough to protect the MEA electrodes during the fabrication of the TFTs and the OLEDs. The parylene film is patterned during a later step in substrate fabrication, in order to form MEA electrode areas and bond pad openings.

Next the backside devices are fabricated. Knowing that the organic semiconductor materials used in OLED fabrication are highly sensitive to oxygen and moisture, the TFT is fabricated before the OLED. Lastly, the OLED stack materials are deposited, and the completed OLED pixels are encapsulated.

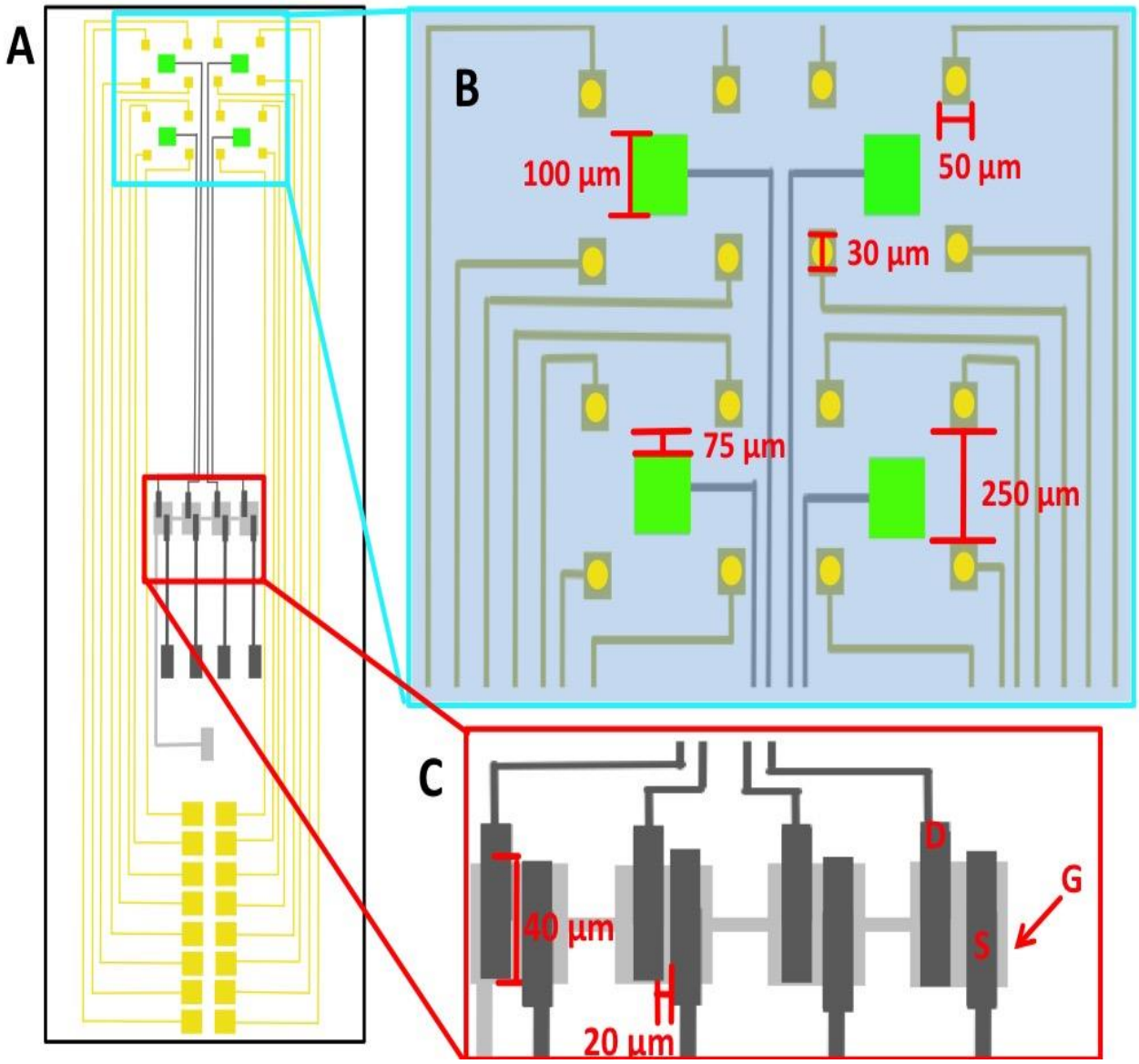

Figure 5.2. A schematic image of the proposed integrated substrate (A). Note that the OLEDs (green) and the TFTs (grey) are on the back side of the substrate, while the MEA array is on the front side. The inset in (B) shows the spatial relationship between 16 MEA electrodes (yellow) and 4 OLED pixels, and the blue field represents parylene encapsulation, that is patterned to form circular openings on the MEA electrodes and the OLEDs. The inset in (C) shows the dimensions of four TFTs, and the location of the source (S), drain (D), and common gate (G) electrodes.

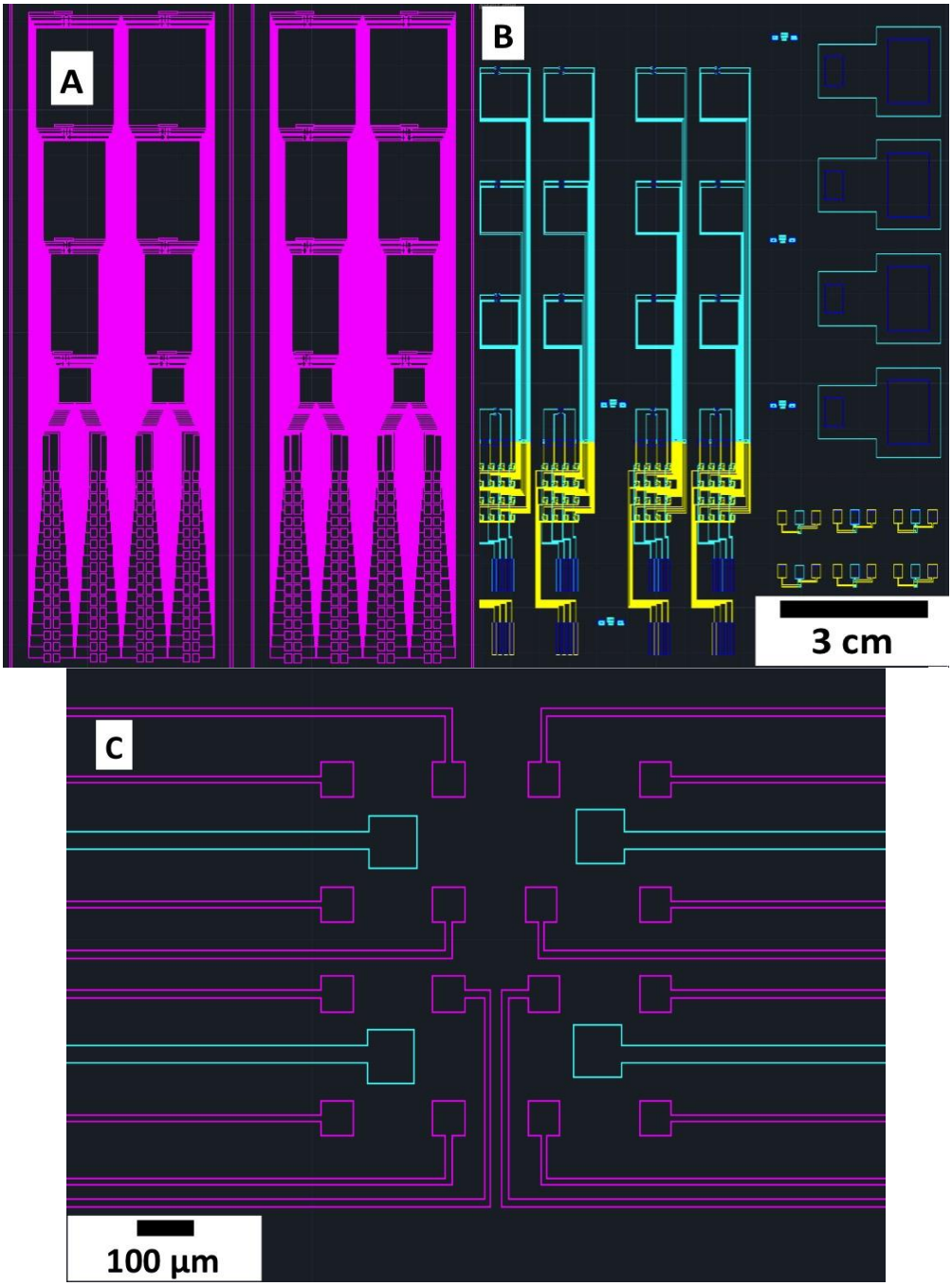

Figure 5.3. Image of CAD layout of the proposed integrated substrate, including (A) two arrays of 64 MEA electrodes on the front side of the substrate (magenta), (B) the backside OLED (cyan) and TFT layout (yellow), and (C) overlay of the MEA electrode (magenta) and OLED traces (cyan).

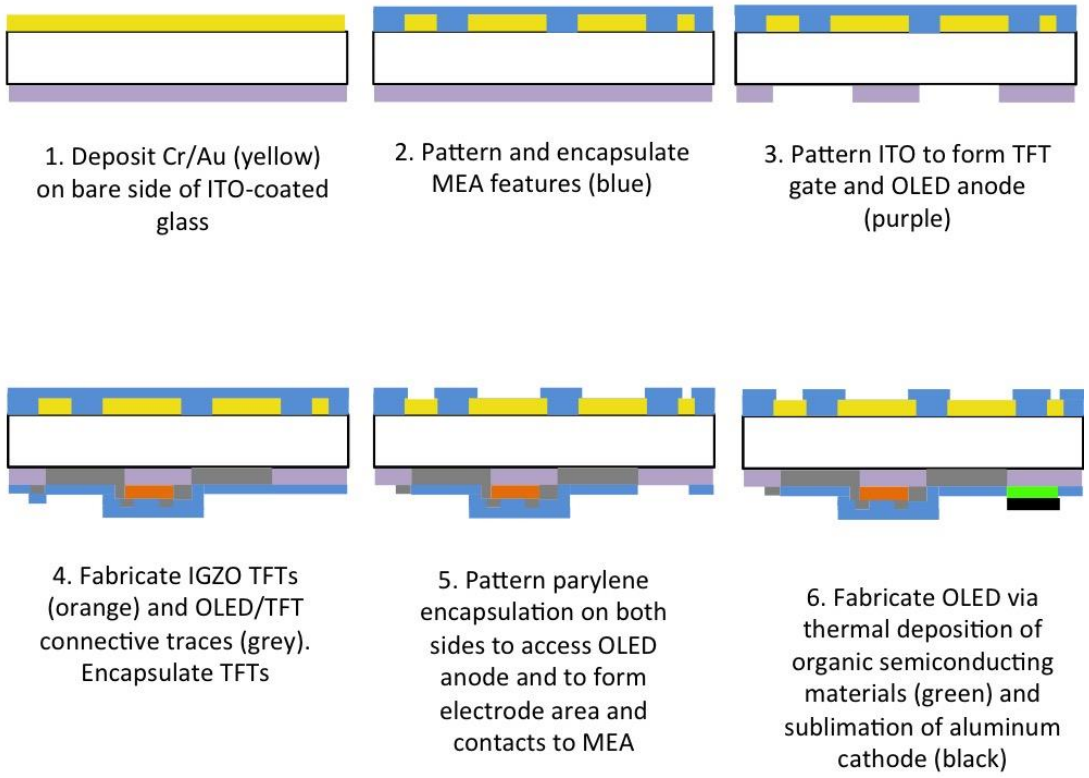

Figure 5.4. A schematic process flow that shows a general overview for steps in fabricating the multifunctional, integrated substrate.

5.2 Methods: Substrate Fabrication

Substrate fabrication began with a glass substrate coated on one side with a blanket film of ITO from Luminescence Technology Corporation (Taiwan). The glass substrate was cleaned with sonication in acetone, isopropyl alcohol, and deionized water for five minutes each. The substrate was dried with N_2 and baked at 100° C for five minutes.

In the next step, the ITO side of the substrate was protected from processing steps with a photoresist film. AZ nLOF 2020, a negative photoresist, was spin-cast on the ITO surface. After a 1 minute thermal cure at 100° C to evaporate solvent, the resist was exposed with UV light,

followed by a post-exposure bake for one minute at 100° C, in order to completely cure the resist. The resulting cured polymer film, which is about 2 μm thick, protects the ITO from mechanical abrasion and wet etchants during MEA fabrication.

Next, the MEA was fabricated. Chromium and gold were deposited on the bare side of the substrate, using electron beam evaporation. The metal films were patterned using the standard S1813 photolithography procedure and wet etch using gold and chromium etchants. The MEA was prepared for parylene deposition by cleaning the substrate in O_2 plasma at a pressure of 140 mT and 50 W power for 1 minute. Prior to parylene deposition, the ITO side is covered in Kapton tape; the Kapton film acts as a barrier to parylene deposition on this side of the substrate. Next, 500 nm of parylene is deposited on the MEA electrodes using 900 mg of parylene dimer and the standard chemical vapor deposition process. The parylene is not patterned immediately after this step, as the blanket film will protect the MEA array from mechanical abrasion and chemical etchants during the fabrication of the TFT and OLED components.

In the next step, the ITO film was patterned into OLED cathodes, TFT gate electrodes, and traces that connect the two components. The ITO was patterned using S1813 standard photolithography processes and a 10.5 minute etch using concentrated HCl. Next, blanket films for TFT fabrication were deposited. This stack of films includes 30 nm of HfO_2 deposited by atomic layer deposition, 30 nm of IGZO deposited by RF magnetron sputtering, and 500 nm of parylene deposited by chemical vapor deposition. Just prior to parylene deposition, the substrate was taped to a carrier wafer, with Kapton tape sealing the top edge of the substrate to the carrier, in order to prevent additional parylene deposition on the MEA side of the substrate.

Next, HfO_2, IGZO, and parylene were patterned using standard S1813 photolithography processes. Parylene was etched using an O_2 plasma with a pressure of 140 mT and 50 W power. IGZO was etched using HCl diluted in water, 1 part to 1000, for 15 seconds. Lastly, HfO_2 was etched using buffered oxide etch, diluted 7:1, for 11 minutes. After patterning these blanket films into the TFT active area stack, channel dimensions were defined by etching vias into the parylene film using standard S1813 photolithography and O_2 RIE etch processes.

Next, a blanket film of aluminum was deposited using RF magnetron sputtering. This film was patterned into TFT source and drain contacts and metal traces that connect OLED and TFT features. Patterning was achieved using standard S1813 photolithography and a wet etch with phosphoric acid heated to 85 °C as the etchant. At this point, TFT fabrication was completed, and these devices were encapsulated with 500 nm parylene, deposited using chemical vapor deposition. This parylene film protected the TFTs from damage during OLED fabrication. Prior to parylene deposition, the substrate is taped to a carrier wafer to prevent parylene deposition on the MEA side of the substrate. This parylene film was patterned using standard S1813 photolithography and O_2 RIE etch processes in order to open source contacts to the TFTs and define the active area of OLEDs.

After patterning this parylene encapsulation on the backside, the substrate was flipped over, and the parylene encapsulation on the MEA array was patterned, using standard photolithography and O_2 plasma etch processes. Patterning this film opens contacts to the MEA electrodes and the MEA bond pads.

Finally, OLEDs were fabricated using thermal evaporation processes. The substrate was prepared for organic semiconductor and cathode deposition by taping the substrate to the Cooke

system sample holder. A custom-made shadow mask that is open where OLEDs are fabricated and covered elsewhere was used to define the areas for deposition. The shadow mask was taped to the substrate. Then, OLED stack materials were deposited using thermal evaporation.

After the deposition system cooled, the substrate was removed from the deposition chamber, but remained in the inert N_2 environment inside the glove box, where the OLED pixels were encapsulated with UV-curable epoxy and glass slides. After curing the epoxy with a small UV lamp, fabrication was completed. Full details from all fabrication processes can be found in Appendix D.

5.3 Results

Images of a completed integrated substrate are shown in Figure 5.5. The completed substrate features a 64 electrode MEA array, 32 IGZO TFTs, and 16 green OLEDs.

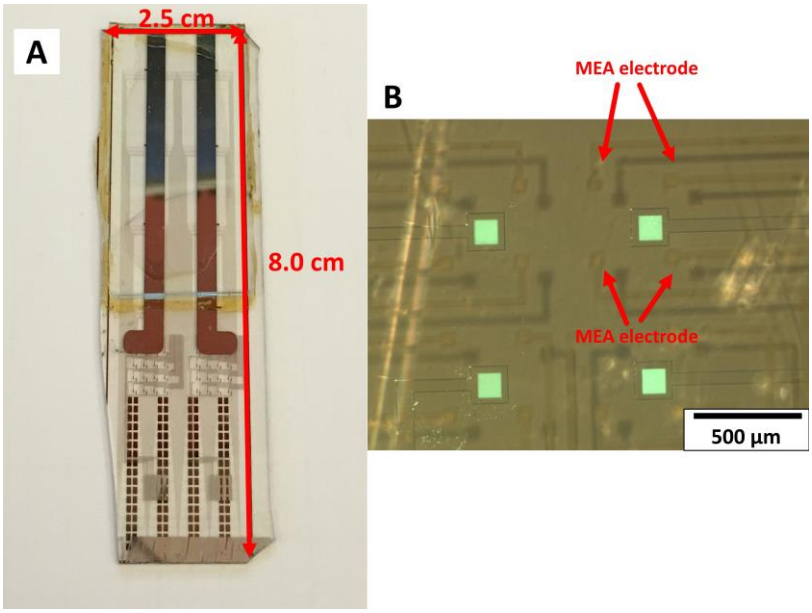

Figure 5.5. An image of a completed integrated multifunctional MEA substrate (A), and (B) a magnified image of MEA electrodes and traces and illuminated green OLED pixels driven at 8 V.

Due to the small size of the substrate pixels, it was not possible to measure spectral or electrical data from these devices. However, a spectral output and current-luminescent characteristics of one of the 10 mm^2 test pixels is presented in Figure 5.6. The pixel turns on at 4 V. The spectral output was collected at 6 V, while the current-luminescent measurements were collected while driving the device from 0-9 V.

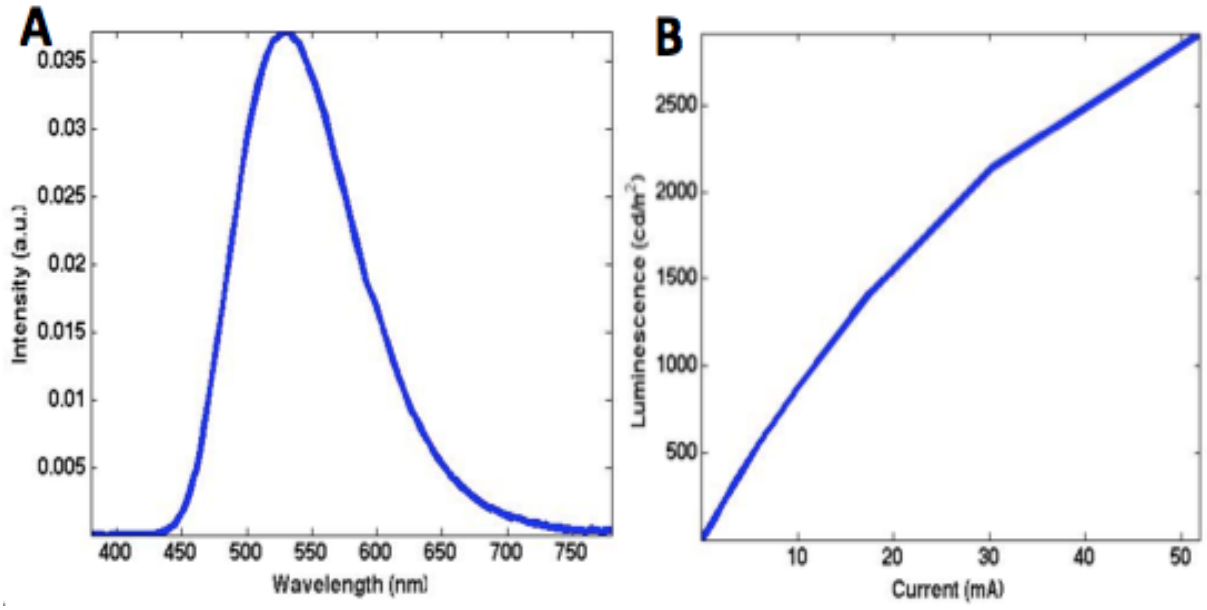

Figure 5.6. Output measurements from green OLED 10 mm^2 test pixels on the integrated substrate, including (A) spectral output at 6 V and (B) current-luminescent characteristics collected while driving the device from 0-9 V.

From Figure 5.6A, the peak output wavelength is 528 nm, which indicates that the device is capable of stimulating the bacteriorhodopsin protein in an optogenetics experiment. The current-luminescent profile in Figure 5.6B, indicates that the test pixel is turned on to a threshold luminescence of 100 cd/m^2 with a driving current of 1.0 mA. The smaller pixels on the device should require 1.0 μA of current.

Prior to TFT encapsulation with parylene, one of the TFT test devices was measured. The transfer curve for the device is presented in Figure 5.7.

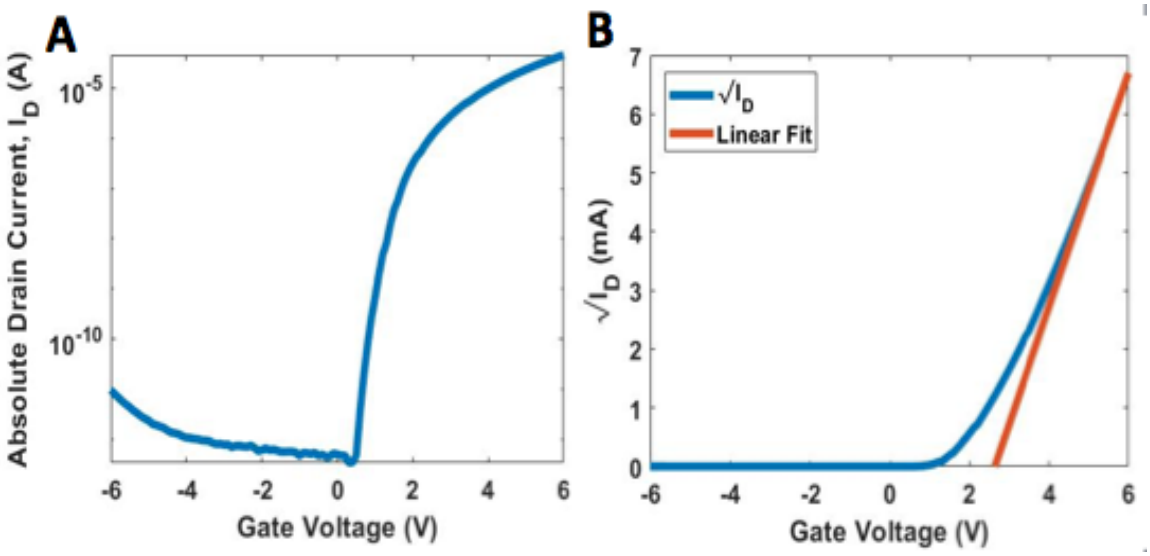

Figure 5.7. (A) Transfer curve measurements from a completed test TFT on the integrated substrate, and (B) the linear fit to the plot of $\sqrt{I_D}$ versus V_G. A 6.0 V drain voltage was applied while the gate voltage was swept from -6.0 V to 6.0 V.

From Figure 5.7A, the TFT delivers 1.1 μA of current at a gate voltage of 2.5 V, indicating that the TFTs on the substrate are able to drive the green OLED micropixels. From Figure 5.7B, the V_T is calculated to be 2.5 V and μ_{sat} was calculated to be 3.4 $cm^2V^{-1}s^{-1}$.

As of the date of this dissertation, a fully functional substrate with blue OLEDs has not been attempted. We anticipate that blue OLED fabrication will easily integrate with the process flow presented in this chapter.

5.3 Conclusions and limitations to this work

The fabrication of an integrated multifunctional substrate featuring MEAs, OLEDs, and TFTs has been demonstrated. The fabrication process results in a substrate with green OLEDs to stimulate bacteriorhodopsin in an optogenetic experiment. The manufacturability of this substrate is the main factor that has impeded studies utilizing this substrate in an *in vitro*

neuroscience experiment. As seen in the work reported in Chapter 2 and elsewhere, a number of substrates are used in *in vitro* MEA studies in order to collect data that is statistically significant. Testing this multifunctional substrate in an *in vitro* cell culture experiment should be no different, and a minimum of 10 of these substrates would be necessary. While we were able to produce substrates that demonstrate the proof of concept of the three-component integration and front- and backside processing, we were not able to produce enough fully functioning substrates to carry out meaningful *in vitro* optogenetic experiments

CHAPTER 6

A PATTERNED POLYSTYRENE-BASED MICROELECTRODE ARRAY FOR *IN VITRO* NEURONAL RECORDINGS

Substrate-integrated microelectrode arrays (MEAs) are non-invasive platforms for recording supra-threshold signals, i.e. action potentials or spikes, from a variety of cultured electrically active cells, and are useful for pharmacological and toxicological studies. However, the MEA substrate, which is often fabricated using semiconductor processing technology, presents some challenges to the user. Specifically, the electrode encapsulation, which may consist of a variety of inorganic and organic materials, requires a specific substrate preparation protocol to optimize cell adhesion to the surface (Berthier et al. 2012; Charkhkar et al. 2016). Often, these protocols differ from and are more complex than traditional protocols for *in vitro* cell culture in polystyrene petri dishes. Here, we describe the fabrication of an MEA with indium tin oxide microelectrodes and a patterned polystyrene electrode encapsulation. We demonstrate the electrochemical stability of the electrodes and encapsulation, and show viable cell culture and *in vitro* recordings.

This work was the result of a collaborative effort between the Gnade and Pancrazio groups at the University of Texas at Dallas that resulted in a manuscript that was submitted to the Journal of Biomedical Microdevices in March 2018, but was not accepted for pubication as of the date of this dissertation. I, the lead author on the manuscript, fabricated the MEA susbstrates. Rashed Rihani, a graduate student in the Pancrazio group, performed impedance measurements and some data analysis. Dr. Bryan Black, a research associate in the Pancrazio lab, performed cell culture,

neuronal recordings, and data analysis. Dr. Bruce Gnade and Dr. Joseph Pancrazio are professors at UT Dallas, and they were the principal investigators that oversaw this work.

6.1 Introduction

Substrate integrated microelectrode arrays (MEAs) offer a means of non-invasively measuring activity from electrically active cells *in vitro.* Compared to patch clamp techniques, the MEA is a relatively high-throughput approach for monitoring action potentials or spikes from populations of cells simultaneously. MEAs have been applied as a drug-screening platform (Colombi et al. 2013; Johnstone et al. 2010; Navarrete et al. 2013; Stett et al. 2003; Xiang et al. 2007), used for analysis of engineered networks for studying neural dynamics (Chang et al. 2000; Hasan and Berdichevsky 2016), and biosensor applications (Charkhkar et al. 2014; Gramowski et al. 2004; Pancrazio et al. 2003; Pancrazio et al. 1999; Scarlatos et al. 2008). The device features a planar substrate with conductive electrodes encapsulated by a dielectric material. The dielectric is patterned to open electrode contacts and bond pads to interface with recording hardware. Many types of devices have been developed in laboratories and some are commercially available. The vast set of encapsulation materials used on these devices includes silicon dioxide (Mastrototaro et al. 1992), silicon nitride (Connolly et al. 1990), and polymeric materials such as photoresists (Gross et al. 1977), parylene (Charkhkar et al. 2016), polydimethylsiloxane (PDMS) (Nam, Musick, Wheeler 2006), polyimide (Oka et al. 1999), and SU-8 (Zhang et al. 30 September 2010). However, the vast majority of conventional *in vitro* cell culture techniques, including protocols for excitable cells, make use of polystyrene petri dishes and culture flasks. Consequently, adoption of MEA technology requires users to modify

protocols to optimize cell attachment and viability on the MEA substrate, and some of these materials may introduce artifacts into cell culture work (Berthier et al. 2012).

This chapter describes the design and development of an MEA prototype device, fabricated with semiconductor processing technology and based on a polystyrene encapsulation layer. We show that the polystyrene film can be etched to created microelectrode contacts with consistent electrochemical impedance. We also show cortical neuron viability and function for at least 29 days in vitro with well-resolved single units.

6.2 Methods

6.2.1 Fabrication and Characterization

Figure 6.1 shows the MEA with a cross-sectional schematic with constituent material layers. Fabrication of the electrode array began with a commercially available ITO-coated glass substrate (Luminescence Technology Corp., Taiwan). The outer dimensions of the substrate were 4.9 cm x 4.9 cm and the substrate was 1.1 mm thick. The ITO film is 1200-1600 Å thick and has a sheet resistance of 15-19 Ω/□.

Standard S1813 photolithography and 10.5 minute wet etch processes with concentrated HCl were used to pattern the ITO film into an array of 60 square microelectrodes with a side length of 30 μm, square bond pads with a side length of 2 mm, and connecting leads. The substrate was prepared for polystyrene adhesion by dip-coating with γ-methacryloxypropyltrimethoxysilane (A-174) (Specialty Coating Systems, USA). A 1% solution of the adhesion promoter was prepared in a 1:1 mixture of deionized water and isopropyl alcohol, and the mixture was allowed to react for 2 hours after preparation.

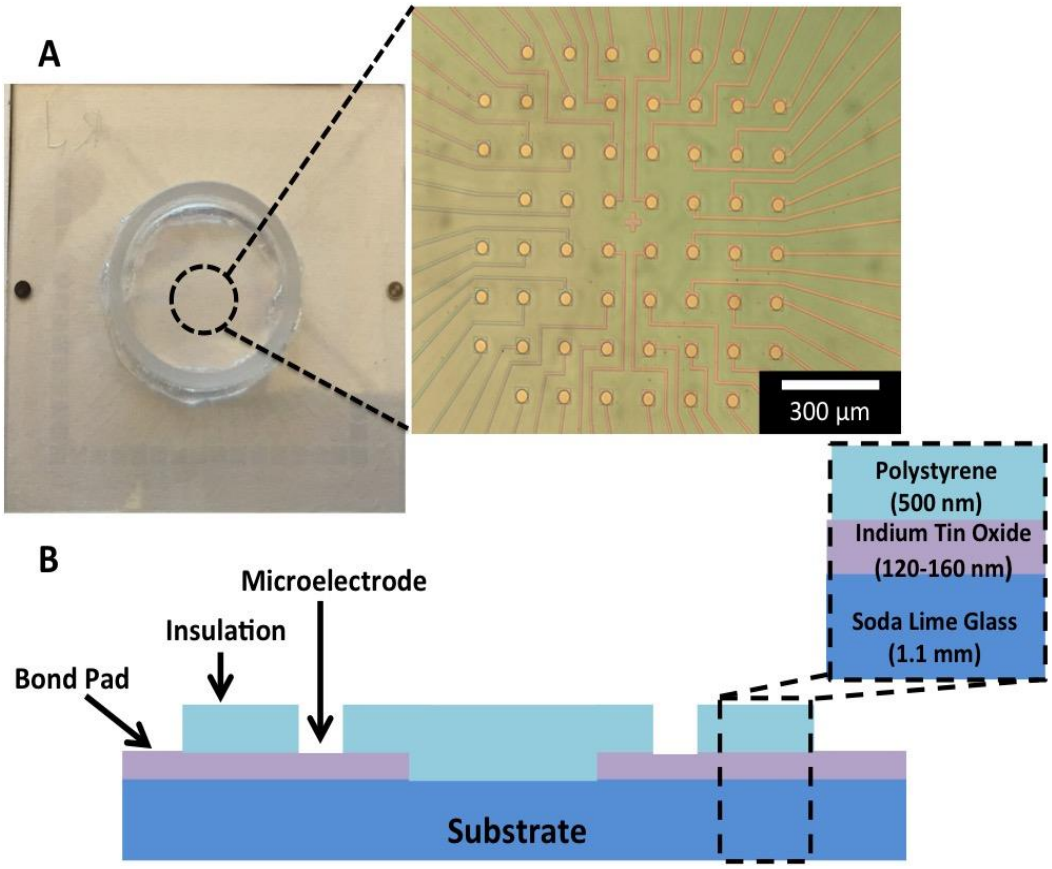

Figure 6.1. An optical image of the transparent polystyrene-encapsulated MEA with magnification showing the microelectrodes (A), and a cross-sectional schematic of the MEA showing the different materials and film thicknesses of each layer (B).

The substrates were soaked in the solution for 30 min, and then the excess solution was poured off and the substrates were allowed to air dry for 30 min. After the drying period, the substrates were rinsed for 30 sec in fresh isopropyl alcohol with gentle agitation, and then the substrates were dried with N_2. The polystyrene encapsulation was deposited by spin-casting from a solution of 0.04 g/mL of polystyrene. The polystyrene solution was prepared from polystyrene pellets, average molecular weight ~280,000 (Sigma-Aldrich, USA), dissolved in toluene, and the solution was mixed for 2 hours at 70 °C while stirring. Residual solvent from the cast film was evaporated with a thermal cure at 90 °C for 1 hour on a hot plate. For an ITO lead 10 µm wide

and length of approximately 1 cm, the shunt capacitance across the layer of polystyrene insulation, with relative permittivity of 2.6, was estimated to be 230 pF/nm thickness. To minimize effects of shunt capacitance, polystyrene was spin cast to a thickness of 500 nm yielding a high shunt impedance of 346 MΩ at 1 KHz. Consequently, for a microelectrode with an impedance of approximately 1 MΩ at 1 KHz, we anticipate minimal impact of the shunt impedance.

The polystyrene film was encapsulated with a 150 nm PECVD oxide hardmask film deposited at 100 °C. This hard mask allows for subsequent patterning and etching of the polystyrene film. The oxide film was patterned using S1813 photolithography and a 30 sec buffered oxide etch 7:1 wet etch. Next, the polystyrene film was patterned via exposure to oxygen reactive ion etching (Sirius T2, Trion Technology, USA), at 200 mT O_2 and 200 W. The etch rate was approximately 50 nm/min. The S1813 resist was removed using blanket UV exposure and MF-319 base developer, and the oxide hardmask was removed with a 30 sec BOE 7:1 wet etch. This wet etch is selective to the hardmask film and does not etch exposed ITO features. Lastly, a polycarbonate ring with height of 0.6 cm, 2.0 cm inner diameter, and 2.2 cm outer diameter was attached to the surface of the substrate with a silicone adhesive (MED1-4213, Nu-Sil, USA). The ring functioned as a well that contains plated tissues and liquid media.

Electrochemical characterization of MEA electrodes was performed by electrochemical impedance spectroscopy (EIS) on 8 representative microelectrodes from 3 substrates. The measurements were performed using a two-electrode configuration using a potentiostat/galvanostat (CH 600D, CH Instruments, Texas, US) equipped with an electrochemical analyzer module (CHI Version 9.03, CH Instruments). Measurements were

made in the presence of phosphate-buffered saline (PBS) at pH of 7.4 at room temperature by applying a sinusoidal signal with 20 mV amplitude over a range of frequencies from 10 Hz to 100 KHz to characterize the complex impedance of the working electrode and the electrolyte solution.

6.2.2 MEA preparation and Cell Culture

Prior to culture, polystyrene-encapsulated MEA surfaces were exposed to oxygen plasma (UV-1, Samco Inc., USA) with an O_2 flow of 0.7 L/min at atmospheric pressure for 15 min and sterilized by 12 hour exposure to ethylene oxide. One day before seeding, the center of each MEA was coated with 50 µg/ml of poly-D-lysine (PDL) (Sigma-Aldrich, USA) and maintained at 37 ˚C overnight. The morning of culture, the PDL was aspirated from MEA surfaces, washed twice with sterile DI water, and treated with 5 µl of 20 µg/ml laminin for 1 hour.

Primary cortical neurons were dissected, dissociated, and cultured as previously described (Knaack et al. 2013). Briefly, anesthetized timed-pregnant CD-1 mice (embryonic day 14-16, Envigo, USA) were euthanized by cervical dislocation followed by decapitation. Embryos were extracted by cesarean section, decapitated, and placed in ice cold Hank's Balanced Salt Solution (Life Technologies, USA). Cortical regions were isolated with meninges removed, minced, and placed in dissociation solution containing DNAase and papain (Worthington Biochemical Corp., USA) for 15 minutes. The remaining tissue was further dissociated with mechanical trituration using fire-polished glass Pasteur pipettes. After centrifuging at 300x g for 5 min, the supernatant was removed and cells were re-suspended in culture medium containing 5% horse serum and 5% fetal bovine serum. Re-suspended cells were counted using a

hemocytometer and approximately 90,000 cells were seeded over the microelectrode grid at the center of each MEA. All cultures were incubated at 37°C with 10% CO_2 and maintained in DMEM with GlutaMAX supplemented with 5% horse serum, 5% fetal bovine serum, 2% B27, and 0.2 % of 4 mg/ml ascorbic acid (Sigma-Aldrich) for the first two days. To avoid overgrowth of glial cells, the fetal bovine serum was removed at day 3 and the cultures were thereafter maintained by a 50% media exchange twice a week for at least 29 days.

6.2.3 Extracellular Recordings and Analysis

Wide band (0.1 – 7000 Hz) extracellular voltage recordings were acquired from all 60 channels simultaneously at 40 KHz sampling rate using Plexon's OmniPlex data acquisition system (Plexon Inc, Dallas, TX). Stage-top environmental control maintained 37 ˚C, 95% humidity, and 10% CO_2 throughout all recordings. Prior to single unit sorting, wide band data was further filtered using a two-pole Butterworth bandpass (250 – 7000 Hz) filter and a spike detection threshold set to 5.5 times the standard deviation of the RMS noise level of each of the channels. Identified spikes were sorted manually using Plexon's Offline Sorter software based on 2D principal component analysis. The percentage of active channels was defined by those which exhibited distinguishable single unit activity with a spike rate greater than or equal to 5 spikes/min. The reported value includes electrode sites which exhibit relatively high impedances (above 5 MΩ) which may disallow high SNR recordings necessary for single unit discrimination. Calculation of mean spike rate was carried out using NeuroExplorer (Version 5, NEX Technologies, USA). Statistical analysis was performed using OriginPro software (OriginLab, USA).

6.3 Results

6.3.1 Characterization of surfaces

A-174 silane and UV/O_3 surface treatments were used to modify the substrate surface. The A-174 silane dip-coating procedure made the surface of the ITO-coated glass substrate more hydrophobic to promote adhesion of the spin-cast polystyrene film. Prior to the A-174 dip-coating process, the contact angle was 18.8 ± 0.3° (mean ± SEM, for N=10 contact angle measurements). After the dip-coating step, the contact angle increased to 50.6 ± 0.8°, which indicates that the substrate surface was made more hydrophobic by the A-174 to promote adhesion of the polystyrene film. The UV/O_3 surface treatment reduced the hydrophobicity of the polystyrene encapsulation, which we would anticipate to improve cell adhesion to the MEA surface. After device fabrication was completed, the contact angle of the polystyrene surface was 91.3 ± 1.0°. After the UV/O_3 treatment, the contact angle was reduced to 6.4 ± 0.4°, indicating that the polystyrene surface became more hydrophilic.

6.3.2 Electrode Impedance Stability

As shown in Figure 6.2, the measured impedance for representative electrodes on a set of MEA substrates ranges from 0.93 to 1.23 MΩ at 1 kHz, which is similar to previous observations of metal electrodes in saline solution (Charkhkar et al. 2016; Robinson 1968). The electrochemical stability of the electrodes and the polystyrene insulation was determined by comparing initial impedance to final impedance in two different conditions that are relevant to cell culture: before and after a standard ethylene oxide substrate sterilization protocol and then after 30 days of storage in a cell culture incubator at 37°C .

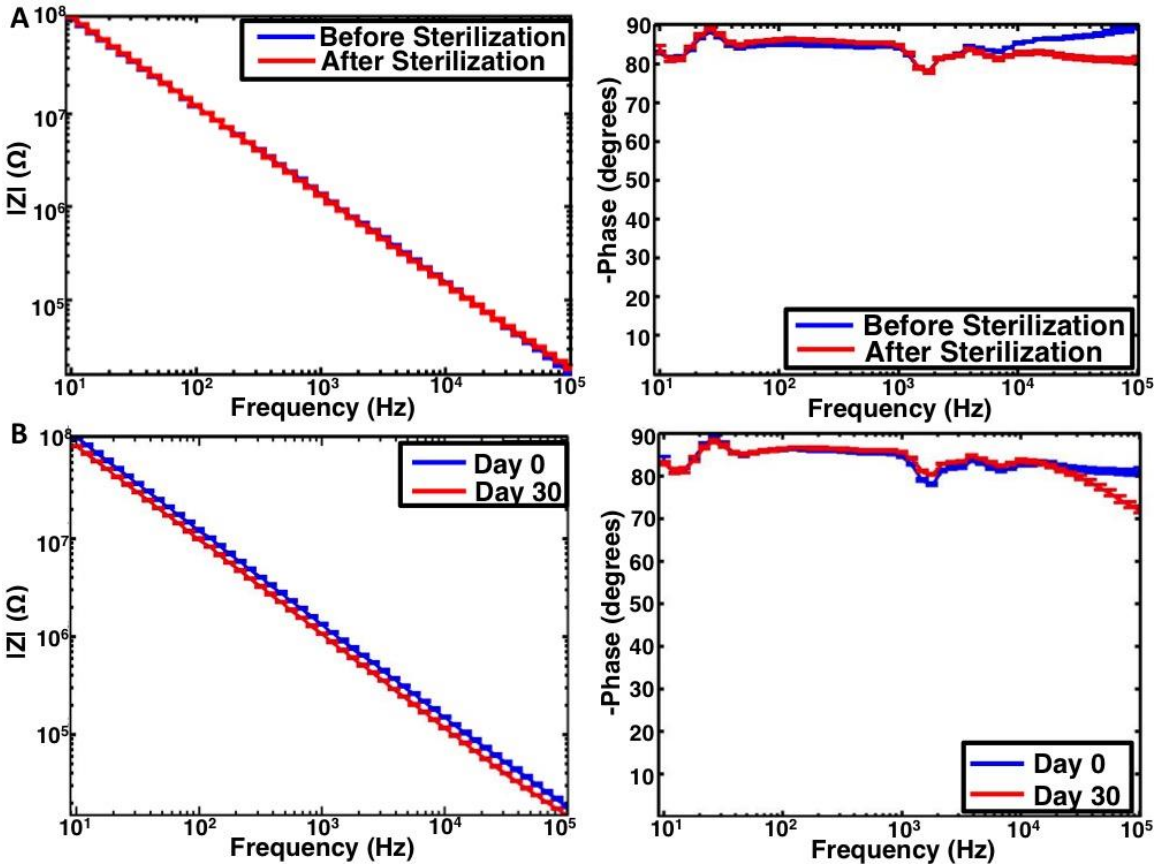

Figure 6.2. Electrochemical impedance stability of the polystyrene-encapsulated MEA. The impedance profile from ITO microelectrodes before and after ethylene oxide sterilization (A). The impedance profile from the ITO microelectrodes at day 1 (after ethylene oxide sterilization) and day 30 after storage at 37° C in PBS (B).

The initial impedance magnitude at 1 kHz was 1.37 ± 0.03 MΩ (mean ± SEM, for N=24 total microelectrode sites) while the impedance phase was -84.1 ± 0.3°. After the ethylene oxide sterilization procedure, the impedance magnitude at 1 kHz was 1.33 ± 0.03 MΩ and the impedance phase was -84.6 ± 0.2°, indicating electrochemical stability with sterilization. After the sterilization and maintenance in a cell culture incubator in the presence of PBS at 37°C, the impedance magnitude at 1kHz decreased to 1.07 ± 0.02 MΩ ($p < 0.05$) whereas the impedance phase did not significantly change -85.6 ± 0.2° ($p = 0.167$). While there is a change in impedance

over time, the impedance magnitude at 1 kHz after 30 days is still well within ranges necessary for good electrophysiological recordings (Charkhkar et al. 2016). These relative minor changes suggest that the polystyrene-encapsulated MEAs are sufficiently robust for *in vitro* neuronal culture applications.

6.3.3 Neuronal Culture

To evaluate the *in vitro* recording performance of polystyrene-encapsulated MEAs, we seeded dissociated embryonic mouse cortical neurons on 7 polystyrene-encapsulated MEAs and recorded extracellular activity for 29 days. Of the 7 devices seeded, 5 showed excellent cellular adhesion and viability at day-in-vitro (DIV) 21 (Figure 6.3A) and were considered for further analysis.

This successful culture yield is consistent with what our laboratory typically observes using commercially available single-well MEAs (75 – 80%). Extracellular action potentials, ranging in amplitude from 20 to 200 μV, could be readily recorded on single electrodes as early as DIV 7, with corresponding activity across multiple electrodes (indicative of functional network formation) emerging by approximately DIV 16. On DIV 29, successful cortical cultures exhibited spontaneous single-cell and network-level activity (Figure 6.3B) on 49.2 ± 4.6 % of electrode sites, with an overall mean firing rate of 3.0 ± 0.3 Hz and a signal-to-noise ratio (SNR) of 11.6 ± 0.5. These values are consistent with previously published observations using commercially available MEAs as well as novel, polymer-encapsulated MEAs (Charkhkar et al. 2015; Charkhkar et al. 2016).

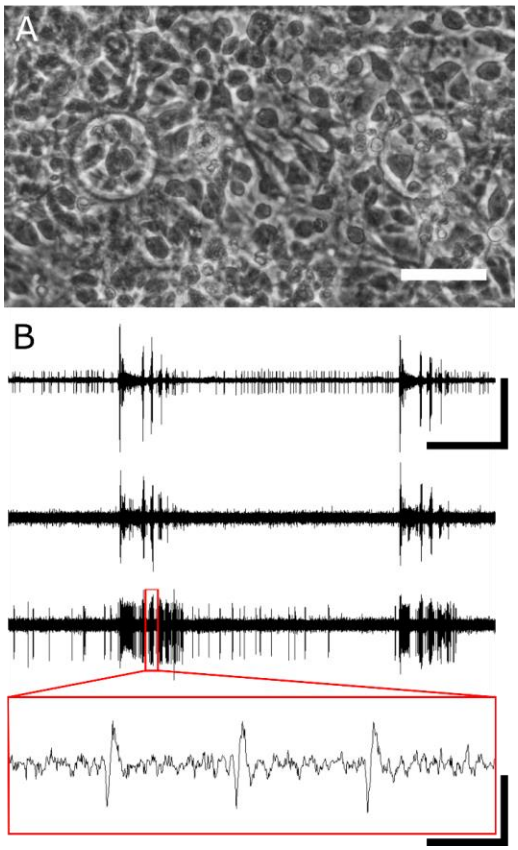

Figure 6.3. (A) Primary embryonic mouse cortical neurons cultured on a polystyrene-encapsulated MEA (DIV 7). Scale bar represents 30 µm (B). Representative bandpass-filtered extracellular recordings from 3 separate electrodes on a single device (DIV 29). Horizontal and vertical scale bars represent 5 sec and 85 µV. Expanded inset (highlighted in red) shows three characteristic action potentials. Inset horizontal and vertical scale bars represent 5 ms and 85 µV.

6.4 Conclusions

We have demonstrated the fabrication of a novel MEA with a polystyrene insulating layer, consistent with substrates typically used for *in vitro* cell culture protocols. The polystyrene film is electrochemically stable during typical cell culture handling, and viable cell culture and recordings have been demonstrated for 29 days.

Unlike the protocols for macroscopic *in vitro* cell culture, which are based on polystyrene culture flasks and petri dishes, cell culture on an MEA substrate requires protocols to be adapted

to promote cell adhesion and viability on a variety of inorganic and organic insulating materials (Leung et al. 2008). An MEA featuring an insulating layer made of polystyrene has been fabricated by utilizing semiconductor processing technologies,. Because polystyrene is an inexpensive material and spin-casting is a relatively inexpensive deposition method, manufacture of this type of MEA can be scaled in a cost-efficient manner.

Previous work has demonstrated that polystyrene is a material that is compatible with microfluidics useful for cell culture, but the fabrication methods presented in prior work have not been readily applied to MEA technology. Previous efforts have relied on polystyrene parts fabricated by a variety of methods, including micromachining, injection molding, and soft lithography techniques (Chin et al. 2011; Mair et al. 2006; Young et al. 2011). While these methods effectively fabricate high aspect ratio microfluidic features, most of these polystyrene parts are intended to be stand-alone components. These techniques could potentially be used to create a microfluidic polystyrene part that would then be bonded to the MEA. However, bonding methods that have been utilized in polystyrene microfluidic fabrication, such as heat- or solvent-assisted bonding, risk deforming the microscale features of the film or contaminating a cell culture with leaching of residual solvent (Tsao and DeVoe 2009). Depositing the polystyrene film and patterning it directly on the surface of the MEA eliminates the need for a bonding method.

Future work will investigate deposition and patterning thicker films, ranging from a few microns to 10's of microns thick, to fabricate three dimensional microstructures directly on the surface of the MEA. These thicker films will enable a multi-well MEA or allow etching of reservoirs and flow channels with the MEA surface. While this has been accomplished using soft

polymeric materials, such as polydimethylsiloxane or agarose (Kang et al. 2009; Langhammer et al. 2013), these materials suffer from a number of drawbacks including deformation, permeability to water and media reagents, and hydrophobic recovery which impedes surface modification protocols for cell attachment (Berthier et al. 2012). Establishing processes to fabricate microfluidic structures from polystyrene, would eliminate the risks associated with these materials.

6.5 Acknowledgements

The authors acknowledge support from NSF PFI grant number IIP-1114211 (PI: BE Gnade). The authors would also like to thank the staff of the University of Texas at Dallas clean room for many helpful processing suggestions.

CHAPTER 7

CONCLUSIONS AND RECOMMENDATIONS FOR FUTURE WORK

The goal of this dissertation was to demonstrate the fabrication of two different types of MEAs with novel functionality. The dissertation presented a proof of concept integrated substrate with MEA electrodes for *in vitro* neural recordings and OLEDs, driven by TFTs for optical stimulation. The dissertation also presented an MEA encapsulated with a patterned polystyrene film. The broad approach of this research was to develop a process flow that results in the fabrication of the integrated multifunctional substrate, and to develop processes for spin-casting, curing, and etching the polystyrene encapsulating film.

7.1 Conclusions

As stated in Chapter 1, there are two main goals of this dissertation. One goal is to fabricate an MEA with substrate-integrated backside OLEDs driven by TFTs. This substrate is intended for application in an *in vitro* optogenetics experiment, wherein the OLEDs stimulate a plated culture of neurons that are susceptible to optical stimulation and the MEA records electrical activity from the plated tissues. This substrate is intended to streamline current work in the field of optogenetics, as several pieces of hardware would be integrated on this substrate. Chapters 2, 3, and 4 focus on the fabrication and preliminary lifetime studies of the MEA, OLED, and TFT components, and Chapter 5 discusses the process flow developed to integrate the components on a glass substrate. Another goal of this work is to utilize polystyrene as an encapsulation material for an *in vitro* MEA. While various types of MEA are available in both academic and commercial settings, the fabrication of these devices uses a vast set of organic and inorganic

materials to insulate the recording electrodes. These materials are difficult to prepare for cell culture and suffer from a number of disadvantages in *in vitro* MEA cell culture work. Macroscopic *in vitro* cell culture work has made use of polystyrene as a material for disposable culturing apparatuses for the past 50 years. This material is chemically inert, mechanically robust, optically transparent, and easily prepared to promote adhesion of plated tissues. Chapter 6 discusses the fabrication of a polystyrene-encapsulated MEA, assesses the electrochemical stability of this insulating film, and evaluates the performance of the substrate in *in vitro* neuronal recordings.

Chapter 2 presents the fabrication of an MEA on a polystyrene substrate, encapsulated with parylene. The goal of this chapter was to demonstrate that an MEA, based on chromium/gold electrodes with parylene insulation, could be fabricated in-house at UT Dallas. The electrodes and insulation are electrochemically stable during handling that is typical of *in vitro* cell culture, and recordings from the UT Dallas MEAs are comparable to commercially available substrates in terms of yield of active electrodes and signal-to-noise ratio. The MEA demonstrated in this chapter will be implemented in the integrated substrate.

Chapter 3 shows the fabrication of green and blue OLEDs. The OLED stack for the green device consists of a NPB hole transport layer and an Alq3 emissive layer. The peak output wavelength of this device is 530 nm, which is appropriate for optically stimulating the bacteriorhodopsin protein. The 10 mm^2 test pixel is turned on at 3.5 V and driven to a threshold brightness of 100 cd/m^2 with a driving current of 1.1 mA. The OLED stack for the blue device is composed of a MoO_3 hole transport layer, a TAPC hole transport layer, and an emissive layer that consists of mCP doped with FIrpic. This device has a peak wavelength output of 470 nm,

which would stimulate the ChR2 protein. The 10 mm^2 test pixel is turned on at 4 V, and is driven with a 0.4 mA current. Scaling this device down to 100 μm^2, the area of the OLED on the proposed integrated substrate, will require 0.4 μA of driving current. A preliminary lifetime test was performed on the blue OLED to assess the performance of a glass coverslip and UV-curable epoxy as an encapsulation system to prolong the lifetime of the device. The brightness of the device under constant operation is stable for the first hour of the test, which suggests that the lifetime of the device may be appropriate for the duration of an optogenetics experiment

Chapter 4 focuses on the fabrication of a TFT that is capable of driving the OLED presented in Chapter 3. The TFT is based on a HfO_2 gate dielectric deposited by ALD, a sputtered IGZO active layer, and parylene deposited by chemical vapor deposition. The device is able to deliver driving currents of 0.4 μA and 1.1 μA that turn on both the blue and green OLEDs, respectively, presented in chapter 3. Preliminary lifetime test of the device shows that the TFT is stable enough. While this device is used to demonstrate proof of concept of the integrated substrate, the instability shows that work integrating passivation and encapsulation steps into TFT fabrication should be performed.

Chapter 5 discusses the process flow developed for the multifunctional substrate. Material tolerances for handling were guiding principles in the design of the process flow. The MEA is fabricated first on the frontside of the substrate, as it is made from robust materials that are compatible with later processing steps. Then the TFT is fabricated on the backside of the substrate. The OLED is fabricated last, as the organic semiconductor material is most sensitive to oxygen and moisture. An integrated substrate was demonstrated. It was not possible to produce enough functional substrates for use in an *in vitro* experiment.

Chapter 6 presents polystyrene as an alternative material for MEA electrode encapsulation. A 500 nm thick polystyrene film is spin-cast from a solution of polystyrene dissolved in toluene. Protecting the polystyrene with an SiO_2 hardmask, enables patterning and etching of the polystyrene film to form electrode areas and bond pads. The insulation and electrodes are electrochemically stable over 30 days in typical cell culture conditions. Viable cell culture on the MEA is demonstrated. The substrates have a signal-to-noise ratio of 11.6 ± 0.5 and demonstrate percentage yields of active electrodes of 49.2 ± 4.6 %, which is comparable to both commercially available devices and the novel polymer-based MEA presented in Chapter 1.

In summary, the work presented in this dissertation establishes a proof of concept and developed a process flow for a substrate-integrated, multifunctional MEA, and demonstrates the fabrication, characterization, and application of an MEA substrate with patterned polystyrene encapsulation.

7.2 Future Work

Based on the work presented in this dissertation, the multifunctional MEA and the polystyrene-encapsulated MEA are promising devices for *in vitro* recordings from electrically active tissues. However, more work is required to advance the multifunctional substrate beyond the proof of concept stage. Additional work on depositing and patterning thicker polystyrene films is needed to realize the fabrication of microfluidic structures on the MEA surface.

1. **Device Stability**: in Chapters 3 and 4, fabrication of the OLED and the TFT, respectively, was demonstrated. Both devices were tested for a short degree of lifetime and stability, but more testing is required in order to fully assess the lifetime of these devices for the intended application. Both devices should be tested in pulsed operation modes, since this is the

most likely mode of operation in an *in vitro* optogenetics stimulation experiment. Additional stability tests that address the lifetime of the device while stored in cell culture conditions should be performed in order to assess device tolerance for handling and conditions associated with *in vitro* application. Results of this particular lifetime test will assess the robustness of OLED encapsulation and TFT passivation.

2. **Device integration, integrated substrate characterization and application**: As mentioned in Chapter 5, the integration of the MEA, TFT, and OLED proved to be a major challenge. Functional discrete OLED and TFT components are promising, but future work must increase the manufacturability of fully functioning substrates. For the integrated functionality, the substrate must be tested for lifetime stability, both on the shelf and in a cell culture incubator. Demonstrating MEA electrode electrochemical stability after TFT and OLED fabrication is crucial, as well as demonstrating that the TFT and OLED are robust enough to withstand typical handing during *in vitro* cell culture work. Fabrication of at least 6-12 fully-functional substrates will be required in order to get statistically meaningful data in an *in vitro* stimulation and recording experiment.

3. **Advancing polystyrene-encapsulated MEA technology**: The original intent of evaluating polystyrene as an insulating material was to move toward an MEA design with microfluidic features fabricated from a material that is more familiar to *in vitro* cell culture. Chapter 6 demonstrates that a polystyrene film cast from solution can be patterned using photolithography, and the film is robust electrode insulation. Advancements will devise methods to deposit and pattern thicker polystyrene films in order to fabricate microfluidic structures directly on the MEA.

APPENDIX A

UTD TRAVELER FOR MEA FABRICATION ON POLYCARBONATE SUBSTRATES

- Step 1: Substrate Preparation

1. Cut polycarbonate sheet into 24” x 14” sheet. Do not peel off protective film. NOTES:_____
2. Cut polycarbonate sheet using CO_2 raster laser. Laser is set to 20% power, 20% speed, and 2 passes. NOTES: _____
3. Remove protective film. NOTES: _____
4. Clean substrates by sonication in dilute aqueous Alconox solution, followed by IPA and DI water. NOTES: _____
5. Dry with N_2 and bake at 85° C for 10 minutes. NOTES: _____

GENERAL NOTES:

- Step 2: Metal Deposition and Patterning

1. Deposit 100 Å chromium and 3000 Å gold using CHA. NOTES: _____
2. Spin coat with S1815 at 2000 rpm, 3000 rpm/s for 60s. NOTES: _____
3. Soft bake 85° C for 10 minutes. NOTES: _____
4. Expose with metal mask with dosage of 150 mJ/cm^2. NOTES: _____
5. Develop pattern in MF-319 for 50s in base hood. NOTES: _____
6. Check resist pattern under microscope. Do not continue patterning on substrates with comets/defects in resist pattern. NOTES: _____
7. Etch metals in acid hood. Use gold etchant with 1:4 dilution (etch rate 12.5Å/s). Use chromium etchant undiluted (etch rate 20 Å/s) NOTES: _____
8. Blanket exposure in Karl Suss for 60s. NOTES: _____
9. Develop in MF-319 for 50s. Rinse, dry, and bake at 85° C for 10 minutes. NOTES: _____
10. Descum with O_2 RIE, 50W, 100 mT for 60 s. NOTES: _____
11. Check metal pattern under microscope. Do not continue fabrication on substrates with comets/defects in electrode pattern. NOTES: _____

GENERAL NOTES:

- Step 3: Parylene Deposition and Patterning

1. Deposit 500nm of parylene using 900 mg of parylene-C dimer. Run Si pilot chip along with substrates. NOTES:_____

2. Spin on S1813 2000 rpm at 3000 rpm/s for 60 s. NOTES: _____
3. Bake at 85° C for 10 min. NOTES: _____
4. Align and expose using a dose of 150 mJ/cm^2, using parylene mask. NOTES:_____
5. Develop pattern in MF-319 for 50s in base hood. NOTES: _____
6. Check resist pattern under microscope. Do not continue patterning on substrates with comets/defects in resist pattern. NOTES: _____
7. Determine O_2 RIE etch rate on Si pilot to estimate etch time for MEA substrates. Use 50W, 100 mT. Etch rate anticipated to be approximately 1 nm/s NOTES: _____
8. Blanket exposure in Karl Suss for 60s. NOTES: _____
9. Develop in MF-319 for 50s. Rinse, dry, and bake at 85° C for 10 minutes. NOTES: _____
10. Check parylene pattern under microscope. Do not continue fabrication on substrates with comets/defects in pattern. NOTES: _____
11. Descum with UV-ozone dry stripper with O_2 flow set to 0.7L/minute for 30 minutes. NOTES: _____

GENERAL NOTES:

- Step 4: Substrate completion and test

1. Attach polycarbonate cell culture ring with silicone adhesive. Mix adhesive components in a 1:1 ratio by weight. Allow adhesive to dry 15 minutes before testing. NOTES: _____
2. Test electrode impedance, using Plexon MEA holder, NanoZ. Cover electrode area with a few drops of 1x PBS. Test NOTES:_____
3. Remove PBS from electrode surface. Rinse with DI water and N_2 dry NOTES:_____

GENERAL NOTES:

APPENDIX B

UTD TRAVELER FOR GREEN OLEDS

- Step 1: Substrate Preparation

1. Obtain glass coupons with patterned ITO anode. Using multimeter and diamond-tipped scribe, denote the backside of the substrate, to prevent deposition on bare glass side of substrate NOTES:_____
2. Clean coupons, ITO side up, in cleanroom. Sonicate substrates in acetone, IPA, and H_2O for 5 minutes each, in solvent hood. NOTES: _____
3. N_2 dry. Bake for 1 minute at 115°C. NOTES: _____

GENERAL NOTES:

- Step 2: Semiconductor Deposition

1. In 4th floor lab, use bench-top UV light and power source to expose ITO side of coupons to UV/O_3 cleaning for 5 minutes. NOTES: _____
2. Vent Cooke system. Verify deposition monitor crystal lifetime >80%, and change crystal as needed. Check logbook for configuration of materials in Knudsen cells, and add/remove materials as needed. Preferred configuration is as follows: NPB (cell 4), LiF (cell 3), Alq3 (cell 6). NOTES: _____
3. Load coupons onto sample holder, with circular semiconductor shadow mask, ITO side down. Load sample holder, and pump Cooke system down. Verify chiller is running. Verify rotation is turned on. System takes ~2hours to reach base vacuum at low 10^{-6} Torr pressure. NOTES: _____
4. Verify thickness monitor is set to deposition program 9 for semiconductor stack. NOTES: _____
5. Evaporate NPB. Deposit 70 nm. Thickness monitor reads 100 nm, according to material tooling factor. NOTES: _____
6. Evaporate Alq3. Deposit 40 nm. Thickness monitor reads 40 nm according to material tooling factor. NOTES: _____

GENERAL NOTES:

- Step 3: Aluminum cathode deposition

1. Verify all power to all cells is off, turn off sample rotation, and allow deposition chamber to cool to <50°C. NOTES:_____

2. Vent Cooke system. Remove substrate holder from chamber. Switch shadow masks to L-shaped cathode mask. Verify coupons are still ITO side down. Return substrate holder to chamber NOTES: _____

3. Prepare external source for aluminum deposition. Remove previous tungsten filament from bracket and replace with new filament. Load aluminum wire on loops of filament. Wire should be cut into 1.5-inch strips. Wire is folded in half, then in half again to make a V-shape. Hang one wire piece on all filament loops, two wire pieces on the inner 4 loops, and three wire pieces on the two central loops. Carefully place bracket in center of chamber. Cover all Knudsen cells (EXCEPT for cell 3) with foil to prevent contamination. NOTES: _____

4. Pump down Cooke system to base vacuum. Verify substrate rotation is on. NOTES:_____

5. Verify thickness monitor is set to program 12 for LiF. Evaporate LiF. Deposit 8-10 Å of material. NOTES: _____

6. Sublimate aluminum. Verify thickness monitor is set to program 20 for metal deposition. Turn on power to external source. Verify source 3 is selected. Set initial sublimation current to 30 A, and start deposition. Allow external power source to run for one minute. After 1 minute, ramp up power at a rate of 0.5 A/min until 32 A of power is reached. Open sample shutter and deposit aluminum. NOTES: _____

7. Tungsten filament may break, and prematurely end metal deposition. If this happens, power off external source, vent chamber, and repeat steps 3, 4, and 6. Total aluminum thickness should be 750-1000 Å thick. NOTES: _____

GENERAL NOTES:

- Step 4: Device encapsulation

1. Vent system and remove samples from sample holder. Transfer coupons to dry box NOTES: _____

2. Apply a thin bead of UV-curable epoxy to outer perimeter of glass microscope slide. Glue glass slide to ITO side of coupon to encapsulate devices. Be careful to not allow glue to touch device area. NOTES:_____

3. Cure glue with long wavelength of hand-held UV lamp for a minimum of 20 minute, before removing substrate from glove box. NOTES:_____

GENERAL NOTES:

APPENDIX C

UTD TRAVELER FOR BLUE OLEDS

- Step 1: Substrate Preparation

4. Obtain glass coupons with patterned ITO anode. Using multimeter and diamond-tipped scribe, denote the backside of the substrate, to prevent deposition on bare glass side of substrate NOTES:_____
5. Clean coupons, ITO side up, in cleanroom. Sonicate substrates in acetone, IPA, and H_2O for 5 minutes each, in solvent hood. NOTES: _____
6. N_2 dry. Bake for 1 minute at 115°C. NOTES: _____

GENERAL NOTES:

- Step 2: Semiconductor Deposition

7. In 4th floor lab, use bench-top UV light and power source to expose ITO side of coupons to UV/O_3 cleaning for 5 minutes. NOTES: _____
8. Vent Cooke system. Verify deposition monitor crystal lifetime >80%, and change crystal as needed. Check logbook for configuration of materials in Knudsen cells, and add/remove materials as needed. Preferred configuration is as follows: MCP (cell 2), LiF (cell 3), TAPC (cell 4), TPBi (cell 5), FIrpic (cell 6), and MoO_3 (cell 8). NOTES: _____
9. Load coupons onto sample holder, with circular semiconductor shadow mask, ITO side down. Load sample holder, and pump Cooke system down. Verify chiller is running. Verify rotation is turned on. System takes ~2hours to reach base vacuum at low 10^{-6} Torr pressure. NOTES: _____
10. Verify thickness monitor is set to deposition program 9 for semiconductor stack. NOTES: _____
11. Evaporate MoO_3. Deposit 20 nm. Thickness monitor reads 76nm, according to material tooling factor. NOTES: _____
12. Evaporate TAPC. Deposit 40 nm. Thickness monitor reads 66.6 nm according to material tooling factor. NOTES: _____
13. Co-deposit FIrpic and MCP in 1:10 ratio. Begin ramping up power to evaporate FIrpic at low rate (~0.1 Å/s). When FIrpic rate is stable, ramp up power to evaporate MCP at higher rate (~1 Å/s). When both rates are stable at a ratio of 1:10, open sample shutter and deposit 30 nm. Thickness monitor will read 30 nm as well. NOTES: _____
14. Evaporate TPBi. Deposit 30 nm. Thickness monitor will read 43 nm, according to material tooling factor. NOTES: _____

GENERAL NOTES:

• Step 3: Aluminum cathode deposition

1. Verify all power to all cells is off, turn off sample rotation, and allow deposition chamber to cool to <50°C. NOTES:_____
2. Vent Cooke system. Remove substrate holder from chamber. Switch shadow masks to L-shaped cathode mask. Verify coupons are still ITO side down. Return substrate holder to chamber NOTES: _____
3. Prepare external source for aluminum deposition. Remove previous tungsten filament from bracket and replace with new filament. Load aluminum wire on loops of filament. Wire should be cut into 1.5-inch strips. Wire is folded in half, then in half again to make a V-shape. Hang one wire piece on all filament loops, two wire pieces on the inner 4 loops, and three wire pieces on the two central loops. Carefully place bracket in center of chamber. Cover all Knudsen cells (EXCEPT for cell 3) with foil to prevent contamination. NOTES: _____
4. Pump down Cooke system to base vacuum. Verify substrate rotation is on. NOTES: _____
5. Verify thickness monitor is set to program 12 for LiF. Evaporate LiF. Deposit 8-10 Å of material. NOTES: _____
6. Sublimate aluminum. Verify thickness monitor is set to program 20 for metal deposition. Turn on power to external source. Verify source 3 is selected. Set initial sublimation current to 30 A, and start deposition. Allow external power source to run for one minute. After 1 minute, ramp up power at a rate of 0.5 A/min until 32 A of power is reached. Open sample shutter and deposit aluminum. NOTES: _____
7. Tungsten filament may break, and prematurely end metal deposition. If this happens, power off external source, vent chamber, and repeat steps 3, 4, and 6. Total aluminum thickness should be 750-1000 Å thick. NOTES: _____

GENERAL NOTES:

• Step 4: Device encapsulation

1. Vent system and remove samples from sample holder. Transfer coupons to dry box NOTES: _____
2. Apply a thin bead of UV-curable epoxy to outer perimeter of glass microscope slide. Glue glass slide to ITO side of coupon to encapsulate devices. Be careful to not allow glue to touch device area. NOTES:_____
3. Cure glue with long wavelength of hand-held UV lamp for a minimum of 20 minute, before removing substrate from glove box. NOTES:_____

GENERAL NOTES:

APPENDIX D

UTD TRAVELER FOR IGZO TFT FABRICATION

- Step 1: Gate Metal Patterning

1. Obtain glass/ITO substrate. Using multimeter and diamond-tipped scribe, denote the backside of the substrate, to prevent processing on bare glass side of substrate NOTES:_____
2. Clean substrate, ITO side up, in cleanroom. Sonicate substrate in acetone, IPA, and H_2O for 5 minutes each, in solvent hood. NOTES: _____
3. N_2 dry. Bake for 1 minute at 115°C. NOTES: _____
4. Cover the ITO surface with photoresist S1813. NOTES:_____
5. Spin at 2000 rpm with 3000 acceleration for 60 seconds. NOTES:_____
6. Bake at 115 °C for 1 min. NOTES:_____
7. Expose resist using a dose of 150 mJ/cm^2 using the gate metal mask. NOTES: _____
8. Develop in MF-319 for 60 seconds. NOTES: _____
9. N_2 dry and bake at 115 °C for 1 min. NOTES: _____
10. Etch metal with concentrated HCl and rinse with water. For ITO substrates, time is 10.5 minutes. Check for complete etch using multimeter and microscope NOTES: _____
11. Strip the photoresist with acetone, IPA and water. RIE descum after cleaning for 1 minute (140 mTorr O_2/50 W). NOTES:_____

GENERAL NOTES:

- Step 2: Dielectric, Semiconductor and Hard-Mask Deposition

1. Blow the wafer with N_2 gas before placing it in the ALD chamber. NOTES:_____
2. Set the conditions for HfO_2 deposition at 100 °C. One cycle for this deposition is as follows: 0.5s pulse of tetrakis(dimethylamido)hafnium(IV), 20 s purge, 0.03 s pulse of H_2O, followed by a 20 s pulse. The deposition rate is 7.3 cycles/nm. NOTES: _____
3. Deposit semiconductor film. NOTES: IGZO by AJA Orion. Presputter for 5 minutes at 50 mT at 1% O_2 with a power of 50 W. At minute 5, ramp pressure down to 4 mT, and allow pressure to equilibrate before opening shutter. Deposition rate is approximately 1nm/min. Deposit 30nm. NOTES:_____
4. Deposit 500 nm parylene using 900 mg of dimer and standard deposition process.

GENERAL NOTES:

- Step 3: Semiconductor and Hard-Mask Patterning

1. Cover the surface with photoresist S1813. NOTES: _____
2. Spin at 2000 rpm with 3000 acceleration for 60 seconds. NOTES: _____
3. Bake at 115 °C for 2 minutes. NOTES: _____
4. Align and expose using a dose of 150 mJ/cm^2, using the semiconductor mask. NOTES: _____
5. Develop in MF-319 for 60 seconds and N_2 dry. NOTES: _____
6. Etch Parylene hard mask using RIE O_2 140 mT, 50 W, 11 minutes. NOTES: _____
7. Etch semiconductor using HCl 1:1000 for 10 seconds. Rinse with water and N_2 dry. NOTES: _____
8. Strip photoresist with acetone, IPA and water (no sonication). NOTES: _____
9. Bake for 2 minutes at 115 °C. NOTES: _____

GENERAL NOTES:

- Step 4: Gate Dielectric Patterning

1. Cover the surface with photoresist S1813. NOTES: _____
2. Spin at 2000 rpm at 3000 rpm/s acceleration for 60 seconds. NOTES: _____
3. Bake at 115 °C for 5 minutes. NOTES: _____
4. Align and expose using a dose of 150 mJ/cm^2, use the gate dielectric mask for HfO_2. NOTES:_____
5. Develop in MF-319 for 60 seconds. NOTES:_____
6. Etch HfO_2 with BOE 7:1 acid for 10 minutes. Rinse with water and N_2 dry. NOTES:_____
7. Strip the photoresist with acetone, IPA and water (no sonication). NOTES:_____
8. Bake for 2 minutes at 115 °C. NOTES: _____

GENERAL NOTES:

- Step 5: Hard-Mask vias patterning and Metal Deposition

1. Cover the surface with photoresist S1813. NOTES: _____
2. Spin at 2000 rpm with 3000 acceleration for 60 seconds. NOTES: _____
3. Bake at 115 °C for 2 minutes. NOTES: _____
4. Align and expose using a dose of 150 mJ/cm^2 using vias mask. NOTES: _____
5. Develop in MF-319 for 60 seconds. NOTES: _____
6. RIE etch parylene O_2 140 mT, 50 W, 11 minutes. . NOTES: _____
7. Strip the photoresist with acetone, IPA and water (no sonication). NOTES: _____
8. Bake for 2 minutes at 115 °C. NOTES: _____
9. Metal deposition for source/drain contacts. Deposit aluminum by AJA 1500 using 100W for 45 minutes in Ar atmosphere at 4mT. NOTES: _____

GENERAL NOTES:

- Step 6: Source-Drain Patterning

1. Cover the surface with photoresist S1813. NOTES: _____
2. Spin at 2000 rpm with 3000 acceleration for 60 seconds. NOTES: _____
3. Bake at 115 °C for 2 minutes. NOTES: _____
4. Align and expose using a dose of 150 mJ/cm^2 using S-D mask. NOTES: _____
5. Develop in MF-319 for 55 seconds. NOTES: _____
6. Etch Al with phosphoric acid heated to 85 °C. NOTES: _____
7. Strip the photoresist with acetone, IPA and water. NOTES: _____

GENERAL NOTES:

APPENDIX E

UTD TRAVELER FOR FABRICATION OF MULTIFUNCTIONAL MEA/OLED/TFT SUBSTRATE

- Chromium/gold MEA electrode deposition, patterning, and encapsulation

1. Obtain glass/ITO substrate. Using multimeter and diamond-tipped scribe, denote the bare side of the substrate, to prevent processing on the wrong side of substrate NOTES: _____
2. Clean substrate, ITO side up, in cleanroom. Sonicate substrate in acetone, IPA, and H_2O for 5 minutes each, in solvent hood. NOTES: _____
3. N_2 dry. Bake for 1 minute at 115°C. NOTES: _____
4. Cover the ITO surface with photoresist nLOF2020. NOTES: _____
5. Spin at 3000 rpm with 3000 acceleration for 60 seconds. NOTES: _____
6. Bake at 115 °C for 1 min. NOTES: _____
7. Blanket expose resist for 2 minutes, using a contact printer with no mask. NOTES: _____
8. Load substrate in CHA, bare side up, for e-beam deposition. NOTES: _____
9. Deposit 100 Å chromium and 3000 Å gold. NOTES: _____
10. Cover the gold surface with photoresist S1813. NOTES: _____
11. Spin at 2000 rpm with 3000 acceleration for 60 seconds. NOTES: _____
12. Bake at 115 °C for 1 minute. NOTES: _____
13. Expose using a dose of 150 mJ/cm^2 using MEA metal mask. NOTES: _____
14. Develop in MF-319 for 55 seconds. NOTES: _____
15. N_2 dry and bake at 115 °C for 1 minute. NOTES: _____
16. Etch metals in acid hood. Use gold etchant with 1:4 dilution (etch rate 12.5Å/s). Use chromium etchant undiluted (etch rate 20 Å/s) NOTES: _____
17. Strip the photoresist with acetone, IPA and water, making sure to clean resist from both sides of substrate. NOTES: _____
18. RIE descum Cr/Au electrodes for 1 minute (140 mTorr O_2/50 W). NOTES: _____
19. Cover ITO side of substrate completely with Kapton tape to prevent parylene deposition on this side of the substrate. NOTES: _____
20. Deposit 500nm of parylene on Cr/Au side of substrate, using 900 mg of parylene dimer and standard parylene deposition process. NOTES: _____

- Patterning ITO features and fabricating TFTs
- Gate metal patterning
    1. Remove Kapton tape from ITO side of substrate. Rinse substrate, ITO side up, in

acetone, IPA, and water. N2 dry. NOTES: _____

2. Cover the ITO surface with photoresist S1813. NOTES: _____
3. Spin at 2000 rpm with 3000 acceleration for 60 seconds. NOTES: _____
4. Bake at 115 °C for 1 minute. NOTES: _____
5. Align and expose using a dose of 150 mJ/cm^2 using OLED/MEA metal mask. NOTES: _____
6. Develop in MF-319 for 55 seconds. NOTES: _____
7. N_2 dry and bake at 115 °C for 1 min. NOTES: _____
8. Etch metal with concentrated HCl and rinse with water. For ITO substrates, time is 10.5 minutes. Check for complete etch using multimeter and microscope NOTES: _____
9. Strip the photoresist with acetone, IPA and water. N_2 dry. NOTES: _____
10. RIE descum after cleaning for 1 minute (140 mTorr O_2/50 W). NOTES: _____

- Blanket deposition of gate dielectric, active layer, and parylene films

1. Blow the wafer with N_2 gas before placing it in the ALD chamber. NOTES: _____
2. Set the conditions for HfO_2 deposition. Deposition is for 15nm HfO_2 at 100 °C. NOTES: _____
3. Deposit semiconductor film IGZO by AJA Orion. Deposition is at 4 mT in 20 sccm flow of 1% O_2, with a power of 50 W. Deposition rate is approximately 1 nm/min. Deposit 30nm. NOTES: _____
4. Tape substrate to carrier wafer, MEA side down. Tape seals all edges to carrier wafer to prevent additional parylene deposition on MEA. NOTES: _____
5. Deposit 500 nm parylene hard mask, using 900 mg of dimer and standard deposition process. NOTES: _____

- Patterning gate dielectric, active layer, and parylene layers

1. Cover the TFT/OLED parylene surface with S1813 photoresist. NOTES: _____
2. Spin resist at 2000 rpm with 3000 acceleration for 60 s. NOTES: _____
3. Bake at 115 °C for 1 min. NOTES: _____
4. Align and expose using a dose of 150 mJ/cm^2 using parylene mask. NOTES: _____
5. Develop in MF-319 for 55 seconds. NOTES: _____
6. N_2 dry and bake at 115 °C for 1 minute. NOTES: _____
7. RIE etch parylene in oxygen with 140 mT O_2 and 100W. Etch rate is approximately 55 nm/minute. NOTES: _____
8. Strip the photoresist with acetone, IPA and water. NOTES: _____
9. N_2 dry and bake at 115 °C for 1 minute. NOTES: _____
10. Cover the TFT/OLED parylene surface with S1813 photoresist. NOTES:

_____

11. Spin resist at 2000 rpm with 3000 acceleration for 60 s. NOTES: _____
12. Bake at 115 °C for 1 min. NOTES: _____
13. Align and expose using 150 mJ/cm^2 dose and parylene mask. NOTES: _____
14. Develop in MF-319 for 55 seconds. NOTES: _____
15. N_2 dry and bake at 115 °C for 1 minute. NOTES: _____
16. Etch IGZO in acid hood, with Hall diluted to 1:1000 in water. Etch rate is approximately 3 nm/s. After etch, N_2 dry substrate. NOTES: _____
17. Strip the photoresist with acetone, IPA and water. NOTES: _____
18. N_2 dry and bake at 115 °C for 1 minute. NOTES: _____
19. Cover the TFT/OLED parylene surface with S1813 photoresist. NOTES: _____
20. Spin resist at 2000 rpm with 3000 acceleration for 60 s. NOTES: _____
21. Bake at 115 °C for 1 min. NOTES: _____
22. Align and expose using a dose of 150 mJ/cm^2 and gate dielectric mask. NOTES: _____
23. Develop in MF-319 for 55 seconds. NOTES: _____
24. N_2 dry and bake at 115 °C for 1 minute. NOTES: _____
25. Etch HfO_2 in acid hood, using BOE 7:1. Etch rate is approximately 1.5 nm/minute. After etch, N_2 dry substrate. NOTES: _____
26. Strip the photoresist with acetone, IPA and water. NOTES: _____
27. N_2 dry and bake at 115 °C for 1 minute. NOTES: _____
28. Cover the TFT/OLED parylene surface with S1813 photoresist. NOTES: _____
29. Spin resist at 2000 rpm with 3000 acceleration for 60 s. NOTES: _____
30. Bake at 115 °C for 1 min. NOTES: _____
31. Align and expose using a dose of 150 mJ/cm^2 and vias mask. NOTES: _____
32. Develop in MF-319 for 55 seconds. NOTES: _____
33. N_2 dry and bake at 115 °C for 1 minute. NOTES: _____
34. RIE etch parylene in oxygen with 140 mT O_2 and 100W. Etch rate is approximately 55 nm/minute. NOTES: _____
35. Strip the photoresist with acetone, IPA and water. NOTES: _____
36. N_2 dry and bake at 115 °C for 1 minute. NOTES: _____

- Source-Drain deposition and patterning

1. Metal deposition for source/drain contacts on TFT/OLED side of substrate. Deposit aluminum by AJA 1500 using 100W for 45 minutes in Ar atmosphere at 4mT. NOTES: _____
2. Cover aluminum surface with S1813 photoresist. NOTES: _____
3. Spin resist at 2000 rpm with 3000 acceleration for 60 s. NOTES: _____
4. Bake at 115 °C for 1 min. NOTES: _____

5. Align and expose using a dose of 150 mJ/cm^2 and source/drain mask. NOTES: _____
6. Develop in MF-319 for 55 seconds. NOTES: _____
7. N_2 dry and bake at 115 °C for 1 minute. NOTES: _____
8. Etch aluminum in acid hood with undiluted phosphoric acid heated to 85°C. NOTES: _____
9. Strip the photoresist with acetone, IPA and water. NOTES: _____
10. N_2 dry and bake at 115 °C for 1 minute. NOTES: _____

- Encapsulating TFTs and patterning parylene

1. Tape substrate to carrier wafer, MEA side down. Tape seals all edges to carrier wafer to prevent additional parylene deposition on MEA. NOTES: _____
2. Deposit 500 nm parylene hard mask, using 900 mg of dimer and standard deposition process. NOTES: _____
3. Cover the TFT/OLED parylene surface with S1813 photoresist. NOTES: _____
4. Spin resist at 2000 rpm with 3000 acceleration for 60 s. NOTES: _____
5. Bake at 115 °C for 1 min. NOTES: _____
6. Align and expose using a dose of 150 mJ/cm^2 and OLED parylene mask. NOTES: _____
7. Develop in MF-319 for 55 seconds. NOTES: _____
8. N_2 dry and bake at 115 °C for 1 minute. NOTES: _____
9. RIE etch parylene in oxygen with 140 mT O_2 and 100W. Etch rate is approximately 55 nm/minute. NOTES: _____
10. DO NOT IMMEDIATELY STRIP RESIST.
11. Flip substrate over, and cover the MEA parylene surface with S1813 photoresist. NOTES: _____
12. Spin resist at 2000 rpm with 3000 acceleration for 60 s. NOTES: _____
13. Bake at 115 °C for 1 min. NOTES: _____
14. Align and expose using a dose of 150 mJ/cm^2 and MEA parylene mask. NOTES: _____
15. Develop in MF-319 for 55 seconds. NOTES: _____
16. N_2 dry and bake at 115 °C for 1 minute. NOTES: _____
17. RIE etch parylene in oxygen with 140 mT O_2 and 100W. Etch rate is approximately 55 nm/minute. NOTES: _____
18. Strip the photoresist with acetone, IPA and water, ensuring that both sides of substrate are cleaned. Fabrication on MEA side of substrate is now complete. NOTES:_____

- Fabrication of OLEDs in Cooke System
- Organic material stack deposition

1. Vent Cooke system. Verify deposition monitor crystal lifetime >80%, and change crystal as needed. Check logbook for configuration of materials in Knudsen cells, and add/remove materials as needed. Preferred configuration is as follows: MCP (cell 2), LiF (cell 3), TAPC (cell 4), TPBi (cell 5), FIrpic (cell 6), and MoO_3 (cell 8). NOTES: _____
2. Tape substrate onto sample holder, with MEA side down. Carefully, tape the large OLED shadow mask to substrate. Verify that deposition areas lines up with test pixels and stimulation pixels. Load sample holder, and pump Cooke system down. Verify chiller is running. Verify rotation is turned on. System takes ~2hours to reach base vacuum at low 10^{-6} Torr pressure. NOTES: _____
3. Verify thickness monitor is set to deposition program 9 for semiconductor stack. NOTES: _____
4. Evaporate MoO_3. Deposit 20 nm. Thickness monitor reads 76nm, according to material tooling factor. NOTES: _____
5. Evaporate TAPC. Deposit 40 nm. Thickness monitor reads 66.6 nm according to material tooling factor. NOTES: _____
6. Co-deposit FIrpic and MCP in 1:10 ratio. Begin ramping up power to evaporate FIrpic at low rate (~0.1 Å/s). When FIrpic rate is stable, ramp up power to evaporate MCP at higher rate (~1 Å/s). When both rates are stable at a ratio of 1:10, open sample shutter and deposit 30 nm. Thickness monitor will read 30 nm as well. NOTES: _____
7. Evaporate TPBi. Deposit 30 nm. Thickness monitor will read 43 nm, according to material tooling factor. NOTES: _____

- Aluminum cathode deposition

1. Verify all power to all cells is off, turn off sample rotation, and allow deposition chamber to cool to <50°C. NOTES:_____
2. Vent Cooke system. There is no need to change shadow mask for the cathode deposition. NOTES: _____
3. Prepare external source for aluminum deposition. Remove previous tungsten filament from bracket and replace with new filament. Load aluminum wire on loops of filament. Wire should be cut into 1.5 inch strips. Wire is folded in half, then in half again to make a V-shape. Hang one wire piece on all filament loops, two wire pieces on the inner 4 loops, and three wire pieces on the two central loops. Carefully place bracket in center of chamber. Cover all Knudsen cells (EXCEPT for cell 3) with foil to prevent contamination. NOTES: _____
4. Pump down Cooke system to base vacuum. Verify substrate rotation is on. NOTES:_____
5. Verify thickness monitor is set to program 12 for LiF. Evaporate LiF. Deposit 8-10 Å of material. NOTES: _____
6. Sublimate aluminum. Verify thickness monitor is set to program 20 for metal deposition. Turn on power to external source. Verify source 3 is selected. Set initial sublimation current to 30 A, and start deposition. Allow external power

source to run for one minute. After 1 minute, ramp up power at a rate of 0.5 A/min until 32 A of power is reached. Open sample shutter and deposit aluminum. NOTES: _____

7. Tungsten filament may break, and prematurely end metal deposition. If this happens, power off external source, vent chamber, and repeat steps 3, 4, and 6. Total aluminum thickness should be 750-1000 Å thick. NOTES: _____

- Step 4: Device encapsulation

1. Vent system and remove shadow masks and substrate from sample holder. Transfer substrates to dry box NOTES: _____
2. Apply a thin bead of UV-curable epoxy to outer perimeter of a glass microscope slide. Glue glass slide to substrate to encapsulate OLED test structures. Glue two glass slides to substrate to encapsulate both arrays of OLED stimulating pixels. Be careful to not allow glue to touch any device area.
   NOTES:_____
3. Cure epoxy with long wavelength of handheld UV lamp for 20 minutes.
   NOTES:_____
4. Substrate fabrication is now complete. Using diamond-tipped scribe, the two multifunctional chips may be carefully broken away from the substrate.
   NOTES:_____

APPENDIX F

UTD TRAVELER FOR FABRICATION OF POLYSTYRENE ENCAPSULATED ITO MEA ON GLASS SUBSTRATE

- Patterning ITO electrodes and chromium alignment markers
    1. Begin with clean ITO/glass substrate. Using multimeter and diamond-tipped scribe, identify the bare side of glass to prevent processing on the wrong side of the substrate. NOTES:_____
    2. Clean substrate, ITO side up, in cleanroom. Sonicate substrate in acetone, IPA, and H_2O for 5 minutes each, in solvent hood. NOTES: _____
    3. N_2 dry and bake at 115 °C for 1 minute. NOTES:_____
    4. Cover ITO surface with S1813 photoresist. NOTES:_____
    5. Spin resist at 2000 rpm with 3000 acceleration for 60 s. NOTES:_____
    6. Align and expose using a dose of 150 mJ/cm^2 and MCS Version E Metal mask. NOTES:_____
    7. Develop in MF-319 for 55 seconds. NOTES:_____
    8. N_2 dry and bake at 115 °C for 1 minute. NOTES:_____
    9. Check resist pattern under microscope. Do not continue patterning on substrates with comets/defects in resist pattern. NOTES: _____
    10. Etch metal with concentrated HCl and rinse with water. For ITO substrates, time is 10.5 minutes. Check for complete etch using multimeter and microscope NOTES:_____
    11. Strip the photoresist with acetone, IPA and water. NOTES:_____
    12. N_2 dry and bake at 115 °C for 1 minute. NOTES:_____
    13. Descum ITO features using RIE, with 100 mT oxygen and 50 W for 1 minute. NOTES:_____
    14. Load substrate(s) in CHA for electron-beam evaporation of chromium. Tape substrates to 6” carrier wafers, being sure to not tape over the ITO alignment markers. Deposit 50 nm of chromium. NOTES:_____
    15. Cover the ITO surface with photoresist AZ nLOF2020. NOTES:_____
    16. Spin resist at 3000 rpm with 3000 acceleration for 60 s. NOTES:_____
    17. Bake at 115 °C for 1 min. NOTES:_____
    18. Obtain MCS Version E parylene mask. Using CPK spinner, use standard solvent clean recipe to clean mask. After cleaning, using Kapton tape, cover all features on the mask, except the alignment markers. NOTES:_____
    19. Align and expose using i-line radiation, a dose of 66 mJ/cm^2 and taped MEA parylene mask. NOTES:_____
    20. Post-exposure bake at 115 °C for 1 min. NOTES:_____
    21. Remove Kapton tape from mask. Using CPK spinner, use standard solvent clean recipe to clean adhesive residue from mask. NOTES:_____

22. Develop in AZ 300 MIF for 55 seconds. NOTES:_____
23. Etch metal with undiluted chromium etchant and rinse with water. Etch rate is approximately 0.8 nm/s. NOTES:_____
24. Strip the photoresist with acetone, IPA and water. NOTES:_____
25. Bake at 115 °C for 1 min. NOTES:_____
26. Descum metal features using RIE, with 100 mT oxygen and 50 W for 1 minute. NOTES:_____

- Polystyrene encapsulation and hard mask deposition

1. Prepare polystyrene solution. Mix 0.8 grams of polystyrene pellets with 20 mL of toluene in a 20 mL glass scintillation vial, for a final concentration of 0.04 g/mL. Heat to 65 °C while stirring for 2 hours. NOTES:_____
2. Prepare A-174 silane adhesion promoter solution in solvent hood in clean room. In a beaker, mix 100 mL of isopropyl alcohol with 100 mL of deionized water. To this beaker, add 1 mL of A-174 solution. Mix well and allow to stand for a minimum of 2 hours up to 24 hours. NOTES:_____
3. Coat patterned ITO substrates with A-174. Place 1-3 substrates in a glass petri dish, and pour in enough A-174 solution to cover substrate in 0.5 cm of liquid. Allow to soak in cleanroom solvent hood for 30 minutes. NOTES:_____
4. Pour off excess liquid into solvent waste sink, and allow substrates to air dry for 30 minutes. NOTES:_____
5. Rinse substrates for 30 s with fresh isopropyl alcohol, while gently agitating petri dish. Pour off rinse solution into solvent waste sink. N_2 dry substrate. NOTES:_____
6. Examine substrates under microscope, looking carefully for oily spots of excess A-174 residue. Spots of residue may be wiped away with a swab. Particles on surface should be blown away with N_2. NOTES:_____
7. Cover surface of MEA with polystyrene solution. Extrude solution through a 0.45 μm syringe filter to remove particulate matter from solution. Bubbles in solution on the surface of MEA should be removed with a clean plastic pipette. NOTES:_____
8. Spin resist at 500 rpm with 3000 acceleration for 10 s. NOTES:_____
9. Bake at 90 °C for 60 min. NOTES:_____
10. Transfer samples to quartz holder, and load into HMDS oven. Run the standard HMDS 20 minute adhesion process. NOTES:_____
11. Deposit 150 nm of SiO_2 hard mask film using PECVD and STDOX100 automated process. Process parameters are: 900 mT pressure, 50 W RF power, 900 sccm SiH_4, 400 sccm N_2O, and a deposition time of 15 minutes. NOTES:_____

- Encapsulation patterning and hard mask removal

1. Cover SiO_2 surface with S1813 photoresist. NOTES:_____

2. Spin resist at 2000 rpm with 3000 acceleration for 60 s. NOTES:_____
3. Bake at 65 °C for 60 min. NOTES:_____
4. Align and expose using a dose of 150 mJ/cm^2 and MEA parylene mask. NOTES:_____
5. Develop in MF-319 for 55 seconds. NOTES:_____
6. Bake at 65 °C for 15 min. NOTES:_____
7. Etch SiO_2 hardmask in acid hood, using BOE 7:1. Etch rate is approximately 10 nm/s. N_2 dry. NOTES:_____
8. Bake at 65 °C for 15 min. NOTES:_____
9. Etch polystyrene encapsulation with RIE, using 200 mT O_2, 200 W RF power. The polystyrene etch rate for this process is approximately 50 nm/minute. Completed polystyrene etch may be verified under microscope and by gently probing ITO bond pads with multimeter. NOTES:_____
10. Remove remaining photoresist with blanket UV exposure for 60 s. NOTES:_____
11. Develop in MF-319 for 55 seconds. NOTES:_____
12. Bake at 65 °C for 15 min. NOTES:_____
13. Remove SiO_2 hardmask in acid hood, using BOE 7:1. N_2 dry. NOTES:_____
14. Bake at 65 °C for 15 min. NOTES:_____

- Substrate completion and test

1. Attach polycarbonate cell culture ring with silicone adhesive. Mix adhesive components in a 1:1 ratio by weight. Allow adhesive to dry 15 minutes before testing. NOTES: _____
2. Test electrode impedance, using Plexon MEA holder and NanoZ. Cover electrode area with a few drops of 1x PBS. Press “activate electrode site” button to start test. NOTES:_____
3. Remove PBS from electrode surface. Rinse with DI water and N_2 dry NOTES:_____

REFERENCES

Adamovich VI, Cordero SR, Djurovich PI, Tamayo A, Thompson ME, D'Andrade BW, Forrest SR. 2003. New charge-carrier blocking materials for high efficiency OLEDs. Organic Electronics 4(2–3):77-87.

Adesnik H and Scanziani M. 2010. Lateral competition for cortical space by layer-specific horizontal circuits. Nature 464(7292):1155-60.

Aton SJ, Huettner JE, Straume M, Herzog ED. 2006. GABA and gi/o differentially control circadian rhythms and synchrony in clock neurons. Proc Natl Acad Sci U S A 103(50):19188-93.

Aziz H and Popovic ZD. 2004. Degradation phenomena in small-molecule organic light-emitting devices. Chem Mater 16(23):4522-32.

Aziz H, Popovic Z, Xie S, Hor A-, Hu N-, Tripp Cl, Xu G. 1998. Humidity-induced crystallization of tris (8-hydroxyquinoline) aluminum layers in organic light-emitting devices. Appl Phys Lett 72(7):756-8.

Bakkum DJ, Chao ZC, Potter SM, Ben-Jacob E. 2008. Long-term activity-dependent plasticity of action potential propagation delay and amplitude in cortical networks. PloS One 3(5):e2088.

Baldo MA, O'Brien DF, You Y, Shoustikov A, Sibley S, Thompson ME, Forrest SR. 1998. Highly efficient phosphorescent emission from organic electroluminescent devices. Nature 395(6698):151.

Bamann C, Kirsch T, Nagel G, Bamberg E. 2008. Spectral characteristics of the photocycle of channelrhodopsin-2 and its implication for channel function. Journal of Molecular Biology 375(3):686-94.

Bardeen J. 1947. Surface states and rectification at a metal semi-conductor contact. Phys Rev 71(10):717-27.

Bayliss SC, Buckberry LD, Fletcher I, Tobin MJ. 1999. The culture of neurons on silicon. Sensors and Actuators A: Physical 74(1):139-42.

Bennett TN, Paguio M, Gligoijevic B, Seudieu C, Kosar AD, Davidson E, Roepe PD. 2004. Novel, rapid, and inexpensive cell-based quantification of antimalarial drug efficacy. Antimicrobial Agents and Chemotherapy 48(5):1807.

Berthier E, Young EWK, Beebe D. 2012. Engineers are from PDMS-land, biologists are from polystyrenia. Lab Chip 12(7):1224-37.

Bockemuehl RR. 1960. Cadmium sulfide field effect phototransistor. Proceedings of the IRE 48(5):875-82.

Boyden ES. 2011. A history of optogenetics: The development of tools for controlling brain circuits with light. F1000 Biology Reports 3(11).

Boyden ES, Zhang F, Bamberg E, Nagel G, Deisseroth K. 2005. Millisecond-timescale, genetically targeted optical control of neural activity. Nat Neurosci 8(9):1263-8.

Bruegmann T, Malan D, Hesse M, Beiert T, Fuegemann CJ, Fleischmann BK, Sasse P. 2010. Optogenetic control of heart muscle in vitro and in vivo. Nature Methods 7(11):897-900.

Carey FA. 2007. Advanced organic chemistry. 5th ed.. ed. New York: New York : Springer.

Caspi O, Itzhaki I, Kehat I, Gepstein AA, G., Huber I, Satin J, Gepstein L. 2009. In vitro electrophysiological drug testing using human embryonic stem cell derived cardiomyocytes. Stem Cells and Development 18(1):161.

Caterina MJ, Schumacher MA, Tominaga M, Rosen TA, Levine JD, Julius D. 1997. The capsaicin receptor: A heat-activated ion channel in the pain pathway. Nature 389(6653):816-24.

Chang JC, Brewer GJ, Wheeler BC. 2000. Microelectrode array recordings of patterned hippocampal neurons for four weeks. Biomed Microdevices 2(4):245-53.

Charati SG and Stern SA. 1998. Diffusion of gases in silicone polymers: Molecular dynamics simulations. Macromolecules 31(16):5529-35.

Charkhkar H, Knaack GL, Gnade BE, Keefer EW, Pancrazio JJ. 2012. Development and demonstration of a disposable low-cost microelectrode array for cultured neuronal network recording. Sensors and Actuators B: Chemical 161(1):655-60.

Charkhkar H, Arreaga-Salas DE, Tran T, Hammack A, Voit WE, Pancrazio JJ, Gnade BE. 2016. Novel disposable microelectrode array for cultured neuronal network recording exhibiting equivalent performance to commercially available arrays. Sensors and Actuators B: Chemical 226:232-8. https://doi.org/10.1016/j.snb.2015.11.094

Charkhkar H, Meyyapan S, Mateeva E, Moll JR, McHail DG, Peixoto N, Cliff RO, Pancrazio JJ. 2015. Amyloid beta modulation of neuronal network activity in vitro. Brain Research 1629:1-9.

Charkhkar H, Frewin C, Nezfati M, Knaack GL, Peixoto N, Saddow SE, Pancrazio JJ. 2014. Use of cortical neuronal networks for in vitro material biocompatibility testing. Biosensors and Bioelectronics 53(15):316-23.

Chen WT, Lo SY, Kao SC, Zan HW, Tsai CC, Lin JH, Fang CH, Lee CC. 2011. Oxygen-dependent instability and annealing/passivation effects in amorphous In–Ga–Zn–O thin-film transistors. IEEE Electron Device Letters 32(11):1552-4.

Chiang CC, Ladas TP, Gonzalez-Reyes LE, Durand DM. 2014. Seizure suppression by high frequency optogenetic stimulation using In Vitro and In Vivo animal models of epilepsy. Brain Stimulation 7(6):890-9.

Chiappalone M, Massobrio P, Martinoia S. 2008. Network plasticity in cortical assemblies. European Journal of Neuroscience 28(1):221-37.

Chiappalone M, Vato A, Tedesco MB, Marcoli M, Davide F, Martinoia S. 2003. Networks of neurons coupled to microelectrode arrays: A neuronal sensory system for pharmacological applications. Biosensors & Bioelectronics 18(5):627-34.

Chihaya A, Shizuo T, Tetsuo T, Shogo S. 1988. Electroluminescence in organic films with three-layer structure. Japanese Journal of Applied Physics 27(2):L269.

Chin CD, Laksanasopin T, Cheung YK, Steinmiller D, Linder V, Parsa H, Wang J, Moore H, Rouse R, Umviligihozo G, et al. 2011. Microfluidics-based diagnostics of infectious diseases in the developing world. Nature Medicine 17(8):1015-9.

Chu TY, Chen JF, Chen SY, Chen CJ, Chen CH. 2006. Highly efficient and stable inverted bottom-emission organic light emitting devices. Appl Phys Lett 89(5):053503.

Colombi I, Mahajani S, Frega M, Gasparini L, Chiappalone M. 2013. Effects of antiepileptic drugs on hippocampal neurons coupled to micro-electrode arrays. Frontiers in Neuroengineering 6(10):1.

Connolly P, Clark P, Curtis ASG, Dow JAT, Wilkinson CDW. 1990. An extracellular microelectrode array for monitoring electrogenic cells in culture. Biosensors & Bioelectronics 5(3):223-34.

Correia APP. 2016. A second-order ΣΔ ADC using sputtered IGZO TFTs. 1st ed. 2016. Cham : Springer International Publishing : Imprint: Springer.

Cui HF, Ye JS, Chen Y, Chong SC, Sheu FS. 2006. Microelectrode array biochip: ATool for in vitro drug screening based on the detection of a drug effect on dopamine release from PC12 cells. Anal Chem 78(18):6347-55.

D'Andrade B and Forrest S . 2004. White organic light-emitting devices for solid-state lighting. Adv Mater 16(18):1585-95.

Deisseroth K, Feng G, Majewska AK, Miesenback G, Ting A, Schnitzer MJ. 2006. Next-generation optical technologies for illuminating genetically targeted brain circuits. Journal of Neuroscience 26(41):10380.

Del Bene F and Wyart C. 2012. Optogenetics: A new enlightenment age for zebrafish neurobiology. Developmental Neurobiology 72(3):404-14.

Duffy DC, McDonald JC, Schueller OJA, Whitesides GM. 1998. Rapid prototyping of microfluidic systems in poly(dimethylsiloxane).Anal Chem 70(23):4974.

Eddington DT, Puccinelli JP, Beebe DJ. 2006. Thermal aging and reduced hydrophobic recovery of polydimethylsiloxane. Sensors Actuators B: Chem 114(1):170-2.

Ellis-Davies G. 2012. A chemist and biologist talk to each other about caged neurotransmitters. Beilstein Journal of Organic Chemistry 9:64-73.

Flanagan LA, et al. 2002. Neurite branching on deformable substrates. Neuroreport 13(18):2411-5.

Forrest SR, et al. 1998. Highly efficient phosphorescent emission from organic electroluminescent devices. Nature 395(6698):151-4.

Gautier E, Lorin A, Nunzi J- , Schalchli A, Benattar J- , Vital D. 1996. Electrode interface effects on indium–tin–oxide polymer/metal light emitting diodes. Appl Phys Lett 69(8):1071-3.

Geffroy B, le Roy P, Prat C. 2006. Organic light-emitting diode (OLED) technology: Materials, devices and display technologies. Polym Int 55(6):572-82.

Gervais T, El-Ali J, Gunther A, Jensen KF. 2006. Flow-induced deformation of shallow microfluidic channels. Lab Chip 6(4):500-7.

Gewandter JS, Staversky RJ, O'Reilly MA. 2009. Hyperoxia augments ER-stress-induced cell death independent of BiP loss. Free Radical Biology and Medicine 47(12):1742-52.

Giovangrandi L, Gilchrist KH, Whittington RH, Kovacs GTA. 2006. Low-cost microelectrode array with integrated heater for extracellular recording of cardiomyocyte cultures using commercial flexible printed circuit technology. Sensors Actuators B: Chem 113(1):545-54.

Gireesh ED and Plenz D. 2008. Neuronal avalanches organize as nested theta- and beta/gamma-oscillations during development of cortical layer 2/3. Proc Natl Acad Sci U S A 105(21):7576-81.

Goldner JS, Bruder JM, Li G, Gazzola D, Hoffman-Kim D. 2006. Neurite bridging across micropatterned grooves. Biomaterials 27(3):460-72.

Goral VN, Hsieh YC, Petzold ON, Faris RA, Yuen PK. 2011. Hot embossing of plastic microfluidic devices using poly(dimethylsiloxane) molds. Journal of Micromechanics and Microengineering 21(1):017002.

Görrn P, Riedl T, Kowalsky W. 2009. Encapsulation of zinc tin oxide based thin film transistors. J Phys Chem C 113(25):11126-30.

Gramowski A, Jügelt K, Weiss DG, Gross GW. 2004. Substance identification by quantitative characterization of oscillatory activity in murine spinal cord networks on microelectrode arrays. Eur J Neurosci 19(10):2815-25.

Green RA, et al. 2012. Substrate dependent stability of conducting polymer coatings on medical electrodes. Biomaterials 33(25):5875-86.

Green R. A., Devillaine F., Dodds C., Matteucci P., Chen S., Byrnes-Preston P., Poole-Warren L. A., Lovell N. H. and Suaning G. J. 2010. Conducting polymer electrodes for visual prostheses. 2010 annual international conference of the IEEE engineering in medicine and biology. 6769 p.

Gross GW. 1979. Simultaneous single unit recording in vitro with a photoetched laser deinsulated gold multimicroelectrode surface. IEEE Transactions on Bio-Medical Engineering BME-26(5):273-9.

Gross GW, Wen WY, Lin JW. 1985. Transparent indium-tin oxide electrode patterns for extracellular, multisite recording in neuronal cultures. Journal of Neuroscience Methods 15(3):243-52.

Gross GW, Williams AN, Lucas JH. 1982. Recording of spontaneous activity with photoetched microelectrode surfaces from mouse spinal neurons in culture. J Neurosci Methods 5(1):13-22.

Gross GW, Rieske E, Kreutzberg GW, Meyer A. 1977. A new fixed-array multi-microelectrode system designed for long-term monitoring of extracellular single unit neuronal activity in vitro. Neurosci Lett 6(2):101-5.

Hales CM, Rolston JD, Potter SM. 2010. How to culture, record and stimulate neuronal networks on micro-electrode arrays (MEAs). Journal of Visualized Experiments (39):2056.

Halls MD, Tripp CP, Bernhard-Schlegel H. 2001. Structure and infrared (IR) assignments for the OLED material: N,N'-diphenyl-N,N'-bis(1-naphthyl)-1,1'-biphenyl-4,4"-diamine (NPB). Phys Chem Chem Phys 3(11):2131.

Hamilton F, Berry T, Peixoto N, Sauer T. 2013. Real-time tracking of neuronal network structure using data assimilation. Physical Review 88(5):052715.

Hämmerle H, Egert U, Mohr A, Nisch W. 1994. Extracellular recording in neuronal networks with substrate integrated microelectrode arrays. Biosensors & Bioelectronics 9(9):691-6.

Harrison RG. 1911. On the stereotropism of embryonic cells. Science 34(870):279-81.

Hasan FM and Berdichevsky Y. 2016. Neural circuits on a chip. Micromachines 7(9):1.

Hayashi R, Sato A, Ofuji M, Abe K, Yabuta H, Sano M, Kumomi H, Nomura K, Kamiya T, Hirano M, et al. 2008. 42.1: Invited paper: Improved amorphous in-ga-zn-O TFTs. Society for Information Display 08 Digest 39(1):621-4.

Heer F, Hafizovic S, Franks W, Blau A, Ziegler C, Hierlemann A. 2006. CMOS microelectrode array for bidirectional interaction with neuronal networks. IEEE Journal of Solid-State Circuits 41(7):1620-9.

Heer F, Franks W, Blau A, Taschini S, Ziegler C, Hierlemann A, Baltes H. 2004. CMOS microelectrode array for the monitoring of electrogenic cells. Biosensors & Bioelectronics 20(2):358-66.

Heil O, inventor; September 26, 1939. Improvements in or relating to electrical amplifiers and other control arrangements and devices. 439.357.

Helfrich W and Schneider WG. 1965. Recombination radiation in anthracene crystals. Phys Rev Lett 14(7):229-31.

Heo YS, Cabrera LM, Song JW, Futai N, Tung YC, Smith GD, Takayama S. 2007. Characterization and resolution of evaporation-mediated osmolality shifts that constrain microfluidic cell culture in poly(dimethylsiloxane) devices. Anal Chem 79(3):1126-34.

Hogan NC, Talei-Franzesi G, Abudayyeh O, Taberner A, Hunter I. 2012. Low-cost, flexible polymer arrays for long-term neuronal culture. Conf Proc IEEE Eng Med Biol Soc :803-6.

Hung LS and Chen CH. 2002. Recent progress of molecular organic electroluminescent materials and devices. Materials Science & Engineering 39(5):143-222.

Ide AN, Andruska A, Boehler M, Wheeler BC, Brewer GJ. 2010. Chronic network stimulation enhances evoked action potentials. Journal of Neural Engineering 7(1):016008.

Jeong JK, Won Yang H, Jeong JH, Mo YG, Kim HD. 2008. Origin of threshold voltage instability in indium-gallium-zinc oxide thin film transistors. Appl Phys Lett 93(12):123508.

Jimbo Y, Kawana A, Parodi P, Torre V. 2000. The dynamics of a neuronal culture of dissociated cortical neurons of neonatal rats. Biological Cybernetics 83(1):1-20.

Johnstone AFM, Gross GW, Weiss DG, Schroeder OHU, Gramowski A, Shafer TJ. 2010. Microelectrode arrays: A physiologically based neurotoxicity testing platform for the 21st century. Neurotoxicology 31(4):331-50.

Kalyani NT. 2017. Principles and applications of organic light emitting diodes (OLEDs). Duxford : Woodhead Publishing.

Kang DH, Kang I, Ryu SH, Jang J. 2011. Self-aligned coplanar a-IGZO TFTs and application to high-speed circuits. IEEE Electron Device Letters 32(10):1385-7.

Kang G, Lee J-, Lee C-, Nam Y. 2009. Agarose microwell based neuronal micro-circuit arrays on microelectrode arrays for high throughput drug testing. Lab Chip 9(22):3236.

Kasap SOS. 2018. Principles of electronic materials and devices. 4th ed. ed. New York, NY: McGraw-Hill.

Kawamura Y, Goushi K, Brooks J, Brown JJ, Sasabe H, Adachi C. 2005. 100% phosphorescence quantum efficiency of ir(III) complexes in organic semiconductor films. Applied Physics Letters 86(7):071104.

Keefer EW, Gramowski A, Stenger DA, Pancrazio JJ, Gross GW. 2001a. Characterization of acute neurotoxic effects of trimethylolpropane phosphate via neuronal network biosensors. Biosensors & Bioelectronics 16(7):513-25.

Keefer EW, Norton SJ, Boyle NAJ, Talesa V, Gross GW. 2001b. Acute toxicity screening of novel AChE inhibitors using neuronal networks on microelectrode arrays. Neurotoxicology 22(1):3-12.

Kim S, Bhandari R, Klein M, Negi S, Rieth L, Tathireddy P, Toepper M, Oppermann H, Solzbacher F. 2009. Integrated wireless neural interface based on the utah electrode array. Biomedical Microdevices 11(2):453-66.

Knaack GL, Charkhkar H, Hamilton FW, Peixoto N, O'Shaughnessy TJ, Pancrazio JJ. 2013. Differential responses to ω-agatoxin IVA in murine frontal cortex and spinal cord derived neuronal networks. Neurotoxicology 37:19-25.

Koshel RJ. 2013. Illumination engineering: Designing with non-imaging optics. Piscataway, NJ: IEEE Press.

Kulkarni AP, Tonzola CJ, Babel A, Jenekhe SA. 2004. Electron transport materials for organic light-emitting diodes. Chem Mater 16(23):4556-73.

Kumomi H, Nomura K, Kamiya T, Hosono H. 2008. Amorphous oxide channel TFTs. Thin Solid Films 516(7):1516-22.

Langhammer CG, Kutzing MK, Luo V, Zahn JD, Firestein B. 2013. A topographically modified substrate-embedded MEA for directed myotube formation at electrode contact sites . Ann Biomed Eng 41:408.

Lee JN, Park C, Whitesides GM. 2003. Solvent compatibility of poly(dimethylsiloxane)-based microfluidic devices. Anal Chem 75(23):6544-54.

Leung BK, Biran R, Underwood CJ, Tresco PA. 2008. Characterization of microglial attachment and cytokine release on biomaterials of differing surface chemistry. Biomaterials 29(23):3289-97.

Lien TL, Ban J, Tormen M, Migliorini E, Grenci G, Pozzato A, Torre V. 2013. Can hippocampal neurites and growth cones climb over obstacles? PLoS ONE 8(9):e73966.

Lilienfield EJ, inventor; 1930. Method and apparatus for controlling electric currents. 1745175.

Lima SQ and Miesenböck G. 2005. Remote control of behavior through genetically targeted photostimulation of neurons. Cell 121(1):141-52.

Lozier RH, Bogomolni RA, Stoeckenius W. 1975. Bacteriorhodopsin: A light-driven proton pump in halobacterium halobium. Biophysical Journal 15(9):955-62.

Mair DA, Geiger E, Pisano AP, Frechet JMJ, Svec F. 2006. Injection molded microfluidic chips featuring integrated interconnects. Lab Chip (10):1346-54.

Makishima A and Mackenzie JD. 1973. Direct calculation of young's moidulus of glass. Journal of Non-Crystalline Solids 12(1):35-45.

Mandal HS, Kastee JS, McHail DG, Rubinson JF, Pancrazio JJ, Dumas TC. 2015. Improved poly(3,4-ethylenedioxythiophene) (PEDOT) for neural stimulation. Neuromodulation 18(8):657-63.

Mandal HS, Knaack GL, Charkhkar H, McHail DG, Kastee JS, Dumas TC, Peixoto N, Rubinson JF, Pancrazio JJ. 2014. Improving the performance of poly(3,4-ethylenedioxythiophene) for brain–machine interface applications. Acta Biomaterialia 10(6):2446-54.

Manz A, Graber N, Widmer HM. 1990. Miniaturized total chemical analysis systems: A novel concept for chemical sensing. Sensors and Actuators B: Chemical 1(1):244-8.

Martinez A , Phillips S , Butte M , Whitesides G . 2007. Patterned paper as a platform for inexpensive, low-volume, portable bioassays. Agnew Chem in Ed Engl 46(8):1318-20.

Massobrio P, Pasquale V, Martinoia S. 2015. Self-organized criticality in cortical assemblies occurs in concurrent scale-free and small-world networks. Scientific Reports 5(1):10578.

Mastrototaro JJ, Massoud HZ, Pilkington TC, Ideker RE. 1992. Rigid and flexible thin-film multielectrode arrays for transmural cardiac recording. IEEE Transactions on Biomedical Engineering 39(3):271-9.

Matsunaga T, Fushiki A, Nose A, Kohsaka H. 2013. Optogenetic perturbation of neural activity with laser illumination in semi-intact drosophila larvae in motion. Journal of Visualized Experiments (77):50513.

Maybeck V, Schnitker J, Li W, Heuschkel M, Offenh A. 2016. An evaluation of extracellular MEA versus optogenetic stimulation of cortical neurons. Biomed Phys Eng Express 2(5):055017.

McConnell ER, McClain MA, Ross J, LeFew WR, Shafer TJ. 2012. Evaluation of multi-well microelectrode arrays for neurotoxicity screening using a chemical training set. Neurotoxicology 33(5):1048-57.

McElvain J, Antoniadis H, Hueschen MR, Miller JN, Roitman DM, Sheats JR, Moon RL. 1996. Formation and growth of black spots in organic light- emitting diodes. J Appl Phys 80(10):6002-7.

McGlynn SP, Azumi T, Kasha M. 1964. External Heavy- Atom Spin—Orbital coupling effect. V. absorption studies of triplet states. Journal of Chemical Physics 40(2):507-15.

McQuarrie DA. 1997. Physical chemistry : A molecular approach. Sausalito, Calif.: University Science Books.

Meister M, Rachel OLW, Baylor DA, Shatz CJ. 1991. Synchronous bursts of action potentials in ganglion cells of the developing mammalian retina. Science 252(5008):939-43.

Moffitt JR, Lee JB, Cluzel P. 2012. The single-cell chemostat: An agarose-based, microfluidic device for high-throughput, single-cell studies of bacteria and bacterial communities. Lab Chip 12(8):1487-94.

Mohanty SK and Lakshminarayananan V. 2015. Optical techniques in optogenetics. Journal of Modern Optics 62(12):949-70.

Morefield SI, Keefer EW, Chapman KD, Gross GW. 2000. Drug evaluations using neuronal networks cultured on microelectrode arrays. Biosensors & Bioelectronics 15(7):383-96.

Naka S, Okada H, Onnagawa H, Yamaguchi Y, Tsutsui T. 2000. Carrier transport properties of organic materials for EL device operation. Synthetic Materials 111-112:331-3.

Nam Y and Wheeler BC. 2011. In vitro microelectrode array technology and neural recordings. Critical Reviews in Biomedical Engineering 39(1):45.

Nam Y, Musick K, Wheeler BC. 2006. Application of a PDMS microstencil as a replaceable insulator toward a single-use planar microelectrode array. Biomed Microdevices 8(4):375-81.

Navarrete EG, Liang P, Lan F, Sanchez-Freire V, Simmons C, Gong T, Sharma A, Burridge PW, Patlolla B, Lee AS, et al. 2013. Screening drug-induced arrhythmia using human induced pluripotent stem cell-derived cardiomyocytes and low-impedance microelectrode arrays. Circulation 128(11):S3.

Neher E and Sakmann B. 1992. The patch clamp technique. Sci Am 266(3):44-51.

Neher E, Sakmann B, Steinbach JH. 1978. The extracellular patch clamp: A method for resolving currents through individual open channels in biological membranes. Pflugers Archive 375(2):219-28.

Nomura K, Kamiya T, Hirano M, Hosono H. 2009. Origins of threshold voltage shifts in room-temperature deposited and annealed a-In–Ga–Zn–O thin-film transistors. Appl Phys Lett 95(1):013502.

Nomura K, Ohta H, Takagi A, Kamiya T, Hirano M, Hosono H. 2004. Room-temperature fabrication of transparent flexible thin-film transistors using amorphous oxide semiconductors. Nature 432(7016):488-92.

Normand V, Lootens DL, Amici E, A., Plucknett KP, Aymard P. 2000. New insight into agarose gel mechanical properties. Biomacromolecules 1(4):730.

Novak JL and Wheeler BC. 1986. Recording from the aplysia abdominal ganglion with a planar microelectrode array. IEEE Transactions on Biomedical Engineering BME-33(2):196-202.

Novellino A, Scelfo B, Palosaari T, Price A, Sobanski T, Shafer TJ, Johnstone AFM, Gross GW, Gramowski A, Schroeder O, et al. 2011. Development of micro-electrode array based tests for neurotoxicity: Assessment of interlaboratory reproducibility with neuroactive chemicals. Frontiers in Neuroengineering 4(4):4.

O'Brien DF, Baldo MA, Thompson ME, Forrest SR. 1999. Improved energy transfer in electrophosphorescent devices. Applied Physics Letters 74(3):442-4.

Oka H, Shimono K, Ogawa R, Sugihara H, Taketani M. 1999. A new planar multielectrode array for extracellular recording: Application to hippocampal acute slice. Journal of Neuroscience Methods 93(1):61-7.

Pancrazio JJ, Gray SA, Shubin YS, Kulagina N, Cuttino DS, Shaffer KM, Eisemann K, Curran A, Zim B, Gross GW, et al. 2003. A portable microelectrode array recording system incorporating cultured neuronal networks for neurotoxin detection. Biosensors and Bioelectronics 18(11):1339-47.

Pancrazio JJ, Whelan JP, Borkholder DA, Ma W, Stenger DA. 1999. Development and application of cell-based biosensors. Ann Biomed Eng 27(6):697-711.

Park JY, Yoo SJ, Lee EJ, Lee DH, Kim JY, Lee SH. 2010. Increased poly(dimethylsiloxane) stiffness improves viability and morphology of mouse fibroblast cells. BioChip Journal 4(3):230-6.

Perez MR, Mejia I, Salas-Villasenor AL, Stiegler H, Trachtenberg I, Gnade BE, Quevedo-Lopez MA. 2012. Hybrid CMOS thin-film devices based on solution-processed CdS n-TFTs and TIPS-pentacene p-TFTs. Organic Electronics 13(12):3045-9.

Perin R, Berger TK, Markram H. 2011. A synaptic organizing principle for cortical neuronal groups. Proc Natl Acad Sci U S A 108(13):5419-24.

Poli D, Pastore VP, Massobrio P. 2015. Functional connectivity in in vitro neuronal assemblies. Frontiers in Neural Circuits 9(57).

Pope M, Kallman HP, Magnante P. 1963. Electroluminescence in organic crystals J Chem Phys 38(8):2042-3.

Rawn JD. 2014. Organic chemistry. First edition.. ed. San Diego, CA: Elsevier.

Regehr KJ, Domenech M, Koepsel JT, Carver KC, Ellison-Zelski S, Murphy WL, Schuler LA, Alarid ET, Beebe DJ. 2009. Biological implications of polydimethylsiloxane-based microfluidic cell culture. Lab Chip 9(15):2132-9.

Rein ML and Deussing JM. 2012. The optogenetic (r)evolution. Molecular Genetics and Genomics 287(2):95-109.

Renault R, Sukenik N, Descroix S, Malaquin L, Viovy JL, Peyrin JM, Bottani S, Monceau P, Moses E, Vignes M. 2015. Combining microfluidics, optogenetics and calcium imaging to study neuronal communication in vitro. Plos One 10(4):e0120680.

Robinson DA. 1968. The electrical properties of metal microelectrodes. Proceedings of the IEEE 56(6):1065-71.

Sabitha KR, Sanjay D, Savita B, Raju TR, Laxmi TR. 2016. Electrophysiological characterization of nsc-34 cell line using microelectrode array. J Neurol Sci 370:134-9.

Saito T, Wu CC, Shiku H, Yasukawa T, Yokoo M, Ito-Sasaki T, Abe H, Hoshi H, Matsue T. 2006. Oxygen consumption of cell suspension in a poly(dimethylsiloxane) (PDMS) microchannel estimated by scanning electrochemical microscopy. Analyst 131(9):1006-11.

Sakar MS, Neal D, Boudou T, Borochin MA, Li Y, Weiss R, Kamm RD, Chen CS, Asada HH. 2012. Formation and optogenetic control of engineered 3D skeletal muscle bioactuators. Lab Chip 12(23):4976.

Sasaki H, et al. 2010. Parylene-coating in PDMS microfluidic channels prevents the absorption of fluorescent dyes. Sensors and Actuators B: Chemical 150(1):478-82.

Scarlatos A, Cadotte AJ, DeMarse TB, Welt BA. 2008. Cortical networks grown on microelectrode arrays as a biosensor for botulinum toxin. J Food Sci 73(3):E129-36.

Schmidt EM, Mcintosh JS, Bak MJ. 1988. Long-term implants of parylene-C coated microelectrodes. Medical & Biological Engineering & Computing 26(1):96-101.

Shafer TJ, Rijal SO, Gross GW. 2008. Complete inhibition of spontaneous activity in neuronal networks in vitro by deltamethrin and permethrin. Neurotoxicology 29(2):203-12.

Shepherd GMG, Pologruto TA, Svoboda K. 2003. Circuit analysis of experience-dependent plasticity in the developing rat barrel cortex. Neuron 38(2):277-89.

Shockley W and Pearson GL. 1948. Modulation of conductance of thin films of semi-conductors by surface charges. Phys Rev 74(2):232-3.

Skoog DA. 1998. Principles of instrumental analysis. Fifth Edition.. ed. Orlando, FL: Harcourt Brace College Publishers.

Smith JT, O'Brien B, Lee YK, Bawolek EJ, Christen JB. 2014. Application of flexible OLED display technology for electro-optical stimulation and/or silencing of neural activity. Journal of Display Technology 10(6):514-20.

Stett A, Egert U, Guenther E, Hofmann F, Meyer T, Nisch W, Haemmerle H. 2003. Biological application of microelectrode arrays in drug discovery and basic research. Anal Bioanal Chem 377(3):486-95.

Su X, Theberge AB, January CT, Beebe DJ. 2013. Effect of microculture on cell metabolism and biochemistry: Do cells get stressed in microchannels? Anal Chem 85(3):1562-70.

Suresh A, Wellenius P, Dhawan A, Muth J. 2007. Room temperature pulsed laser deposited indium gallium zinc oxide channel based transparent thin film transistors. Appl Phys Lett 90(12):123512.

Sze SM. 2007. Physics of semiconductor devices. 3rd ed.. ed. Hoboken, N.J.: Wiley-Interscience.

Takeuchi S, Ziegler D, Yoshida Y, Mabuchi K, Suzuki T. 2005. Parylene flexible neural probes integrated with microfluidic channels. Lab on a Chip 5(5):519.

Tang CW and VanSlyke SA. 1987. Organic electroluminescent diodes. Appl Phys Lett 51(12):913.

Tang CW and VanSlyke SA. 1989. Electroluminescence of doped organic thin films. J Appl Phys 65(9):3610-6.

Tang Y, Scheef EA, Gurel Z, Sorenson CM, Jefcoate CR, Sheibani N. 2010. CYP1B1 and endothelial nitric oxide synthase combine to sustain proangiogenic functions of endothelial cells under hyperoxic stress. American Journal of Physiology-Cell Physiology 298(3):C665-78.

Tateno T and Nishikawa J. 2014. A CMOS IC-based multisite measuring system for stimulation and recording in neural preparations in vitro. Frontiers in Neuroengineering 7(39).

Tetzlaff C, Okujeni S, Egert U, Wörgötter F, Butz M. 2010. Self-organized criticality in developing neuronal networks. PLOS Computational Biology 6(12):e1001013.

Thomas CA, Springer PA, Loeb GE, Berwald-Netter Y, Okun LM. 1972. A miniature microelectrode array to monitor the bioelectric activity of cultured cells. Exp Cell Res 74(1):61-6.

Toepke MW and Beebe DJ. 2006. PDMS absorption of small molecules and consequences in microfluidic applications. Lab Chip 6(12):1484-6.

Tokuda T., Nakajima S., Maezawa Y., Noda T., Sasagawa K., Ishikawa Y., Shiosaka S. and Ohta J. 2013. An in vitro demonstration of CMOS-based optoelectronic neural interface device for optogenetics. 2013 35th annual international conference of the IEEE engineering in medicine and biology society (EMBC); 2013; . 799 p.

Tønnesen J, Parish CL, Sørensen AT, Andersson A, Lundberg C, Deisseroth K, Arenas E, Lindvall O, Kokaia M. 2011. Functional integration of grafted neural stem cell-derived dopaminergic neurons monitored by optogenetics in an in vitro parkinson model. Plos One 6(3):e17560.

Tsao CW and DeVoe DL. 2009. Bonding of thermoplastic polymer microfluidics. Microfluidics and Nanofluidics 6(1):1-16.

Tung YC, Hsiao AY, Allen SG, Torisawa YS, Ho M, Takayama S. 2011. High-throughput 3D spheroid culture and drug testing using a 384 hanging drop array. The Analyst 136(3):473-8.

Udagawa K, Sasabe H, Igarashi F, Kido J. 2016. Simultaneous realization of high EQE of 30%, low drive voltage, and low efficiency roll-off at high brightness in blue phosphorescent OLEDs. Advanced Optical Materials 4(1):86-90.

Urabe T, Sasaoka T, Tatsuki K, Takaki J. 2007. 13.1: Invited paper: Technological evolution for large screen size active matrix OLED display. Society for Information Display 07 Digest 38(1):161-4.

Vanheusden K, Warren WL, Seager CH, Tallant DR, Voigt JA, Gnade BE. 1996. Mechanisms behind green photoluminescence in ZnO phosphor powders. J Appl Phys 79(10):7983-90.

Vincett PS, Barlow WA, Hann RA, Roberts GG. 1982. Electrical conduction and low voltage blue electroluminescence in vacuum-deposited organic films. Thin Solid Films 94(2):171-83.

Wagenaar DA, Madhavan R, Pine J, Potter SM. 2005. Controlling bursting in cortical cultures with closed-loop multi-electrode stimulation. The Journal of Neuroscience 25(3):680-8.

Wang L, Yoon MH, Facchetti A, Marks T . 2007. Flexible inorganic/organic hybrid thin-film transistors using all-transparent component materials. Adv Mater 19(20):3252-6.

Wang Z, Volinsky AA, Gallant ND. 2014. Crosslinking effect on polydimethylsiloxane elastic modulus measured by custom-built compression instrument. Journal of Applied Polymer Science 131(22).

Welkenhuysen M, Hoffman L, Luo Z, De Proft A, Van den Haute C, Baekelandt V, Debyser Z, Gielen G, Puers R, Braeken D. 2016. An integrated multi-electrode-optrode array for in vitro optogenetics. Scientific Reports 6:20353.

Wypych G. 2012. PS polystyrene. In: Handbook of polymers. Wypych G, editor. Oxford: Elsevier. 541 p.

Xiang G, et al. 2007. Microelectrode array-based system for neuropharmacological applications with cortical neurons cultured in vitro. Biosensors and Bioelectronics 22(11):2478-84.

Yao J, Xu N, Deng S, Chen S, She J, Shieh HPD, Liu PT, Huang YP. 2011. Electrical and photosensitive characteristics of a-IGZO TFTs related to oxygen vacancy. IEEE Transactions on Electron Devices 58(4):1121-6.

Young EWK, Berthier E, Guckenberger DJ, Sackmann E, Lamers C, Meyvantsson I, Huttenlocher A, Beebe DJ. 2011. Rapid prototyping of arrayed microfluidic systems in polystyrene for cell-based assays. Anal Chem 83(4):1408-17.

Young SS, Keunchang C, Sun HL, Seok C, Park SJ, Chung C, Dong-Chul H, Jun KC. 2003. PDMS-based micro PCR chip with parylene coating. J Micromech Microengineering 13(5):768.

Zhang Y., Zhang X., Fang J., Jiang S., Zhang Y., Gu D., Nelson R. D. and LaRue J. C. 30 September 2010. Application of SU-8 as the insulator toward a novel planar microelectrode array for extracellular neural recording. Proceedings of the 2010 5th IEEE international conference on nano/micro engineered and molecular systems; 20-23 January 2010; . 395 p.

BIOGRAPHICAL SKETCH

Audrey Sue Hammack was born in Tyler, Texas, in 1986 to Charles and Susanne Hammack. After growing up in Tyler, and graduating as the salutatorian of the class of 2005 of John Tyler High School, she attended The University of Texas at Tyler. In the summer of 2010, she completed a National Science Foundation Research Experience for Undergraduates internship at the University of California, Santa Barbara, in the lab of Song-I Han. She graduated with a Bachelor of Science in Chemistry in 2011. She moved to Richardson, Texas, later that year in order to attend graduate school at The University of Texas at Dallas. She joined the research group of Dr. Bruce Gnade in January of 2012 and began work on the projects that became the subject of this dissertation. In May of 2016, she took a six-month internship at Qorvo, Inc., in Richardson, Texas, where she was a process engineering intern supporting work in the thin films deposition group.

CURRICULUM VITAE

Audrey Hammack

Address: 800 W. Campbell Rd. RL 10, Richardson, Texas, 75080

Email: ash107020@utdallas.edu

EDUCATION

PhD in Chemistry **May 2018**
University of Texas at Dallas, Richardson, TX
Bachelor of Science in Chemistry **May 2011**
University of Texas at Tyler, Tyler, TX

PROFESSIONAL EXPERIENCE

Process Engineering Intern **May 2016-November2016**
Thin Films Group, Qorvo Inc., Richardson, Texas

TEACHING/RESEARCH ASSISTANT EXPERIENCE

Graduate Teaching Assistant **August 2011-May 2013, August 2017-December 2017**
Lab courses taught: Organic chemistry I and II, Instrumental Analysis
Graduate Research Assistant **January 2012-December 2017**
Performed research for dissertation
Graduate Assistant **January 2018-May 2018**
Supported UTD cleanroom staff as a graduate assistant in the office of research. Assisted in maintenance of atomic force microscope, training on ball bonder system, and general daily operations

RESEARCH INTERESTS

Semiconductor processing technology, *in vitro* neural interfaces

PUBLICATIONS

Hammack A, Chen YL, Pearce JK. 2011. Role of dissolved salts in thermophoresis of DNA: lattice-Boltzmann-based simulations. Phys. Rev. E. Stat Nonlin Soft Matter Phys., **83** (3).

Young CA, Saosupa S, **Hammack A,** Tangonan AA, Anuragodom P, Jia H, Jamison AC, Panichphant S, Gnade BE, Lee TR. 2014. Synthesis and characterization of poly(2,5-didecyl-1,4-

phenylene vinylene),(2,5-didecyloxy-1,4-phenylene vinylene), and their alternating copolymer Applied Polymer Science, **131** (23).

Charkhkar H, Arreaga-Salas DE, Tran T, **Hammack A,** Voit WE, Pancrazio JJ, Gnade BE. 2016. Novel disposable microelectrode array for cultured neuronal network recording exhibiting equivalent performance to commercially available arrays. Sensors and Actuators B: Chemical, **226**.

Hammack A, Rihani RT, Black BJ, Gnade BE, Pancrazio JJ. Submitted March 2018. A patterned polystyrene-based microelectrode array for in vitro neuronal recordings. Biomedical Microdevices.

CONFERENCE PRESENTATIONS

Hammack, A., Avendaño-Bolivar, A., Jia, H., Gnade, B.E., "A Novel Substrate for In Vitro Optogenetic Experiments." Poster presentation. 2014 Neural Interfaces Conference, Dallas, Texas, June 2014.

Hammack, A., Avendaño-Bolivar, A., Jia, H., Gnade, B.E., "A Novel Substrate for In Vitro Optogenetic Experiments." Poster presentation. 2014 Annual Meeting of the Biomedical Engineering Society, San Antonio, Texas, October 2014.

TECHNICAL SKILLS

Cleanroom experience: Photolithography, plasma-enhanced chemical vapor deposition, thermal deposition, RF magnetron sputtering, e-beam metallization, reactive ion etch

Film characterization: optical microscopy, FT-IR spectroscopy, ellipsometry, stylus profilometry, beam profile reflectrometry

Electrical characterization: Electrical impedance measurements, electroluminescence spectrometry, capacitance-voltage and current-voltage measurements

Programs: MATLAB, AutoCAD, MS Office, Spotfire

Relevant coursework: Photolithography and nanofabrication, semiconductor physics, and Very Large Scale Integration (VLSI) technology

LANGUAGES

English (fluent), Spanish (conversational)